Integrated petrogenesis of podiform chromitites

博　士　論　文

Integrated petrogenesis of podiform chromitites

(ポディフォーム・クロミタイトの統合的成因論)

金沢大学大学院 自然科学研究科

環境科学専攻 自然計測講座

学籍番号：1223142011

氏名：三浦　真

主任指導教員名：海野　進

提出年月日：2015 年 4 月２２日

Contents

Chapter 1: Introduction

Podiform chromitite has been well known as a resource of chromium. They sometimes occur in the Moho transition zone to uppermost mantle section of ophiolites (e.g., Nicolas 1989) (Fig. 2-1, 2). Chromitite has been interpreted as a magmatic product of melt/peridotite reaction and subsequent melt mixing at low pressure condition such as Moho transition zone to uppermost mantle (e.g., Arai and Yurimoto 1994; Zhou et al., 1994) regarding the existence of its dunite envelope. The presence of Na amphibole, such as pargasite, inclusions in chromian spinel of chromitite is possibly one of indicators for low pressure origin of chromitites (e.g., Arai and Matsukage 1998; Niida and Green 1999; Borisova et al., 2012).

Recently, however, some ultrahigh-pressure (=UHP) minerals, such as diamond and moissanite, have been found from mantle chromitites and its host peridotites in the Luobusa ophiolite, Tibet, and the Ray-Iz ophiolite, Polar Urals (e.g., Robinson et al., 2004; Yang et al., 2014). Coesite lamellae in spinels from some UHP chromitites from the Luobusa ophiolite strongly indicate their ultrahigh-pressure origin (Yamamoto et al. 2009). These findings seriously require us to reconsider the framework for the origin of podiform chromitites and relationship between chromitite formation and mantle dynamics (Arai 2010, 2013). Despite the necessity of detailed petrologic studies of UHP chromitites and surrounding peridotites (harzburgite and dunite), such studies have been very limited until now. In this study, I would like to re-examine and compare some chromitite pods from the Oman, Tibet and Polar Urals ophiolites with chromitite xenoliths from the Takashima alkali basalt (Arai and Abe 1994) in terms of petrographical characteristics such as inclusions in spinel, to reconstruct the framework of the genesis of podiform chromitite.

This thesis is composed of five chapters. In Chapter 2, some chromitite pods from the northern Oman ophiolite are compared to summarize characteristics of the low-pressure chromitite as a background. Chapter 3 highlights the similarities between discordant chromitite in the northern Oman ophiolite and sub-arc chromitite xenoliths from the Takashima alkali basalt, southwest Japan, in its textural variation, mineral chemistry and PGE chemistry, to constrain the origin of discordant chromitites in

ophiolites. Petrographycal characteristics of some UHP chromitites and their host peridotites from the Luobusa and the Ray-Iz ophiolites are examined and summarized in Chapter 4.

Chapter 2: Genesis of podiform chromitites in the northern Oman ophiolite

2.1: Abstract

Some chromitite pods in the mantle section of Salahi and Fizh blocks of northern Oman ophiolite along Wadi Hilti, Rajmi and Fizh, were examined to constrain the genesis of ophiolitic chromitite and host peridotite. They were classified into two types, discordant and concordant, in terms of structural relationship with the foliation of surrounding harzburgite, mineral chemistry and characteristics of micro-inclusions in spinel. Discordant chromitite pods in the mantle section along Wadi Hilti, Rajmi and Fizh, have an arc-related affinity in spinel chemistry and trace element characteristics of clinopyroxenes. Chromian spinels from Oman discordant pods show high Cr#s (=Cr/(Cr+Al) atomic ratio), around 0.65 to 0.78, and low-Ti contents (< 0.2 wt%), indicating an arc-related feature. Harzburgites adjacent to discordant dunites and chromitites also show a high-depleted feature, e.g., high Cr# (0.65 to 0.75) of spinels and low HREE content in clinopyroxenes. This highly depleted harzburgite surrounding discordant dunite and chromitite shows transitional changes in spinel and REE chemistry toward the surrounding oceanic harzburgites. Calculated compositions of the melt in equilibrium with clinopyroxene in dunite enveloping discordant chromitite along Wadi Hilti and Fizh suggest that the discordant chromitite and surrounding peridotite were derived from high-Mg andesite, such as boninite. Spinel grains in discordant chromitites are full of primary hydrous mineral, e.g., pargasite and Na phlogopite, inclusions. On the other hand, concordant pods along Wadi Hilti and Rajmi show contrasted characteristics in mineral chemistry and in micro-inclusions in spinel. In contrast, spinels from concordant pods and surrounding associated peridotites show lower Cr#s, around 0.5 to 0.65, possibly showing a sub-oceanic character. Thin pyroxene lamellae in spinels, similar to those in ultrahigh-pressure chromitites from Tibet and Polar Urals, are typically available only from concordant chromitites. Spinels in concordant pods also contain primary hydrous mineral inclusions as in discordant pods, although they are far less abundant and smaller in size than in discordant pods. Olivines in the dunite enveloping a concordant chromitite along Wadi Hilti, are extraordinarily high in NiO (up to > 0.5 wt %), suggesting

subsolidus Ni diffusion from the chromitite.

The involved melt was clearly different between the two types of chromitite, discordant and concordant. Concordant chromitites have probably experienced a longer duration of cooling. Exsolution of silicate lamellae in spinel and subsolidus Ni diffusion in olivine from dunite envelope were caused by cooling during emplacement as a concordant pod by horizontal mantle flow. Discordant chromitites, dunites and surrounding highly-depleted harzburgites are probably formed at the supra-subduction zone environment just before ophiolite obduction. The involved sub-arc magma was probably generated by the flux melting of depleted mantle harzburgite on the subducted slab, judged from incompatible element enrichment in clinopyroxene from dunite and harzburgite. Coexistence of the two types of chromitites and surrounding harzburgites reflects switch of tectonic setting to sub-arc mantle from oceanic mantle.

2.2: Introduction

Ophiolites provides us with excellent opportunities for observing and understanding various processes occurring throughout upper crust to uppermost mantle section of the lithosphere. However, their origin has been controversial because some complicate questions in ophiolites still remain. Coexistence of two contrasting types of magmatism, oceanic and arc-like, recorded in the constitutuent rocks of ophiolite (e.g., Ishikawa et al., 2002; Python and Ceuleneer 2003; Arai et al., 2006) is one of problems for our understanding of the origin of ophiolite (e.g., Nicolas 1989). Such polygenetic characteristics of the constituent rocks of ophiolite complexes have been discussed for the Oman ophiolite (e.g., Ishikawa et al., 2002; Python and Ceuleneer 2003; Arai et al., 2006) (Fig. 2-1). Recently, spatial distribution of highly depleted harzburgites, possible residues after arc-related magma extraction, was reported from the mantle section of Fizh block (Kanke and Takazawa 2014). The sub-arc characteristics have been interpreted to be caused by the secondary modification of pre-existing oceanic lithosphere due to a switch of tectonic setting from a spreading ridge to an island arc (e.g., Arai et al., 2006).

The chromitite is one of key rocks in the ophiolite, although its abundance is very low, to interpret the origin of ophiolite. Ophiolitic chromitites have been frequently

interpreted as a product of melt/harzburgite reaction within uppermost mantle (e.g., Arai and Yurimoto 1994; Zhou et al., 1994). They are divided into two types, discordant and concordant, in terms of their structural relationship with the foliation of surrounding harburgite (Cassard et al., 1981) (Fig. 2-2). Concordant pods are interpreted to have been intensely deformed by plastic flow and tectonically rotated to become parallel to the surrounding peridotite foliation. Discordant pods and their dunite envelopes are of younger origin than concordant pods regarding the structural attitude. The generation of two types of ophiolitic chromitite is possibly related to the polygenetic nature of ophiolites, which recorded: the early stage of a spreading ridge such as a mid-ocean ridge and the later stage of an arc-like setting just before ophiolite obduction. This is shown by differences in spinel chemistry and platinum group element (PGE) mineralogy/chemistry (Ahmed and Arai 2002; Miura et al., 2012). Some studies of ophiolites suggest that the discordant chromitite was probably generated by arc-related magmatism, such as boninitic one (e.g., Ahmed and Arai 2002; Uysal et al., 2005), at low-pressure mantle condition. Miura et al. (2012) made a comparison between the two structural types of chromitite, discordant and concordant, along Wadi Hilti, northern Oman ophiolite. They show the contrasted characteristics in mineral chemistry and micro inclusions in spinel. In this chapter, I conducted detailed analyses of the concordant and discordant chromitites in the northern Oman ophiolite.

2.3: Geological background

The Oman ophiolite has been well known as a complete ophiolite complex throughout the upper crustal to uppermost mantle rocks of a kind of ocean-floor origin (cf. Nicolas 1989) (Fig. 2-1). Structural and petrological characteristics of many chromitite pods in the mantle section to the Moho transition zone (=MTZ) have been determined (e.g., Auge 1987; Nicolas 1989) (Fig. 2-2). As an exceptional case of podiform chromitite occurrence, an upper crustal chromitite was found from a late-intrusive dunite body in the transition zone between sheeted dyke and upper gabbro along Wadi Hilti (Arai et al., 2004). Although various chromitite pods exist in the Oman ophiolite, the lack of good exposures because of mining and exploiting is one

of serious problems for systematic observations and sampling of chromitite and surrounding peridotites. Some localities from the northern Oman ophiolite will solve this problem; especially the two chromitite pods in the deeper mantle section of the Salahi block, at about 5 km below the Moho transition zone along Wadi Hilti, were described by Ahmed and Arai (2002) and Miura et al. (2012) (Figs. 2-3, 4). They are quite intact from exploiting and mining, and suitable for detailed petrological observation and analysis with surrounding peridotites. In addition to them, discordant pods in deeper mantle section along Wadi Rajmi and Wadi Fizh have also good exposures (Figs. 2-3, 5, 6). I selected three discordant pods along Wadi Hilti, Rajmi and Fizh, two concordant pods along Wadi Hilti and Rajmi, and one MTZ chromitite pod from Wadi Rajmi (Fig. 2-1) for this study.

2.4: Geologic and petrographic descriptions of chromitites and surrounding peridotites

Wadi Hilti area

Wadi Hilti area is located in the Salahi block of the northern Oman ophiolite (Fig. 2-1). Two structural types of chromitite, concordant and discordant, are exposed on the same cliff in the deeper part of mantle section (Ahmed and Arai 2002; Miura et al., 2012) (Figs. 2-3, 4). The pods are about 100 m apart from each other in plan (Figs. 2-3a, 4a). The concordant chromitites is almost lenticular in shape and mostly subconcordant to concordant to the foliation of the surrounding harzburgite (Fig. 2-7a). The discordant one is highly irregular in shape and completely discordant to the harzburgite (Fig. 2-7b). The envelope is thicker around the discordant pods than around the concordant pods (Fig. 2-7a, b). Chromitites from both pods show dense massive to disseminated textures, but the concordant chromitite shows a homogeneous appearance. Discordant chromitites are highly heterogeneous in olivine/spinel ratio. The boundary between the chromitite and the dunite envelope is different in appearance between the two types of chromitites. Olivine-rich disseminated marginal part of the concordant chromitite is sometimes in a sharp contact with dunite, but sometimes form a transition zone, around several tens of centimeters wide. On the other hand, the olivine-rich part, sometimes with anti-nodular textures, always grades

to dunite via a transition zone around 50 centimeters wide around the discordant pod. The dunite envelope quickly grades outward (with a transition zone of several tens of centimeters) to surrounding harzburgite around the two chromitite pods.

The chromitites comprise subhedral to anhedral chromian spinel, olivine and minor orthopyroxene which is moderately to strongly serpentinized. Chromian spinels are reddish brown in thin section, indicating their moderately Cr-rich character (Fig. 2-8). Spinels from the discordant chromitite are full of orbicular inclusions, up to several tens of microns across, of hydrous minerals and pyroxenes. They usually show a concentric distribution indicating a primary origin (Fig. 2-8a). The orbicular inclusions are composed of pargasite, Na phlogopite and pyroxenes (Ahmed and Arai 2002; Miura et al., 2012). In contrast, the orbicular inclusions such as in the discordant chromitite are apparently absent in spinel grains from the concordant chromitite (Fig. 2-8j). Some spinels contain, however, similar orbicular inclusions, although very sparse and minute (several microns across), composed of pargasite, Na phlogopite and pyroxenes as in the discordant chromitite (Fig. 2-9). Spinel grains from the concordant chromitite additionally contain numerous needle-like exsolution lamellae (Fig. 2-9). Such exsolution lamellae are not included in spinels from the discordant chromitite. They are very thin but up to 100 microns long, and identified as pyroxenes by Raman spectroscopy as described below.

Dunites forming the envelope are coarse-grained and weakly serpentinized, but clearly different in texture between the two types of chromitite pod. Spinels are euhedral to subhedral in both dunites (Figs. 2-8b and k). The dunite enveloping the concordant pod shows a prominent porphyroclastic texture, with coarse and strongly kinked porphyroclasts (Fig. 2-8k). In contrast, the dunite around the discordant pod shows almost an equigranular texture, composed of coarse non-strained olivine grains with curvilinear boundaries. Some olivines from dunite around the concordant chromitite sometimes contain lamellae of chromian spinel and magnetite.

The surrounding harzburgites, weakly to moderately serpentinized, show weakly porphyroclastic to protogranular textures for the both chromitite pods. Some olivines from them are kinked, suggesting deformation. The harzburgite around the concordant pod contains a small amount of clinopyroxene, which is closely associated with

orthopyroxene. In contrast, clinopyroxene is very rarely present in harzburgite around the discordant pod, and its amount increases with increasing distance from the dunite envelope (Fig. 2-12). The orthopyroxene content is 10 to 18 vol %, but is apparently high (up to 18 vol %) around the boundary with dunite (Fig. 2-12). I systematically took samples of harzburgite at intervals of 2 m, if permitted by exposure condition, along a transet, A-A', from the contact with dunite enveloping the discordant chromitite outward (Fig. 2-12).

Wadi Rajmi area

Wadi Rajmi area is well known as abundance of various chromitite pods in the mantle section including a Moho transition zone (=MTZ) (e.g., Auge 1987; Nicolas 1989; Rollinson 2008) (Fig. 2-3). MTZ-type chromitite pods exist in a thick MTZ dunite body several hundred meters below the contact between peridotites and layered gabbro. The MTZ chromitite pod is irregular in shape, and the rock is heterogeneous in texture showing massive to disseminated textures. MTZ chromitites are sometimes cut by gabbroic veins. A concordant chromitite pod was found about 2 km stratigraphically below the Moho transition zone (Figs. 2-1, 3). Although we cannot observe its occurrence because of active mining at present, Abbou-Kebir et al. (2011) described that this pod is subconcordant to concordant to the enclosing harzburgite foliation. This concordant chromitite shows massive to disseminated texture. Discordant chromitite pods were found in a thick discordant dunite body near the abandoned chromitite mine in the deeper mantle section around 5 km below the MTZ (Fig. 2-3). The Rajmi discordant chromitite pods show a thin (< 1 m in thickness) almost dike-like form, being highly heterogeneous in texture (Fig. 2-5). Chromitites from the pods show massive to disseminated or anti-nodular textures, and seem to be gradational to the dunite envelope. A nodular textured chromitite pod occurs in a spinel-rich dunite near these discordant pods.

The MTZ chromitites comprise subhedral to anhedral chromian spinel, feldspar, amphibole and olivine. Chromian spinels from the MTZ chromitite are reddish brown in thin section, indicating their moderately Cr-rich character. Spinel grains in the MTZ chromitite typically contain numerous rod- and needle-like rutile and clinopyroxene

exsolution lamellae, and the primary hydrous mineral inclusions. The MTZ chromitite shows dense massive to disseminated textures. Gabbroic veins sometimes cut the texture of chromitite. The mantle concordant chromitite is composed of subhedral to anhedral spinel and olivine, which is moderately to strongly serpentinized. Chromian spinels in the concordant chromitite contain numerous exsolution lamellae of pyroxenes similar to those in the Hilti concordant chromitite, and orbicular inclusions of hydrous minerals and pyroxenes. Olivine grains in the mantle concordant pod are sometimes kinked, suggesting deformation. The mantle discordant chromitites are composed of subhedral to anhedral spinel and olivine. Their spinels, from the various textural types, are dark to reddish brown in thin section, indicating their Cr-rich character. Olivines composing the olivine nodules in anti-nodular chromitite are coarser in size than those in surrounding spinel-rich dunites. Some spinels contain the primary orbicular inclusions composed of hydrous minerals and pyroxenes.

In-situ dunite sample could not be taken as samples because of mining for the concordant pod. Dunite enveloping the discordant pods shows almost an equigranular texture, composed of coarse non-strained olivine grains and euhedral to subhedral spinel grains. The surrounding harzburgite, weakly to moderately serpentinized, shows weakly porphyroclastic to protogranular textures for both the concordant and discordant chromitites. Their olivines and orthopyroxens are sometimes kinked.

Wadi Fizh area

Wadi Fizh area is also well known as producing various pods from the mantle section to the Moho trantision zone. A discordant chromitite pod exists in discordant dunite within the mantle harzburgite around 4 km below the Moho transition zone (Fig. 2-3c). The Fizh discordant chromitite pod is highly irregular in shape. Chromitites from the pod show heterogeneous and various textures, such as massive, disseminated, nodular and anti-nodular textures (Fig. 2-4). Disseminated textures sometimes gradually change to nodular textures within the pod (Fig. 2-6). Dike and network-like dunite veins crosscut the texture of chromitite (Fig. 2-6). The contact between the dunite envelope and enclosing harzburgite is almost sharp.

The Fizh discordant chromitites comprise subhedral to anhedral chromian spinel

and olivine, and show dense massive to disseminated textures. Chromian spinels are reddish brown in thin section, indicating their moderately Cr-rich character. They contain the primary orbicular inclusions of hydrous minerals and pyroxenes.

The dunite enveloping the Fizh discordant chromitite is coarse-grained and weakly serpentinized, and show an equigranular texture, composed of non-kinked olivine grains. The dunite around the discordant pod contains a small amount of clinopyroxene, which is closely associated with spinel grains (Fig. 2-8g). Olivines in dunite sometimes contain lamellae composed of spinel and magnetite. The surrounding harzburgite shows weakly porphyroclastic to protogranular textures. Their olivines from them are sometimes kinked.

2.5: Analytical methods

Mineral chemistry

Minerals were analyzed by a JEOL wave-length dispersive electron microprobe (JXA8800R) at Kanazawa University. Analytical conditions were 20 kV accelerating voltage, 20 nA probe current, and 3 or 0 μm probe diameter. Natural and synthetic minerals were used as standards, and the ZAF matrix correction algorithm was used during data reduction. Ferrous and ferric iron contents of chromian spinel were calculated assuming spinel stoichiometry, while all iron was assumed to be Fe^{2+} in silicates. Mg# is $Mg/(Mg + Fe^{2+})$ atomic ratio, and Cr# is Cr/(Cr + Al) atomic ratio.

The trace-element (Ti, Sr, Y, Zr, Nb, and PGEs = rare earth elements) compositions of clinopyroxene were determined with a laser ablation (193 nm ArF excimer; Micro Las GeoLas Q-Plus), inductively coupled plasma mass spectrometer (Agilent 7500S; LA-ICP-MS) at Kanazawa University (Morishita et al., 2005). I used a laser energy density of 8 J/cm^2 operating at a frequency of 6 Hz, and 30, 40, and 50-μm laser spot sizes. The NIST 612 standard glass was used for calibration with Si as an internal standard.

Raman spectroscopy

Raman spectra of microinclusions in minerals were determined with a micro-Raman system (HORIBA Jobin Yvon, LabRAM HR800) equipped with a 532 nm

Nd:YAG laser (Showa Optronics Co., Ltd, J100GS-16), 514 nm Ar^+ laser (Melles Griot, 43 Series Ion Laser, 543-GS-A02) and an optical microscope (Olympus, BX41). The Nd:YAG laser has an irradiation power at 1.6 mW with a spectral resolution of about ± 2.5 to ± 3.5 cm^{-1}, the Ar^+ has an irradiation power at 70μW with a spectral resolution of about ± 1.6cm^{-1}. For tiny inclusions and exsolutions in host minerals, the gained Raman spectra were processed to remove the signal of host spinel using LabSpec software (ver. 5) as shown in Fig. 2-10.

2.6: Mineral chemistry

2.6.1: *Major-element chemistry*

Chromian spinels show systematic chemical variations between two types of chromitite pods and enclosing peridotites from Wadi Hilti, Rajmi and Fizh (Fig. 2-11). Spinels in discordant pods are slightly higher in Cr# than those in concordant pods, although those from the Fizh discordant chromitite show a relatively low Cr# (around 0.6) (Fig. 2-11). The Cr# of spinel in chromitite is 0.6-0.7 for the Hilti and Rajmi concordant pods, but is higher than 0.7 for the Hilti and Rajmi discordant pods. Spinels in the dunite envelope are almost similar in Cr# and Ti content to those in chromitites for both types of chromitites (Arai 1997). The Fe^{3+}/ (Cr+Al+Fe^{3+}) atomic ratio of spinel in the envelope dunite is slightly higher than in the chromitite (Fig. 2-11a). Chromian spinels in the surrounding harzburgite show chemical differences between the two types of chromitite. The Cr# of spinel is 0.5-0.6 in harzburgites around the concordant pod, and is 0.6-0.7 in those enclosing discordant pods (Figs. 2-11a and d). The Cr# of spinel in the surrounding harzburgites of the Hilti discordant pod gradually decreases with distance from the contact with dunite, from 0.65 to 0.45 along the transect A-A' (Figs. 2-11 and 12). This tendency shows a negative correlation between the Na_2O content of clinopyroxene and modal % of pyroxenes (Fig. 2-12).

Olivines are high in forsterite (Fo) and NiO contents in chromitites, Fo_{96} and 0.7-0.8 wt% in the Hilti concordant chromitites, and Fo_{95} and 0.6-0.7 wt% in the discordant ones (Fig. 2-11g). Olivine in contact with spinel in the concordant pod especially shows a high Fo (around 96.5) and NiO content (0.8 wt%) (Fig. 2-13a). Olivines from surrounding harzburgites are Fo_{91-92} and contain 0.3-0.4 wt% NiO around the both

types of chromitite. Olivines in the dunite envelope are mostly similar in Fo content (91-91) to the surrounding harzburgites. However, the NiO content of olivine is noticeably higher in the dunite enveloping the concordant pod, especially in the dunite in contact with chromitite, up to around 0.5 wt%. The NiO content gradually decreases with increasing distance from the contact with chromitite (Fig. 2-13). This is in contrast to the dunite enveloping discordant pod, where olivine is not so high in NiO, around 0.4 wt% (Fig. 2-13c).

2.6.2: *Trace-element chemistry*

Chondrite-normalized trace element patterns of clinopyroxene from harzburgites enclosing the Hilti discordant pod were characterized by the depletion of light REE (LREE) (Fig. 2-14). Some trace element patterns show positive Sr and Ti anomalies (Fig. 2-14a). Clinopyroxene is more enriched in LREE, e.g., La and Ce, in the harzburgite adjacent to the dunite than in distal ones. In contrast, concentrations of heavy REE (HREE), e.g., Yb, in clinopyroxene are lower in proximal harzburgites than in distal ones. The surrounding harzburgites are characterized by the low Y in clinopyroxene and high Cr# of spinel, plotted around the depleted end of the abyssal peridotite range (Fig. 2-11h). The trace-element pattern of clinopyroxene in the dunite envelope shows a simple decline from HREE to LREE, and shows overall higher levels of REE than that from harzburgites (Fig. 2-14a). Clinopyroxene inclusions in spinel from the Hilti discordant chromitite are more enriched in LREE and Sr than in discrete clinopyroxne from the dunite and harzburgites. Trace element patterns for clinopyroxene inclusion in spinel of chromitite show negative Zr and Ti anomalies (Fig. 2-14a). Clinopyroxenes in harzburgites enclosing the Hilti concordant and the Fizh discordant chromitites show negative Sr and Zr anomaries, and are within the range for abyssal peridotites (Tamura and Arai 2008) (Fig. 2-14c).

2.7: Raman spectroscopy of minute inclusion in spinel of chromitite

Minute exsolution lamellae and orbicular inclusions in chromian spinel from the Hilti and Rajmi concordant chromitites and Rajmi MTZ chromitite were examined by Raman spectroscopy. Raman spectroscopy revealed that the exsolution lamellae in

spinels from the Hilti and Rajmi concordant chromitites mainly consist of clinopyroxene (>90%) with subordinate orthopyroxene (<10%) (Fig. 2-10). Preliminary FE- (Field-emission type) microprobe analysis indicates that lamellar clinopyroxene and orthopyroxene in spinel identified by Raman spectroscopy are diopside and enstatite (Miura et al., 2012). The lamellar enstatite is not clinoenstatite but orthoenstatite, based on Raman spectroscopic characteristics (Huang et al., 2000; Ulmer and Stalder 2001). The minute orbicular inclusions in spinels from the Hilti and Rajmi concordant pods are composed of pargasite, Na phlogopite and pyroxenes, similar to those in the discordant pods from Wadi Hilti, Rajmi and Fizh (Fig. 2-10). Numerous exsolution lamellae in spinel of the Rajmi MTZ chromitite consist of rutile and clinopyroxene.

2.8: Discussion

2.8.1: *Differences between the two types of chromitites*

The involved magmas were quite different between the two types of chromitite pods in the northern Oman ophiolite in chemical characteristics (Figs. 2-8, 9, 11). Spinel chemistry and trace-element characteristics of chromitites and surrounding peridotites suggest that the concordant pods were formed through reaction of MORB-like melt with wall harzburgite beneath a spreading ridge, whereas the discordant pods were precipitated through reaction between some arc-related magma and harzburgite at a later setting (Ahmed and Arai 2002; Miura et al., 2012). Spinels in the concordant chromitite and associated peridotites are plotted within the compositional field for spinels from MORB-related plutonic rocks (Figs. 2-11 d-f). In contrast, the spinel compositions for the discordant chromitite and surrounding peridotites are off the compositional range for MORB-related spinels, and well within range of spinels from arc-related plutonic rocks (Arai et al., 2011; Miura et al., 2012) (Figs. 2-11 a-c).

Numerous silicate lamellae in chromian spinel from the concordant pods indicate the precursor spinel before exsolution of silicates had relatively Si- and Ca- rich characters (Fig. 2-9). Yamamoto et al. (2009) suggested that the precursor phase of spinel from UHP chromitites in Tibet most likely had a Ca-ferrite or Ca-titanite structure (Chen et al., 2003) for the origin of coesite and diopside lamellae. However,

the Oman concordant pods are clearly of low-P origin, because of the existence of the primary pargasite inclusion in spinel (e.g., Niida and Green 1999; Frost 2006) (Figs. 2-9f, i and 10). Brey et al. (1999) and Aranovich and Kawasaki (2007) indicated that SiO_2 content in spinel slightly increases with increasing temperature and pressure. Although there is no experimental data for Ca content in spinel, the dissolution of pyroxene component into spinel structure under high-T condition is expected. Existence of pyroxene and rutile lamellae in chromian spinel from the Rajmi MTZ chromitite, being of clearly low-P origin, also indicates that the previous spinel had a relatively Si- and Ti- rich character (Figs. 2-9 j-l). In contrast, spinels in the discordant pods have no silicate lamellae. The common occurrence of silicate lamellae in chromian spinel only from the concordant and the MTZ pods indicates their longer duration of subsolidus cooling than the discordant pods. This is consistent with the younger origin for the latter in terms of structural attitude with surrounding peridotite (Cassard et al., 1981). In addition, olivines in the dunite in just contact with the Hilti concordant pod are remarkably high in NiO (up to 0.5 wt%) and Fo (around 92 mol%) contents (Figs. 2-11g and 13). Olivines in the dunite adjacent to the discordant pod do not show such high contents of NiO and Fo (Fig. 2-13c). The Ni content in olivine is initially controlled by the partitioning between olivine and magma on partial melting/magma extraction processes (Sato 1977; Ishimaru and Arai 2008; Negishi et al., 2013). The initial crystallization of Ni-rich olivine from Ni-rich magma is a simple way to form high-Ni olivine. The only way to form high-Ni olivine in the dunite around chromitite, the Ni redistribution to olivine from the chromitite as in the manner in Ni enrichment in matrix olivines within chromitites (e.g., Arai 1980; Ozawa 1984) (Fig. 2-13a). The width of the Ni-rich olivine zone (diffusion length) in dunite means a long annealing time for the concordant chromitite, if we consider Ni diffusion coefficient (D_{Ni}) in olivine (Ito et al., 1999; Petry et al., 2004). Although D_{Ni} strongly depends on the composition of olivine (Petry et al., 2004), I estimated the annealing time for the concordant pod assuming the annealing temperature of 1100°C and the diffusion length of 10 cm in olivines. The D_{Ni} ($3.15\times10^{-17}m^2s^{-1}$ and $4.7\times10^{-17}m^2s^{-1}$) provided by Ito et al. (1999) and Petry et al. (2004) indicates the diffusion length of 10cm can be attained in around 20-30 My even at 1100°C. However, this time is too long for the

interval of several My between MORB- and arc-related magmatism (V1 and V2 volcanisms) of the Oman ophiolite (e.g., Kusano et al., 2014). The high-Ni olivine zone in profiles is mostly longer than 10cm (Fig. 2-13), and sometimes shows complicated distributions (Fig. 2-13d). This problem possibly resulted from incomplete sampling due to incomplete distributions of dunite and chromitite on outcrops.

The differences of cooling duration between the two types of pod are clear, and resulted from the difference of time of formation of chromitite. This is consistent with the geological context and mineral chemical characteristics of chromitite (Fig. 2-11).

2.8.2: *Formation of discordant chromitite at the initiation of sub-arc mantle processes*

The discordant chromitite and enveloping dunite are clearly younger than the surrounding harzburgite. The spinel from the chromitite and dunite are beyond the compositional range of MORB-related spinels, while within the compositional range of arc-related plutonic rocks (Arai et al., 2011) (Fig. 2-11). The spinel chemistry of discordant chromitites suggests that the magma involved in their formation was arc-related magma, such as boninite (Arai et al., 2011; Miura et al., 2012) (Fig. 2-11). This is consistent with the trace-element characteristics of clinopyroxene from the dunite envelopes (Fig. 2-14). Calculated compositions of the melt in equilibrium with clinopyroxenes from the dunite enveloping discordant pods show the characteristics of arc-related magmas, especially boninite (Fig. 2-14). Its characteristics are actually analogous to those of boninite found in the northern Oman ophiolite (Ishikawa et al., 2005), as well as of the boninitic melt expected to be in equilibrium with the harzburgite-dunite-orthopyroxenite suite, from the northern Oman ophiolite (Tamura and Arai 2006). However, trace-element characteristics of clinopyroxene from dunite enveloping the Hilti concordant pod also show arc-related characteristics such as boninites in spite of its sub-oceanic features in terms of spinel chemistry of chromitite and associated peridotites (Fig. 2-11).

These observations strongly indicate that the melt/harzburgite reaction at low-P condition plays an important role in the evolution or formation of boninitic magma in

the mantle (e.g., Fisk 1986; Klingenberg and Kushiro 1996). The melt/harzburgite reaction at low-P condition may produce Si- and Mg- rich melt, like boninitic melt, as a result of assimilation of orthopyroxene and clinopyroxene in harzburgite (e.g., Fisk 1986; Kelemen 1990). The boninitic Si-rich melts, which were produced by the reaction, could be involved in the formation of chromitite (e.g., Arai and Yurimoto 1994; Zhou et al., 1994). The melt/harzburgite reaction and subsequent melt mixing leaves dunite with chromitite along the passage of the involved melt (e.g., Arai 1997). The enrichment of Na and LREE in clinopyroxene in the harzburgites adjacent to the dunite enveloping Hilti discordant pod (Fig. 2-12 and 14), relative to that in the distal harzburgites, was due to concentrations of these elements during the melt/wall harzburgite reaction (cf., Arai et al., 1997). The concentration of modal orthopyroxene in the proximal harzburgite may be due to the addition of Si-rich melt, produced by the reaction, to the wall harzburgite, not only to the conduit side (e.g., Arai and Yurimoto 1994; Zhou et al., 1994). The involvement of the melt rich in SiO_2 and incompatible elements during the formation of the chromitite-dunite suite is supported by the existence of primary inclusions composed of pyroxenes and hydrous minerals (Fig. 2-9).

2.8.3: *The conversion of oceanic mantle to sub-arc mantle*

The Cr# of spinels in ordinary harzburgites from the Oman ophiolite is generally less than 0.6 (e.g., Kelemen et al., 1995; Le Mée et al., 2004), indicating their abyssal nature (e.g., Kelemen et al., 1995; Arai et al., 2011). The harzburgites 8-10m from contact with dunite around the Hilti discordant chromitites are similar to the ordinary Oman harzburgites, and are equivalent to the abyssal harzburgites in terms of spinel chemistry (Arai et al., 2011) (Figs. 2-11 & -12). The highly LREE-depleted clinopyroxene is also one of features of abyssal peridotites (e.g., Dick and Natland 1996). Conversely, spinels from the harzburgites adjacent (~4 m from the contact point A) to the discordant chromitites are beyond the compositional range of MORB-related spinels, and well within that of arc-related plutonic rocks (Arai et al., 2011) (Figs. 2-11 & -12). The proximal harzburgite shows more depleted features in the spinel Cr# and HREE content of clinopyroxene (Figs. Figs. 2-12 & -14) than distal one. The slight

enrichment of LREE in clinopyroxene is characteristic of the sub-arc harzburgites (e.g., Ishimaru et al., 2007). This part of the harzburgites shows characteristics of the sub-arc mantle. We can see the contact/transition between the oceanic mantle and the sub-arc mantle along the transect A-A' (Figs. 2-3, -12 & -13). This transition between the two types of mantle, oceanic and arc-like, is in less than 4 m (Fig. 2-12).

This characteristics of surrounding harzburgite and two types of chromitite pods indicate the conversion of abyssal harzburgite to arc mantle (arc harzburgite + dunite + chromitite) through reaction with olivine-oversaturated melt (possibly basaltic) (e.g., Fisk 1986) (Fig. 2-14). This in turn reflects the transformation of the lithospheric mantle formed beneath a spreading ridge to a sub-arc mantle, along with a switch of tectonic setting to subduction mode (cf., Arai et al., 2006; Takazawa 2012).

2.9: Figures and Tables

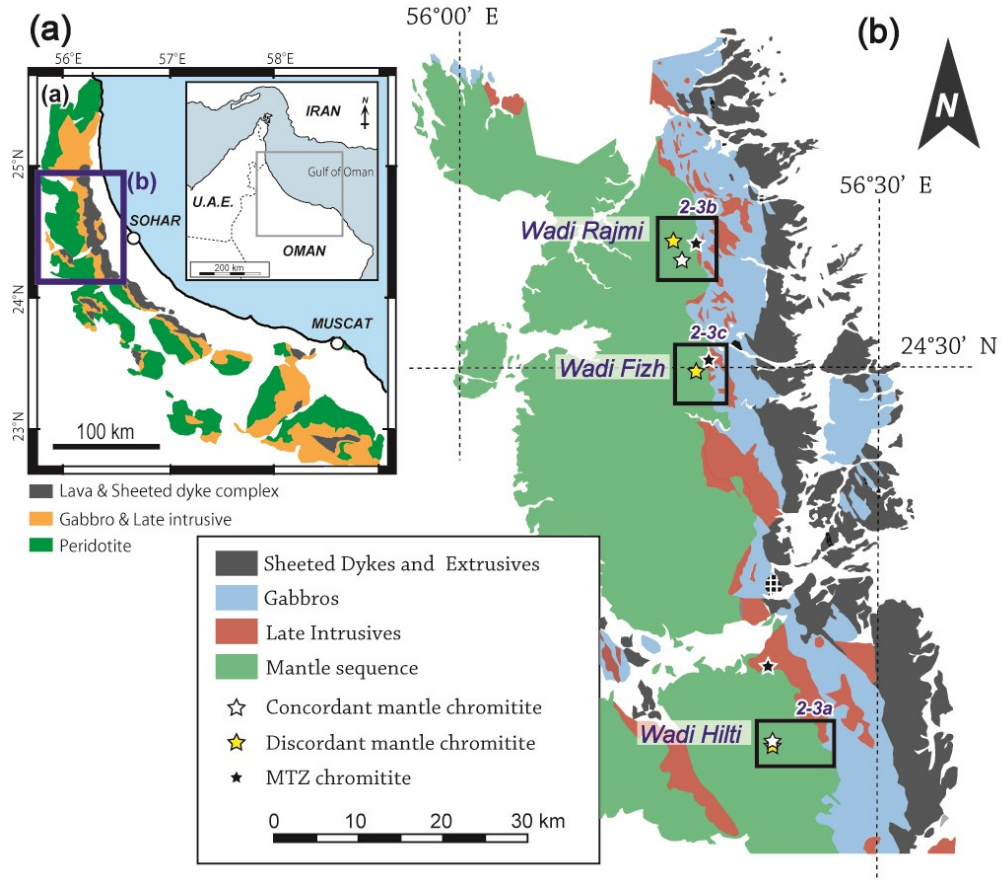

Figure 2-1. Geological maps of northern Oman ophiolite. Star symbols indicate sampling sites of chromitite pods. Modified from Lippard et al. (1986), Ahmed and Arai (2003) and Takazawa et al. (2003).

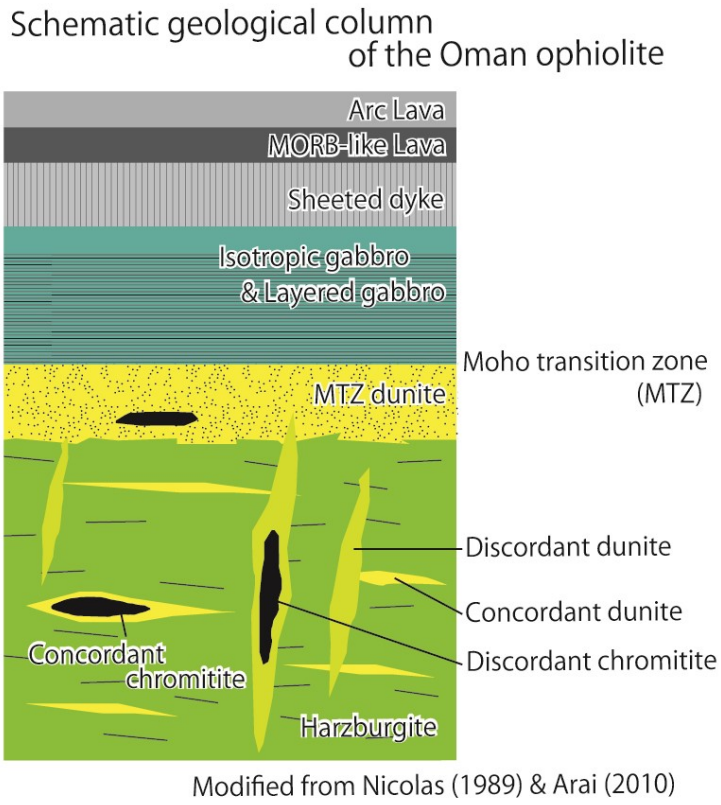

Figure 2-2. Schematic representation of the occurrence of ophiolitic chromitites. Modified from Nicolas (1989) and Arai (2010).

Fig. 2-3a *Wadi Hilti*

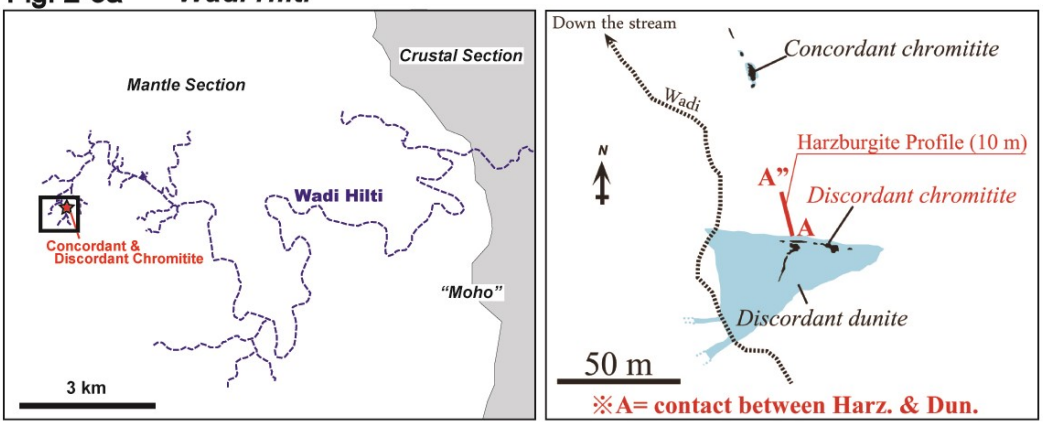

Fig. 2-3b *Wadi Rajmi*

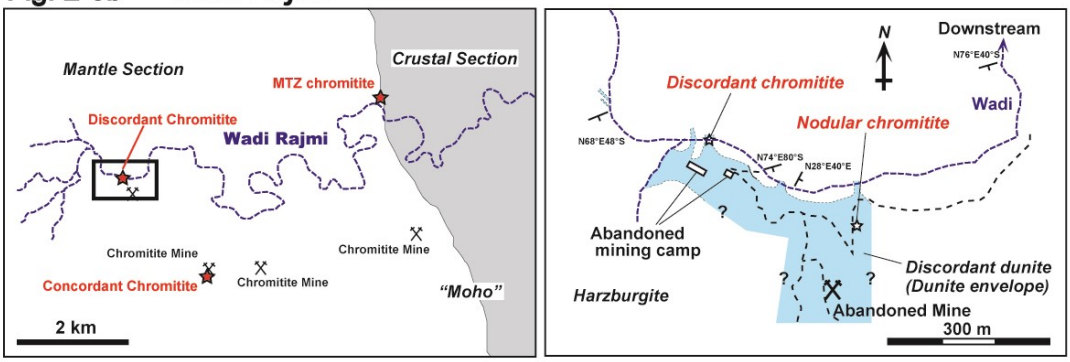

Fig. 2-3c *Wadi Fizh*

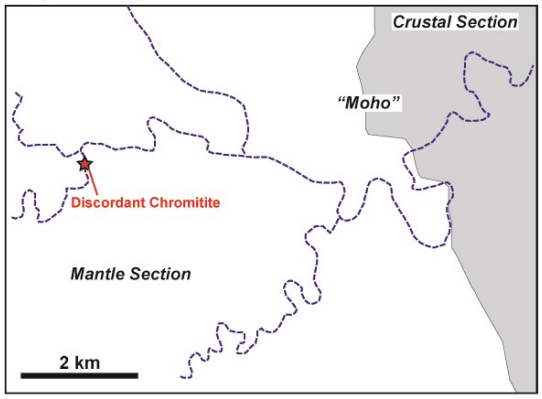

Figure 2-3. Locality maps of studied chromitite pods in Wadi Hilti, Rajmi and Fizh areas, northern Oman ophiolite.

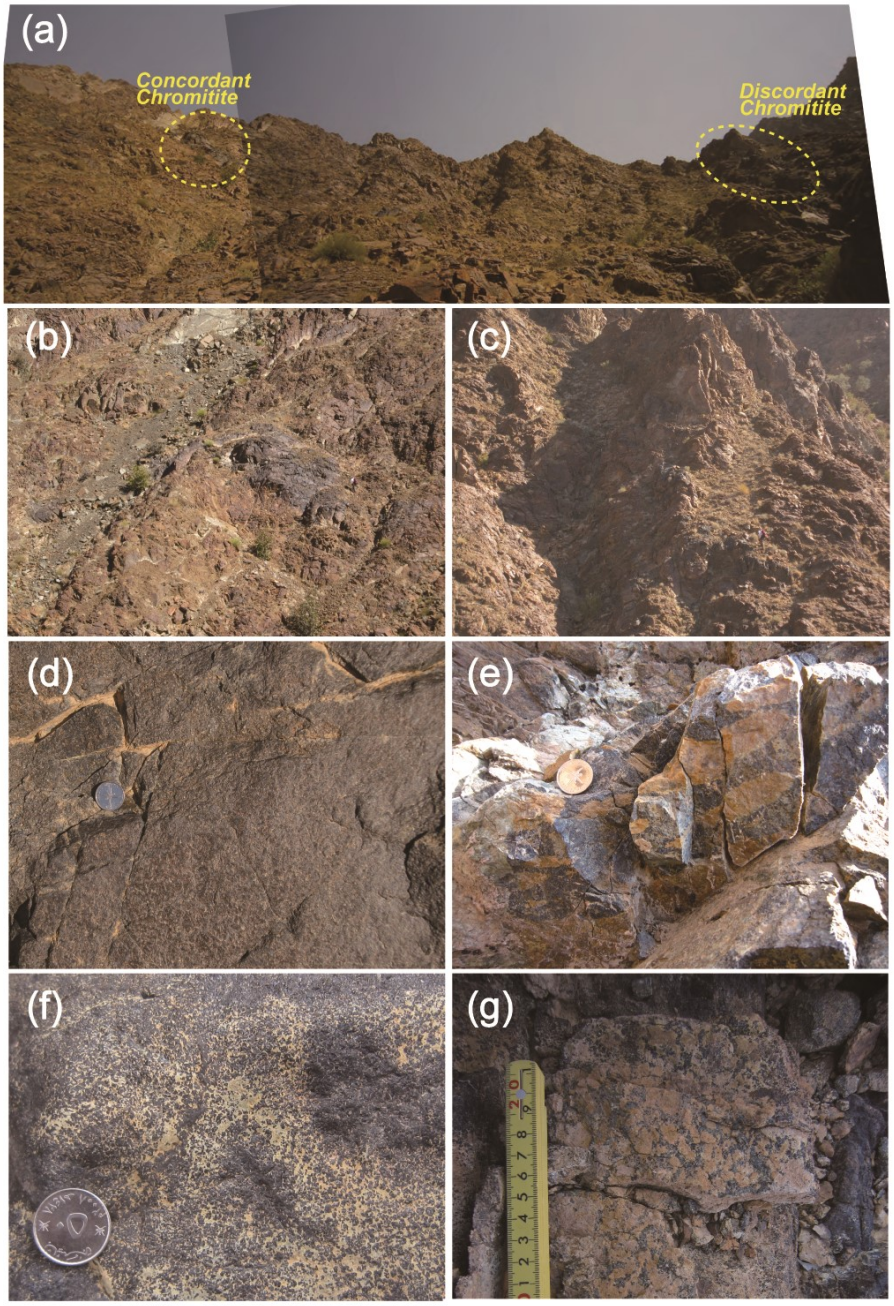

Figure 2-4. Modes of occurrence of the concordant and discordant chromitites from Wadi Hilti, northern Oman ophiolite. (a) Panoramic view of two types of chromitite on the same cliff (Ahmed and Arai 2002; Miura et al., 2012). (b) Concordant to subconcordant chromitite. (c) Discordant chromitite and surrounding thick dunite envelope. (d) Massive and homogeneous texture of the concordant chromitite. (e) Anti-nodular texture of the concordant chromitite. (f) Heterogeneously disseminated texture of the discordant chromitite. (g) Anti-nodular texture of the discordant chromitite.

Figure 2-5. Modes of occurrence of the discordant chromitites from Wadi Rajmi. (a) Anti-nodular texture appears in the boundary between the massive chromitite pod and spinel-rich dunite. (b) Massive-textured chromitite pod in spinel rich dunite. (c) Nodular textured chromitite pod in spinel-rich dunite from an abandoned mine. Note that nodular textured part gradually change to disseminated textured part. (d) An enlarged photo of nodular textured chromitite on photo (c). (e) An enlarged photo of nodular to disseminated textured chromitite on photo (c). (f) Anti-nodular textured part of a boulder massive chromitite. (g) Dunitic patch in disseminated to massive chromitite. (h) Contact between surrounding harzburgite and thick dunite enveloping the Rajmi discordant chromitite. Note that dunite is discordant to the foliation of surrounding harzburgite.

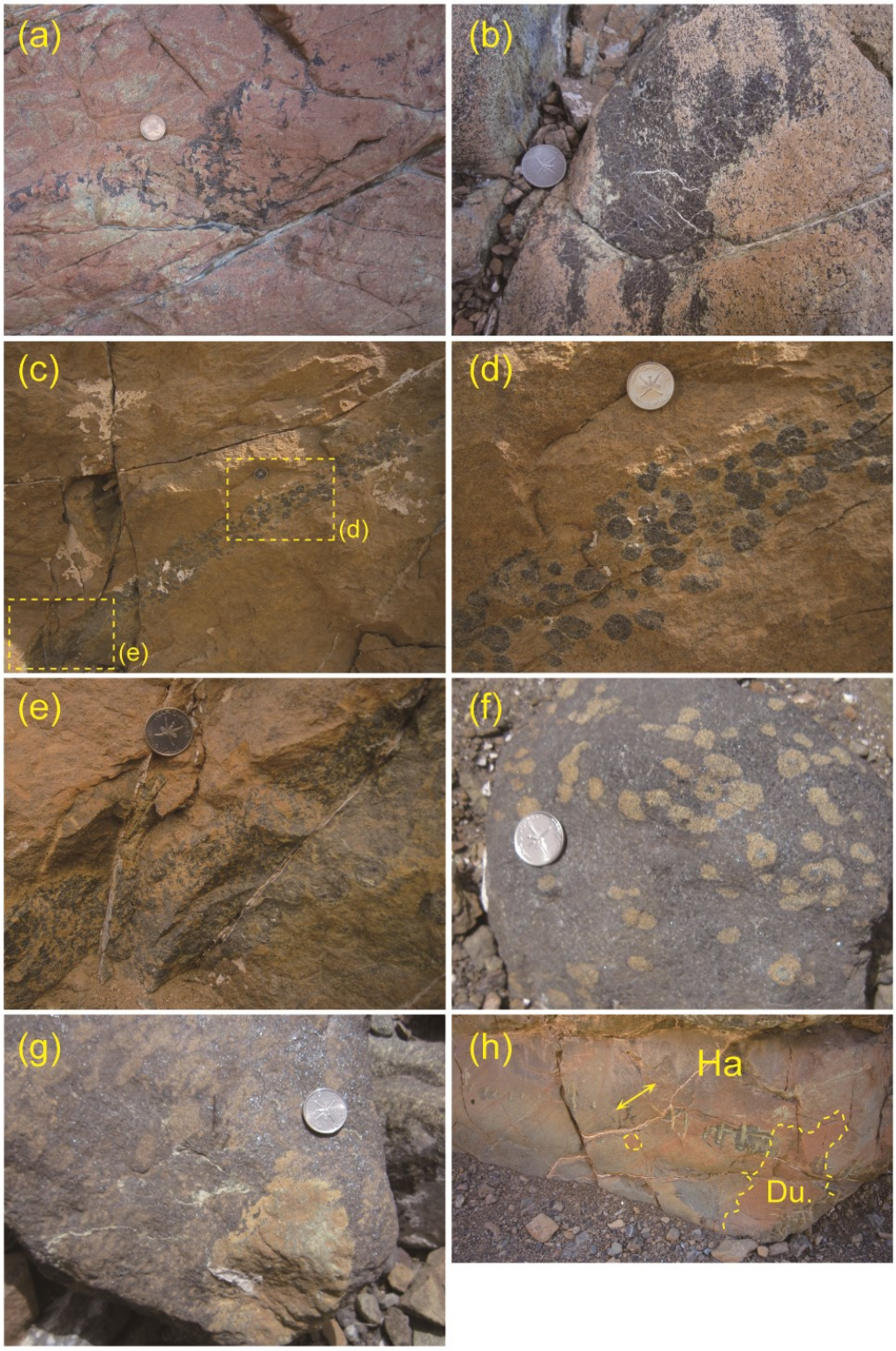

Figure 2-5.

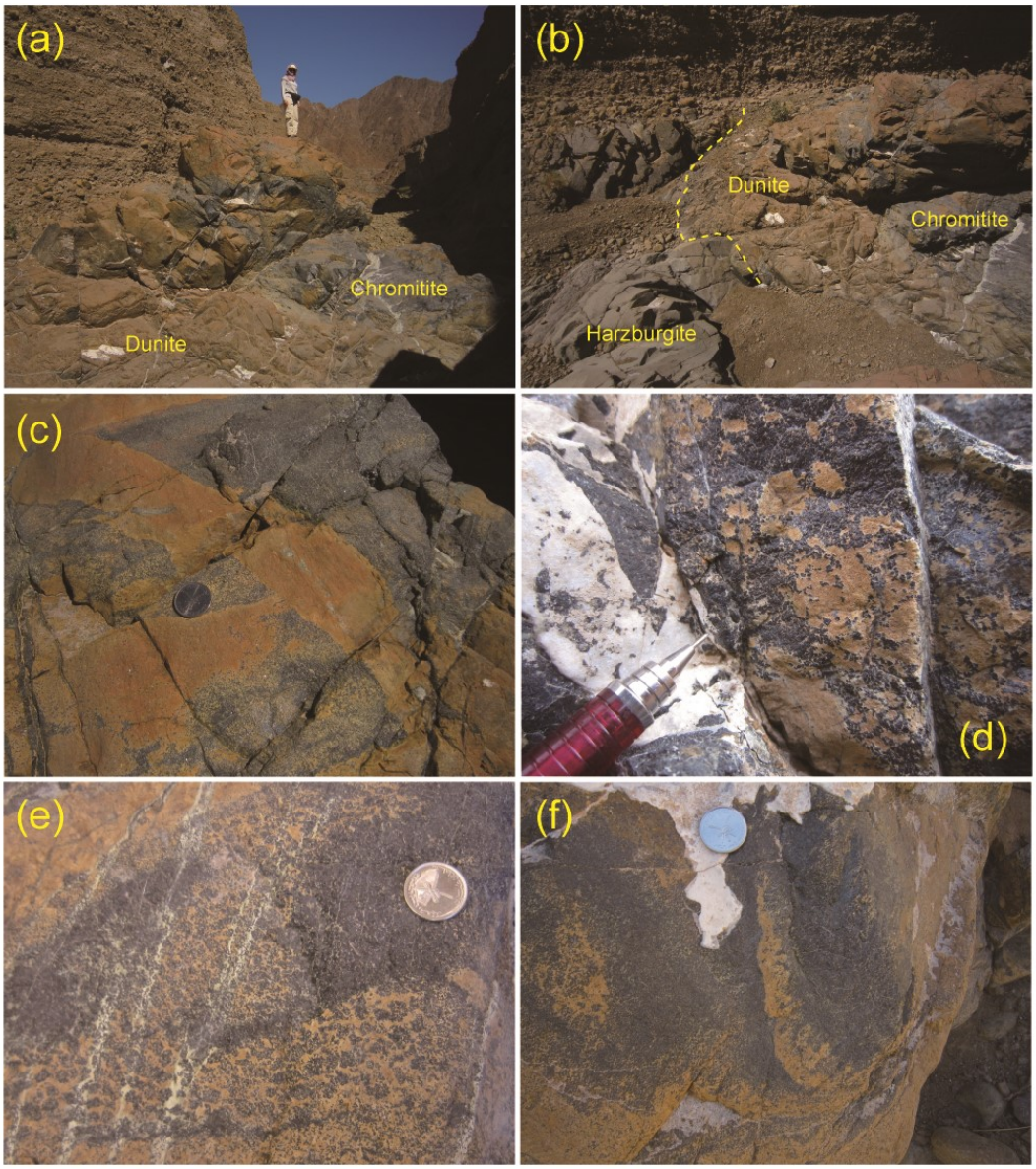

Figure 2-6. Field occurrences of the discordant chromitites from Wadi Fizh. (a) Entire discordant chromitite pod. (b) Boundary of surrounding harzburgite, dunite envelope and chromitite. Note that the dunite envelope and chromitite are discordant to the foliation of surrounding harzburgite. (c) Dunitic vein in massive to anti-nodular textured chromitite. (d) Anti-nodular textured part of chromitite. (e) Massive to disseminated part gradually changing to nodular textured part. (f) Disseminated and massive part gradually changing to nodular textured part in dunitic pocket.

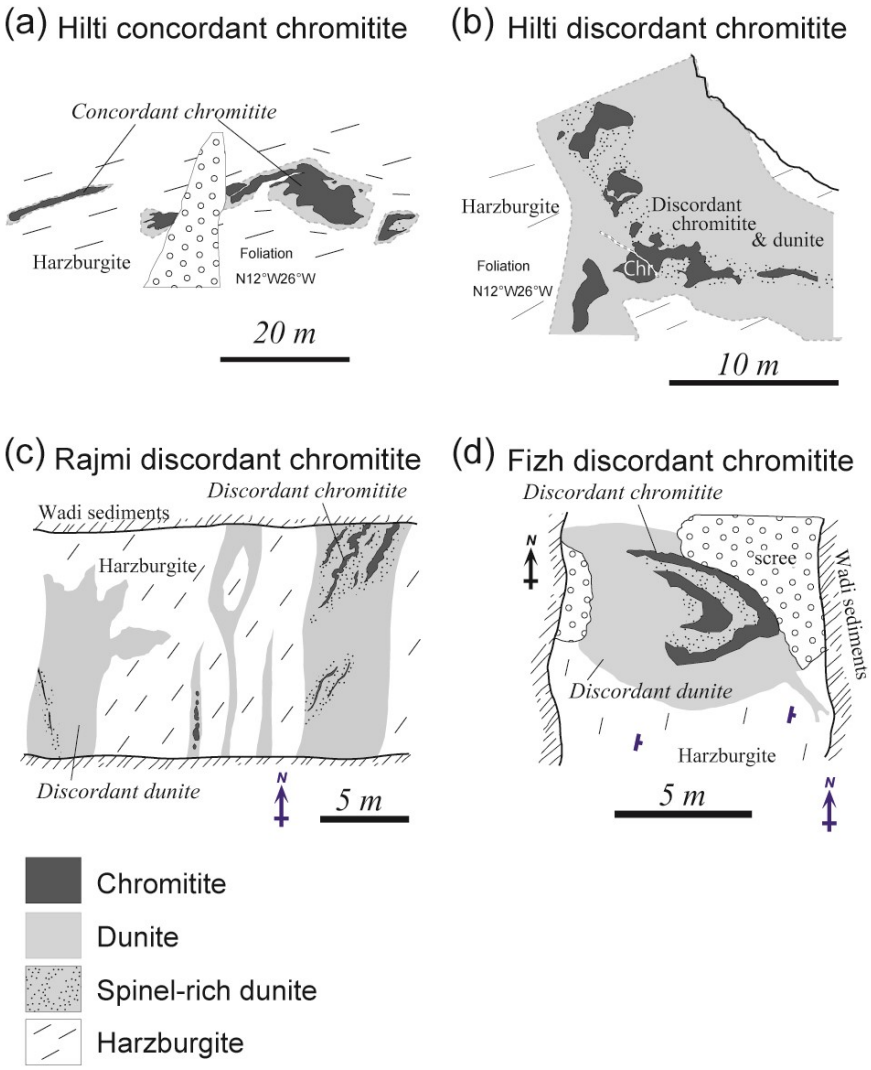

Figure 2-7. Sketches of mantle chromitites from northern Oman ophiolite. Attitudes of the surrounding harzburgite foliation are shown. (a) The occurrence of the Hilti concordant to subconcordant chromitite. (b) The appearance of the Hilti discordant chromitite. (c) Sketch of the Rajmi discordant chromitite pods in plan. (d) Sketch of the Fizh discordant chromitite pods in plan.

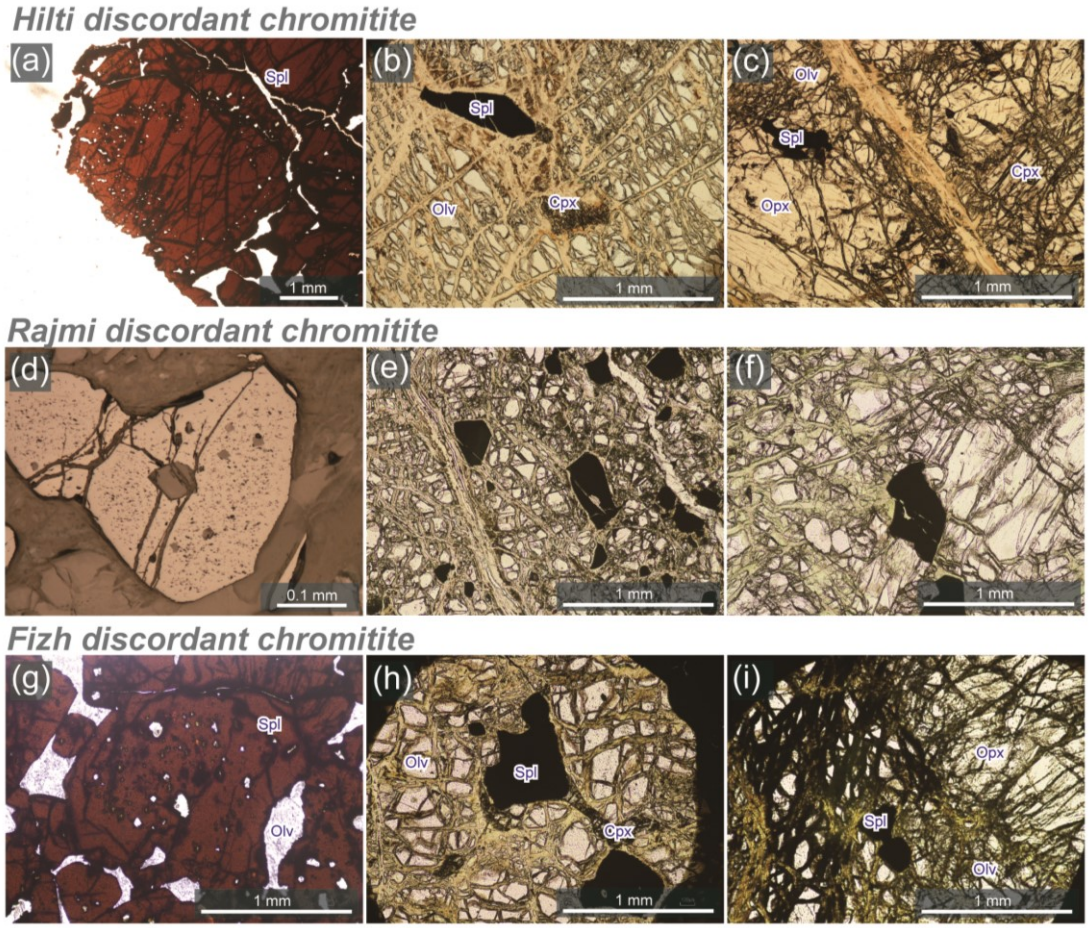

Figure 2-8a-i. Photomicrographs of chromitites, dunite envelopes and surrounding harzburgites from Wadi Hilti (a-c, j-l), Rajmi (d-f, m-q) and Fizh (g-i). Abbreviations; Olv, olivine; Spl, spinel; Opx, orthopyroxene; Cpx, clinopyroxene; Amp, amphibole; Fel, feldspar. Note that olivines in the dunite enveloping Hilti concordant pod and in the Rajmi concordant chromitite are kinked, suggesting deformation.

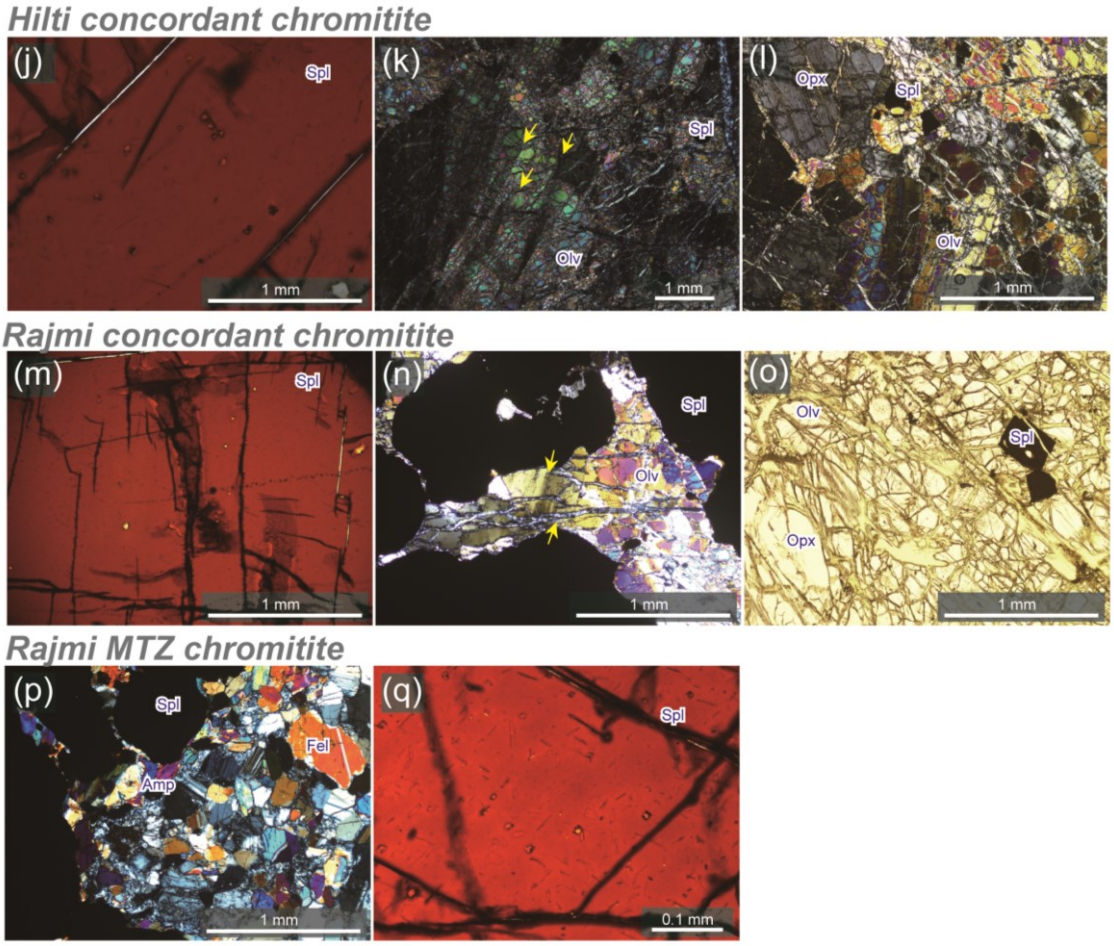

Figure 2-8j-q. Photomicrographs of chromitites, dunite envelopes and surrounding harzburgites from Wadi Hilti (a-c, j-l), Rajmi (d-f, m-q) and Fizh (g-i). Abbreviations; Olv, olivine; Spl, spinel; Opx, orthopyroxene; Cpx, clinopyroxene; Amp, amphibole; Fel, feldspar. Note that olivines in the dunite enveloping Hilti concordant pod and in the Rajmi concordant chromitite are kinked, suggesting deformation.

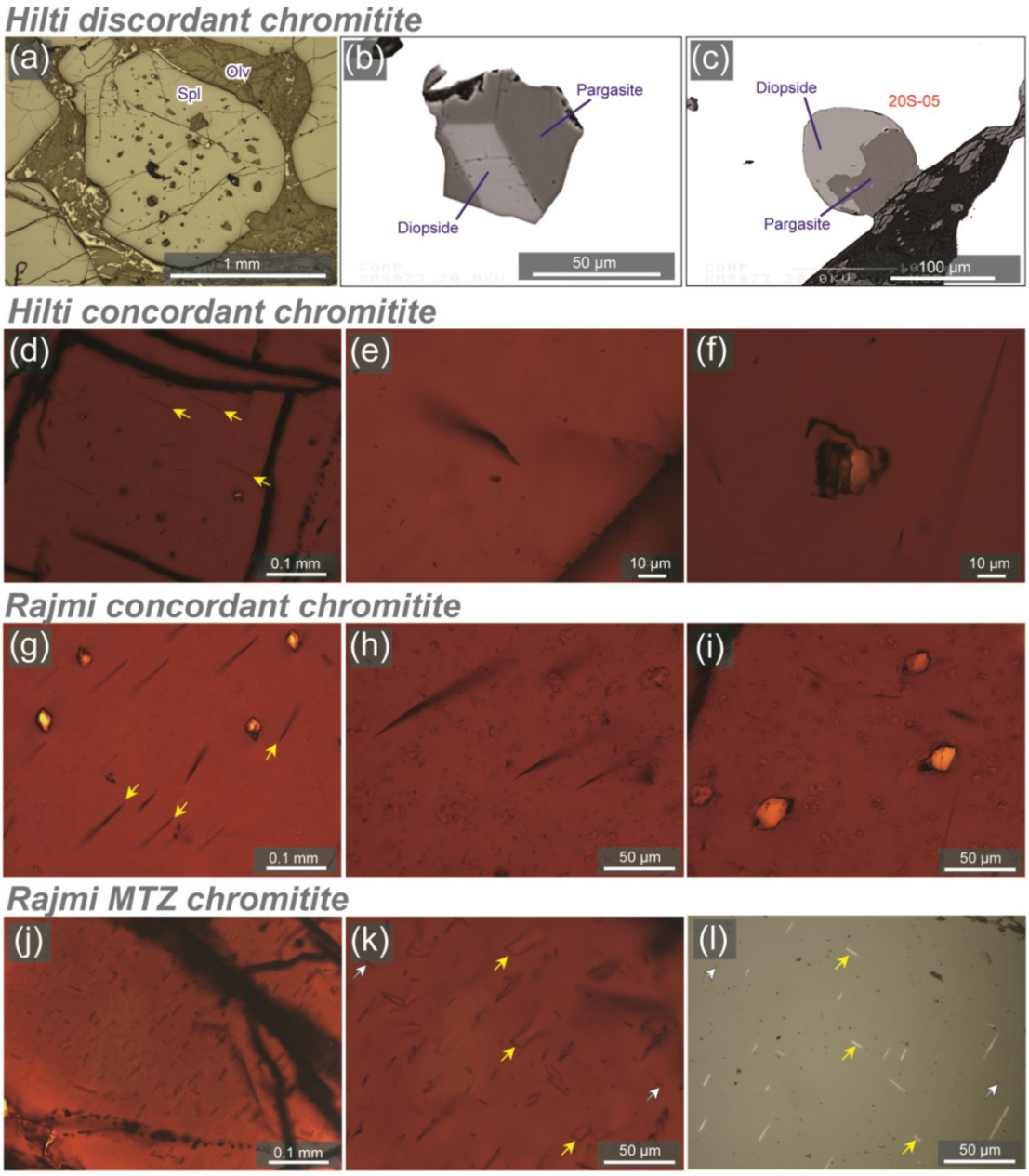

Figure 2-9. Photomicrographs of inclusions in spinel from chromitites of northern Oman ophiolite. Orbicular inclusions in the discordant chromitites (a-c), Lamellar inclusions in spinels from the Hilti and Rajmi concordant pods (d-i) and the Rajmi MTZ chromitite (j-l). Yellow arrow indicates exsolution lamellae.

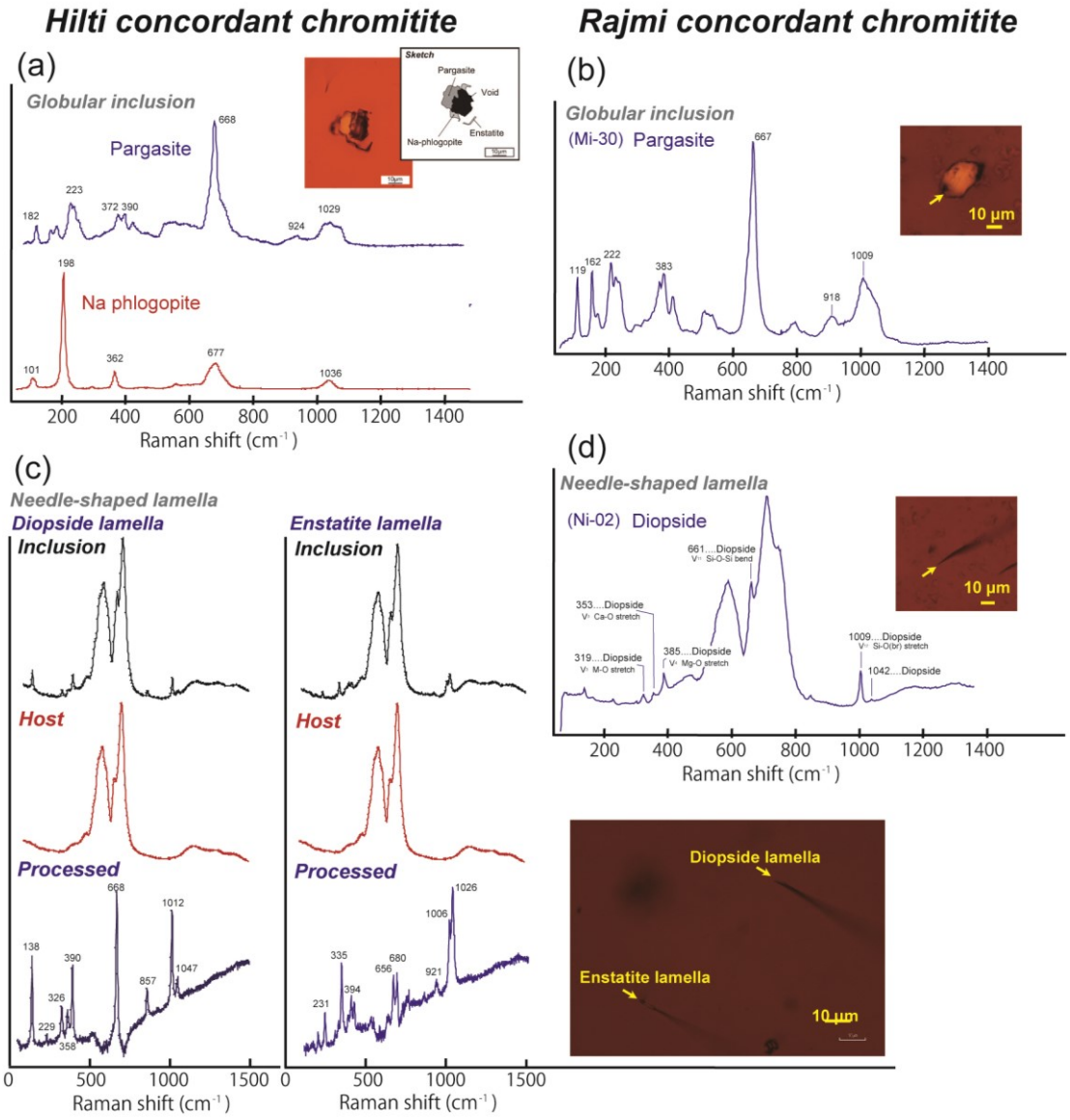

Figure 2-10. Raman spectra of micro-inclusions in spinel from the Hilti and Rajmi concordant pods.

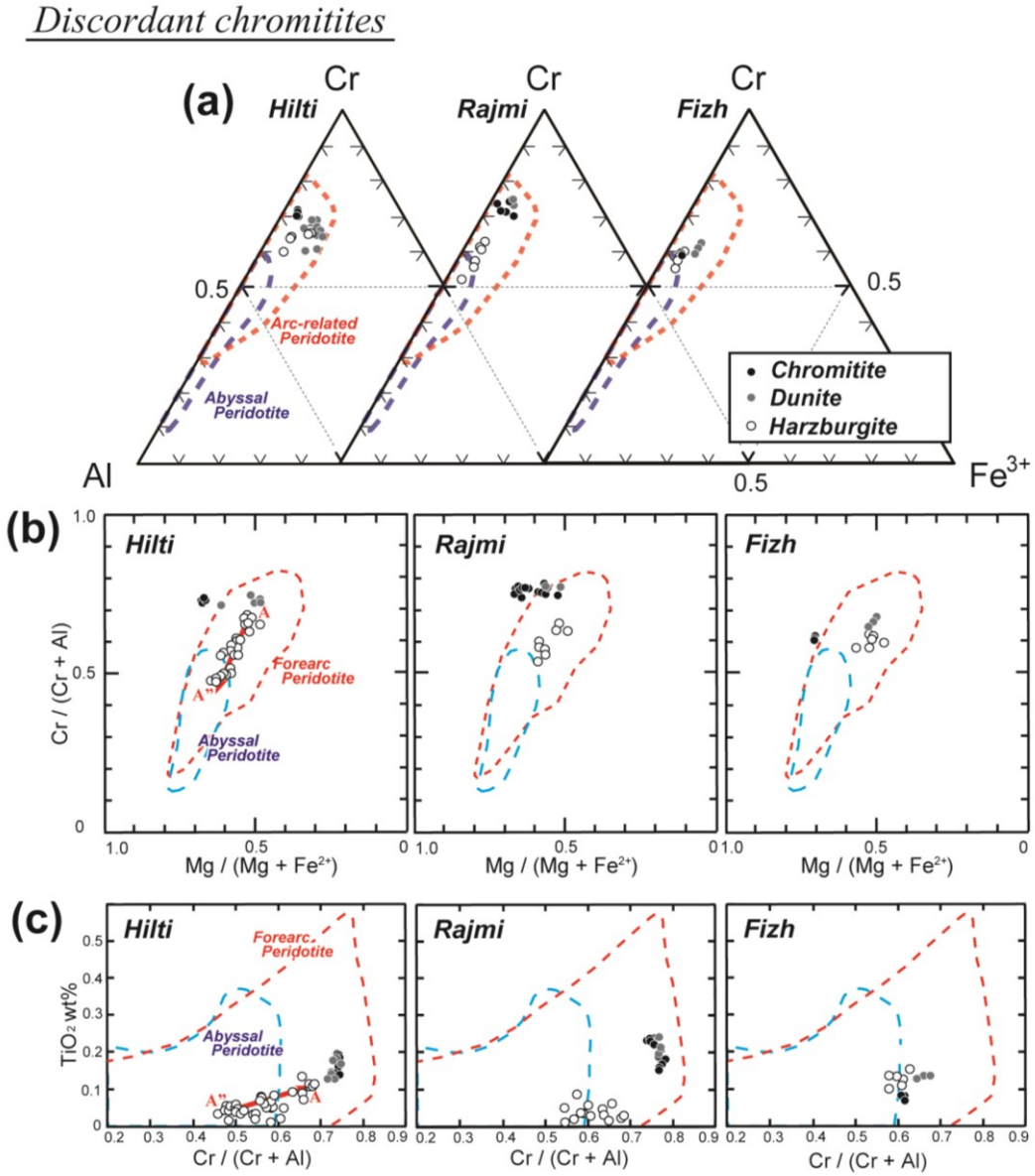

Figure 2-11a-c. Major-element chemical characteristics of minerals in chromitites, dunite envelope and surrounding harzburgite. Abyssal peridotite fields are from Dick and Bullen (1984), Arai (1994) and Arai et al. (2011). Arc-related peridotite fields are from Arai and Ishimaru (2008) and Arai et al. (2011). Olivine Mantle Array is from Takahashi et al. (1987). Abyssal peridotite field in (h) are from Tamura et al. (2008). (a) Trivalent cation ratios of chromian spinels from the Hilti, Rajmi and Fizh discordant pods. (b) Relationships between Mg# and Cr# of spinels from discordant pods. (c) Relationships between Cr# and TiO_2 content of spinels from discordant pods.

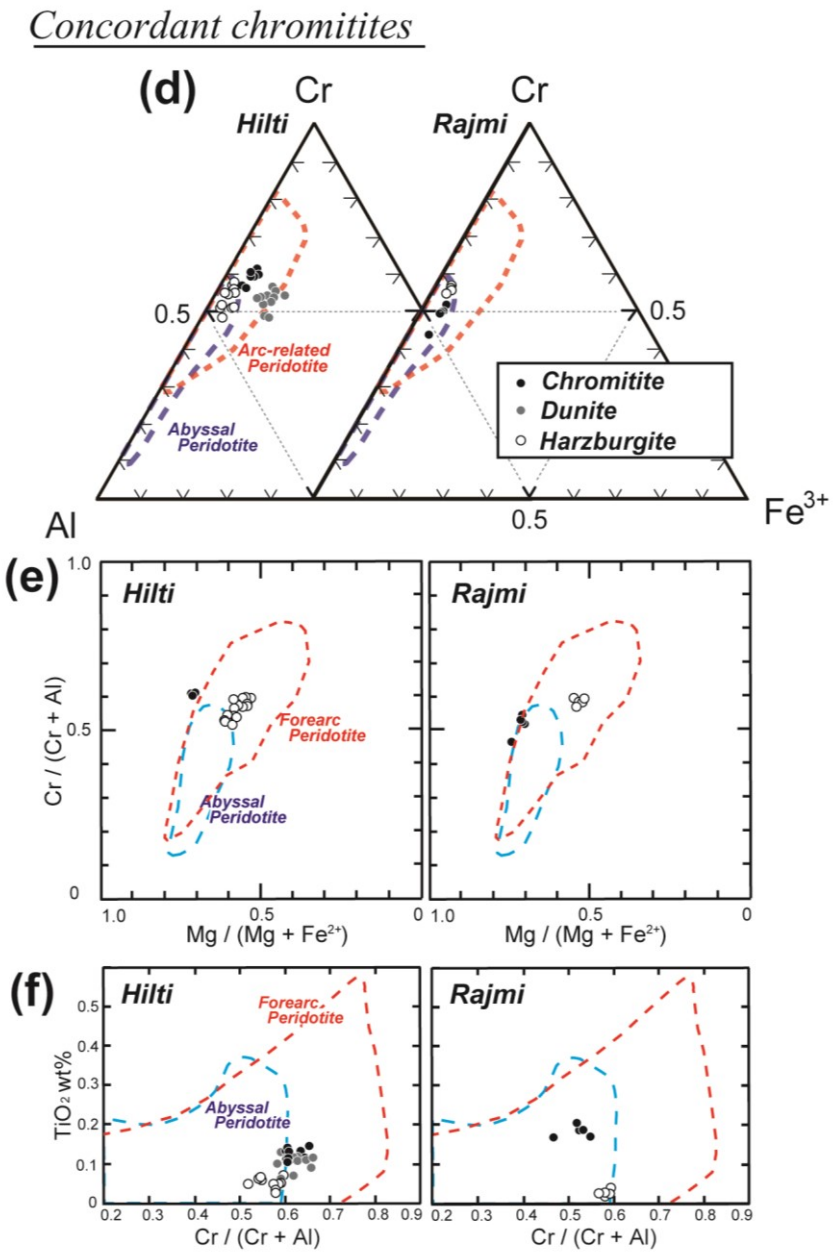

Figure 2-11d-f. Major-element chemical characteristics of minerals in chromitites, dunite envelope and surrounding harzburgite. (d) Trivalent cation ratios of chromian spinels from the Hilti and Rajmi concordant pods. (e) Relationships between Mg# and Cr# of spinels from concordant pods. (f) Relationships between Cr# and TiO_2 content of spinels from concordant pods.

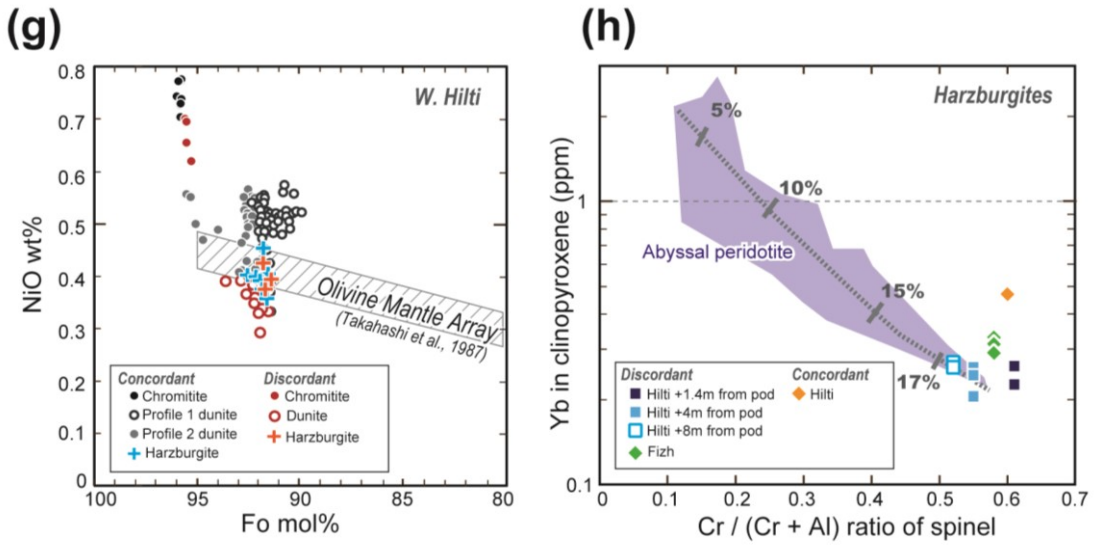

Figure 2-11g-h. Major-element chemical characteristics of minerals in chromitites, dunite envelope and surrounding harzburgite. (g) Relationships between Fo mol% and NiO content of olivines from the concordant and discorsant chromitite pods of Wadi Hilti. Note that olivines in dunite enveloping concordant pod show high Ni contents. (h) Relationships between Cr# of spinel and Yb content of clinopyroxene from harzburgites surrounding the Hilti discordant pods. Numbers on gray line indicate the degree of partial melting.

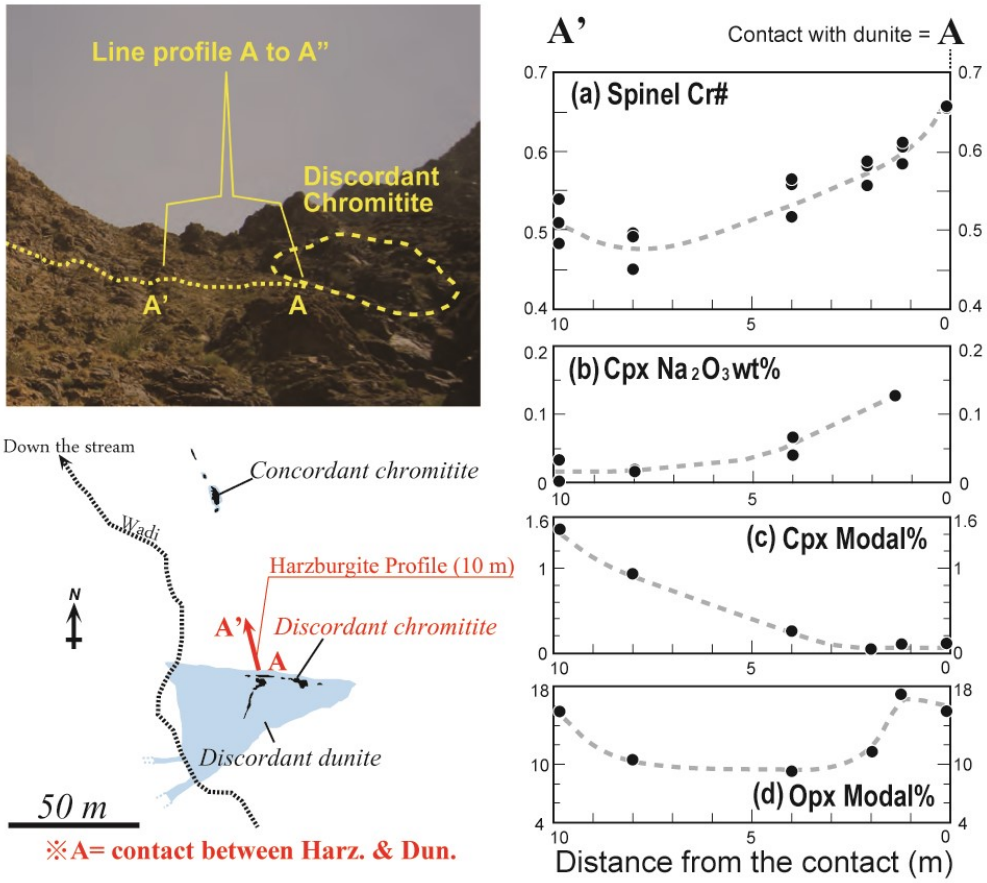

Figure 2-12. Chemical profiles of harzburgites surrounding the Hilti discordant chromitite. Modified from Miura et al. (2014).

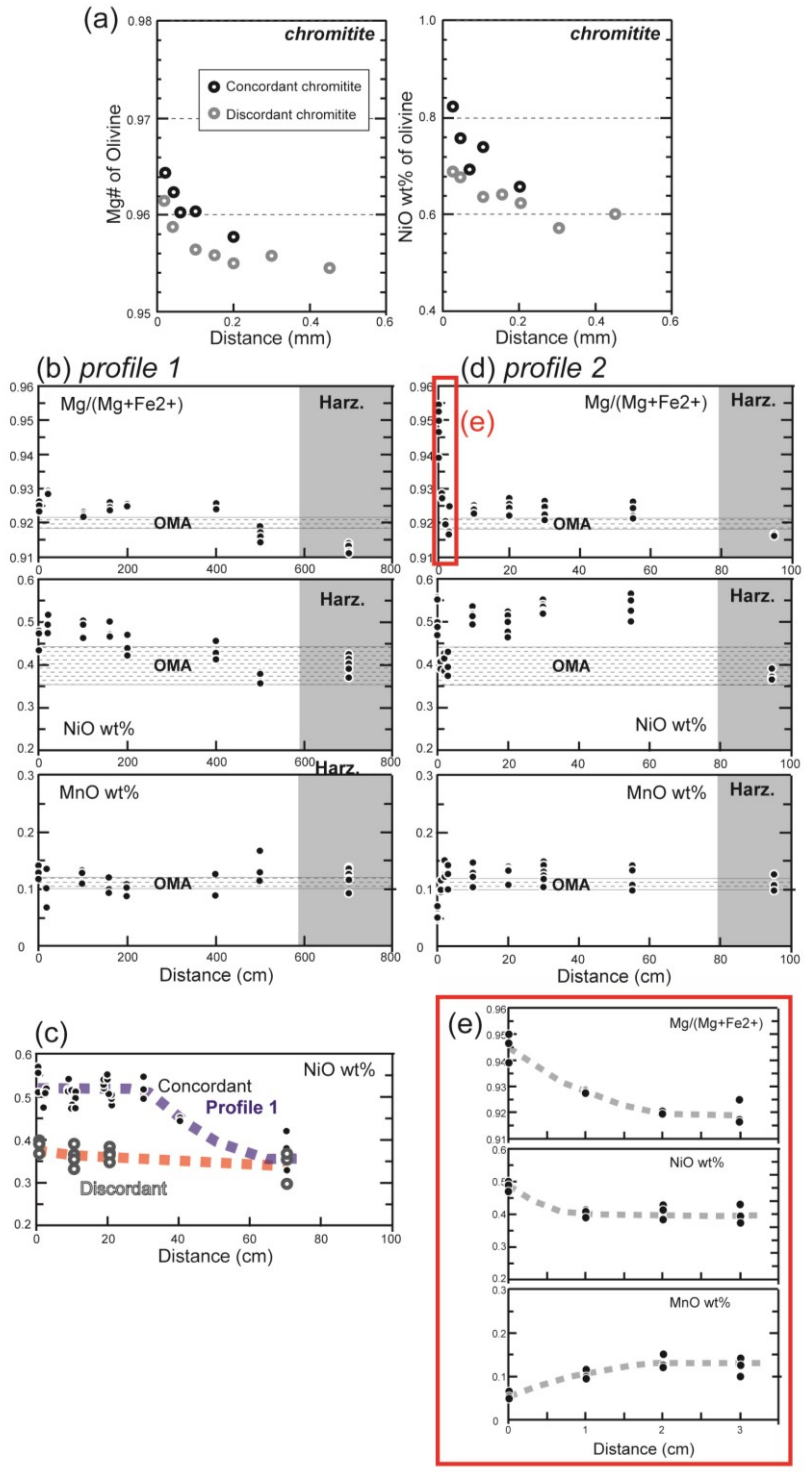

Figure 2-13. Profile of Mg# and Ni content in olivine from dunite enveloping Hilti concordant and discordant chromitite. (a) Mg# and Ni profiles of olivines from the concordant and discordant chromitite. (b, d, e) Dunite enveloping concordant chromitite. (c) Compositional profiles of olivine from dunite enveloping both types of chromitite.

Figure 2-14. Chondrite-normalized trace element patterns of clinopyroxenes in the Hilti (a-d) and Fizh (e-f) chromitites, dunite and surrounding harzburgite. Harzburgite, orthopyroxenite and boninite fields are from Tamura and Arai (2006). Abyssal peridotites field is from Tamura et al. (2008). N-MORB pattern is from Sun and McDonough (1989). (a) Clinopyroxenes in the dunite envelope, surrounding harzburgites and chromitite from Wadi Hilti. Note that clinopyroxene show higher contents of LREE, e.g., Ce, in the adjacent harzburgites than in the distant harzburgites. (b) Calculated melt in equilibrium with clinopyroxene from dunite and chromitite. The Oman boninites (Ishikawa et al., 2005) and arc-related ultramafics (Tamura and Arai 2006) are shown for comparison. The partition coefficients of clinopyroxene/melt, reported by Sobolev et al. (1996) were used for the calculation of melt composition.

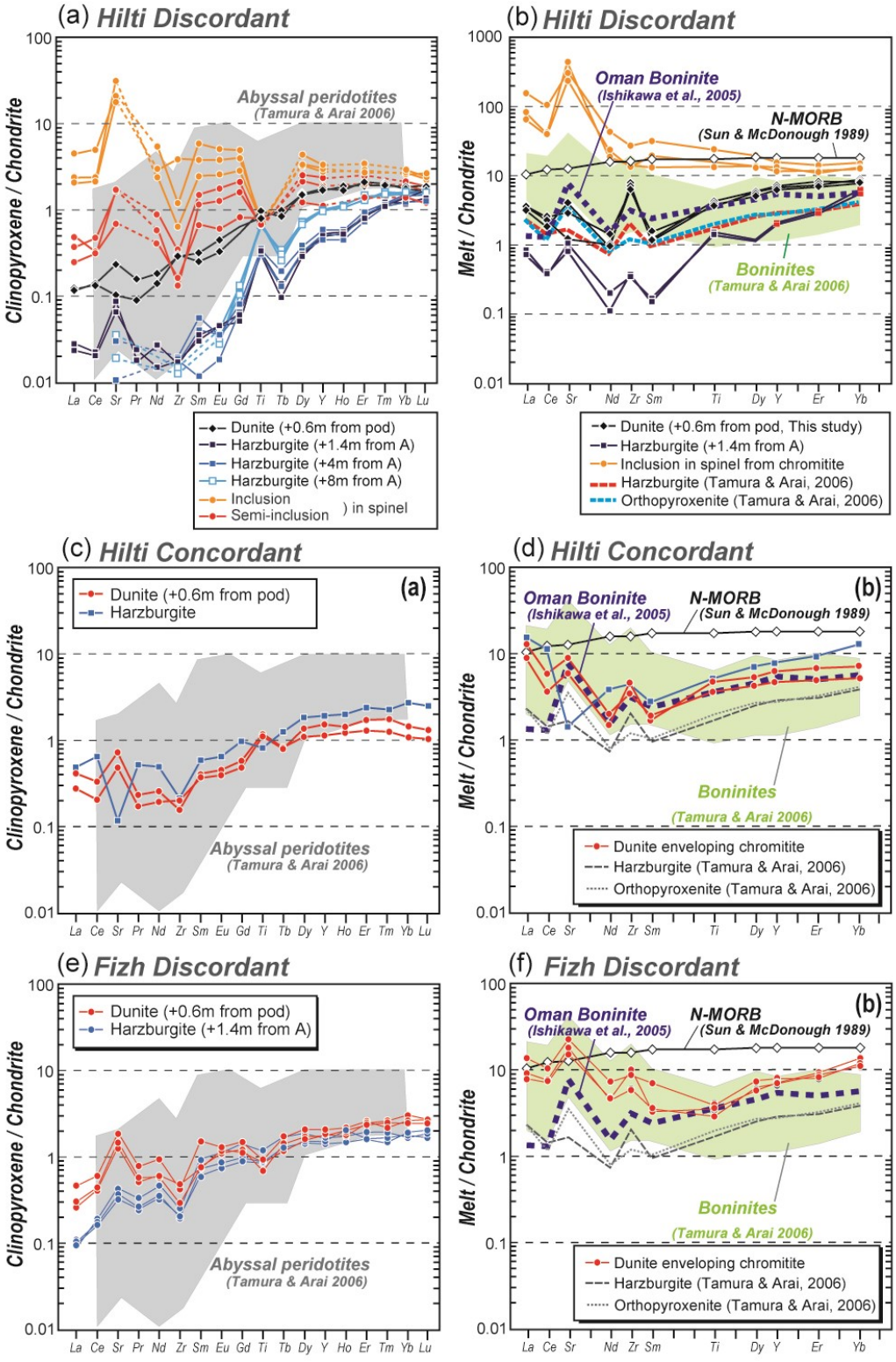
(a) Hilti Discordant
Clinopyroxene / Chondrite
Abyssal peridotites
(Tamura & Arai 2006)
Dunite (+0.6m from pod)
Harzburgite (+1.4m from A)
Harzburgite (+4m from A)
Harzburgite (+8m from A)
Inclusion
Semi-inclusion
) in spinel
(b) Hilti Discordant
Melt / Chondrite
Oman Boninite
(Ishikawa et al., 2005)
N-MORB
(Sun & McDonough 1989)
Boninites
(Tamura & Arai 2006)
Dunite (+0.6m from pod, This study)
Harzburgite (+1.4m from A)
Inclusion in spinel from chromitite
Harzburgite (Tamura & Arai, 2006)
Orthopyroxenite (Tamura & Arai, 2006)
(c) Hilti Concordant
Dunite (+0.6m from pod)
Harzburgite
(a)
Abyssal peridotites
(Tamura & Arai 2006)
(d) Hilti Concordant
(b)
Dunite enveloping chromitite
Harzburgite (Tamura & Arai, 2006)
Orthopyroxenite (Tamura & Arai, 2006)
(e) Fizh Discordant
Dunite (+0.6m from pod)
Harzburgite (+1.4m from A)
(f) Fizh Discordant
La Ce Sr Pr Nd Zr Sm Eu Gd Ti Tb Dy Y Ho Er Tm Yb Lu

Figure 2-14.

Sample	Distace from contact	Olivine	Opx	Spinel	Cpx	Ser.	Total %
DH1	+ 0.5 m	60.90	15.49	0.35	0.12	23.14	100
DH2	+ 1.2 m	64.57	17.13	1.06	0.11	17.13	100
DH3	+ 3.2 m	51.20	11.35	0.40	0.05	37.00	100
DH4	+ 4.2 m	50.37	9.33	1.20	0.27	38.84	100
DH6	+ 8.2 m	63.73	10.60	0.67	0.93	24.07	100
DH7	+ 10.0 m	72.42	15.45	1.11	1.46	9.55	100

Abbreviations: Opx, orthopyroxene; Cpx, clinopyroxene; Ser, serpentine.
Contact indicates the boundary between dunite envelope and surrounding harzburgites.

Table 2-1. Modal amounts of minerals in harzburgites surrounding the Hilti discordant chromitite pod. Contact indicates the boundary between dunite and harzburgites.

Table 2-2. Selected microprobe analysis of spinel in chromitite, dunite and harzburgite from the northern Oman ophiolite.

Wadi	Hilti	Hilti	Hilti	Hilti	Hilti	Hilti	Rajmi	Rajmi	Rajmi	Rajmi	Fizh	Fizh	Fizh
		Discordant						Discordant				Discordant	
Rock type	Chr.	Dun.	Har.	Har.	Har.	Har.	Chr.	Chr.	Dun.	Har.	Chr.	Dun.	Har.
Remarks		envelope	proximal	proximal	proximal	ambient			envelope	proximal		envelope	proximal
Texture	Mas.		*0.5m*	*1.2 m*	*4.2 m*	*8.2 m*	Nod.	Dis.			Mas.		
Sample	HD20-42	HD26-48	HD28-62	DH2	DH4	DH6	RNC5	WR3-3-4	RND7	WR3-9	FZC1	FZD1	FZH
SiO_2	0.00	0.00	0.00	0.00	0.00	0.00	0.00	0.00	0.00	0.00	0.00	0.01	0.01
TiO_2	0.13	0.18	0.11	0.05	0.07	0.05	0.23	0.21	0.24	0.03	0.07	0.13	0.12
Al_2O_3	13.28	12.56	15.85	20.09	23.89	28.88	12.24	11.60	12.98	20.82	20.76	17.91	20.26
Cr_2O_3	55.39	51.07	51.40	47.39	45.08	40.37	54.43	57.87	56.39	47.54	49.29	48.00	46.86
FeO*	15.91	25.47	20.77	20.64	17.55	17.48	21.47	17.25	18.13	18.60	14.77	23.10	21.60
MnO	0.29	0.41	0.31	0.33	0.24	0.26	0.32	0.33	0.29	0.27	0.17	0.30	0.33
MgO	14.17	10.08	11.27	12.26	13.65	14.50	11.80	13.31	10.74	12.66	15.80	11.44	11.06
CaO	0.01	0.00	0.00	0.01	0.00	0.00	0.00	0.00	0.01	0.00	0.00	0.03	0.00
Na_2O	0.05	0.00	0.00	0.01	0.00	0.00	0.00	0.01	0.00	0.01	0.00	0.02	0.00
K_2O	0.00	0.00	0.00	0.00	0.00	0.00	0.00	0.00	0.00	0.00	0.01	0.00	0.01
NiO	0.09	0.07	0.03	0.08	0.09	0.09	0.09	0.08	0.08	0.08	0.21	0.09	0.09
Total	99.31	99.84	99.75	100.85	100.56	101.62	100.59	100.65	98.85	100.01	101.07	101.03	100.34
Mg#	0.67	0.49	0.54	0.57	0.62	0.63	0.57	0.63	0.52	0.59	0.71	0.53	0.52
Cr#	0.74	0.73	0.69	0.61	0.56	0.48	0.75	0.77	0.75	0.61	0.61	0.64	0.61
$Cr/(Cr+Al+Fe^{3+})$	0.701	0.663	0.653	0.582	0.541	0.469	0.696	0.734	0.737	0.584	0.589	0.597	0.583
$Al/(Cr+Al+Fe^{3+})$	0.250	0.243	0.300	0.368	0.428	0.500	0.233	0.219	0.253	0.381	0.370	0.332	0.376
$Fe^{3+}/(Cr+Al+Fe^{3+}$	0.049	0.094	0.047	0.051	0.031	0.031	0.071	0.046	0.010	0.034	0.041	0.070	0.041

Abbreviations: Chr = chromitite, Dun = dunite, Har = harzburgite, C-Har = clinopyroxene-bearing harzburgite
Mas = massive, Nod = nodular, Dis = disseminated

Wadi	Hilti	Hilti	Hilti	Rajmi	Rajmi
		Concordant			
Rock type	Chr.	Dun.	Har.	Chr.	Har.
Remarks		envelope	proximal		proximal?
Texture	Mas.	*contact*			
Sample	HC8-7	HC7-8	HC4-29	K29	KSH-29
SiO_2	0.00	0.00	0.00	0.00	0.00
TiO_2	0.13	0.11	0.05	0.19	0.03
Al_2O_3	18.77	15.93	22.70	25.77	21.76
Cr_2O_3	48.15	43.09	45.37	42.63	45.81
FeO*	18.53	28.57	19.46	15.12	20.64
MnO	0.28	0.38	0.33	0.20	0.36
MgO	13.02	9.91	11.99	16.26	11.34
CaO	0.00	0.02	0.00	0.00	0.01
Na_2O	0.00	0.01	0.00	0.00	0.00
K_2O	0.00	0.00	0.00	0.00	0.00
NiO	0.14	0.18	0.03	0.18	0.05
Total	99.02	98.18	99.93	100.35	99.99
Mg#	0.61	0.48	0.55	0.72	0.53
Cr#	0.63	0.64	0.57	0.53	0.59
$Cr/(Cr+Al+Fe^{3+})$	0.601	0.559	0.556	0.502	0.566
$Al/(Cr+Al+Fe^{3+})$	0.349	0.308	0.415	0.452	0.401
$Fe^{3+}/(Cr+Al+Fe^{3+}$	0.049	0.133	0.029	0.046	0.033

Table 2-2. Selected microprobe analysis of spinel in chromitite, dunite and harzburgite from the northern Oman ophiolite. Mg# = $Mg/(Mg+Fe^{2+})$, Cr#=Cr/(Cr+Al).
FeO* is total iron as FeO.

Table 2-3. Selected microprobe analysis of spinel in chromitite, dunite and harzburgite from the northern Oman ophio

Wadi	Hilti	Hilti	Hilti	Hilti	Rajmi	Rajmi	Rajmi	Fizh	Fizh	Hilti	Hilti	Hilti	Hilti	Hilti	Rajmi	Rajmi
		Discordant				Discordant		Discordant				Concordant				Concordant
Rock type	Chr.	Dun.	Har.	Har.	Chr.	Dun.	Har.	Dun.	Har.	Chr.	Dun.	Dun.	Dun.	Har.	Chr.	Har.
Remarks		envelope	proximal	ambient		envelope	proximal	envelope	proximal		envelope	envelope	envelope	proximal		proximal?
Texture	Mas.				Dis.					Mas.	*contact*	*30cm*	*100cm*		Mas.	
Sample	HD3	HD22-53	DH1	DH6	WR3-3-4	WR3-6	WR3-9	FZD1	FZH	HP1-14	SD6-1	SD4-6	SD4-9	HC4-33	K29	KSH-29
SiO_2	42.27	41.24	41.71	42.18	41.16	41.51	41.02	41.77	40.86	41.66	41.55	42.15	42.42	41.46	42.59	40.12
TiO_2	0.00	0.00	0.00	0.05	0.00	0.04	0.00	0.00	0.01	0.00	0.05	0.01	0.00	0.00	0.00	0.00
Al_2O_3	0.00	0.00	0.02	0.00	0.00	0.00	0.03	0.00	0.00	0.01	0.01	0.00	0.00	0.00	0.00	0.00
Cr_2O_3	0.00	0.00	0.00	0.00	0.00	0.00	0.00	0.00	0.00	0.06	0.05	0.00	0.00	0.00	0.00	0.00
FeO*	4.40	7.48	8.19	8.57	5.30	5.56	8.35	8.81	8.87	3.88	7.30	7.54	8.00	8.36	4.50	8.72
MnO	0.03	0.08	0.13	0.14	0.06	0.09	0.12	0.11	0.11	0.08	0.09	0.12	0.15	0.15	0.05	0.14
MgO	54.10	51.31	51.13	51.12	53.04	53.33	50.98	50.57	51.15	54.78	51.93	52.05	51.52	50.65	53.93	49.58
CaO	0.01	0.05	0.03	0.03	0.01	0.04	0.01	0.17	0.01	0.01	0.08	0.02	0.03	0.02	0.00	0.01
Na_2O	0.00	0.00	0.00	0.00	0.01	0.00	0.00	0.00	0.00	0.00	0.01	0.00	0.00	0.00	0.01	0.03
K_2O	0.01	0.01	0.00	0.00	0.00	0.00	0.00	0.00	0.00	0.00	0.01	0.00	0.00	0.00	0.00	0.00
NiO	0.70	0.37	0.40	0.34	0.50	0.45	0.38	0.34	0.41	0.85	0.52	0.52	0.43	0.38	0.60	0.44
Total	101.52	100.54	101.60	102.44	100.08	101.02	100.90	101.75	101.41	101.33	101.60	102.41	102.55	101.01	101.69	99.02
Mg#	0.96	0.92	0.92	0.91	0.95	0.94	0.92	0.91	0.91	0.96	0.93	0.92	0.92	0.92	0.96	0.91

Abbreviations: Chr = chromitite, Dun = dunite, Har = harzburgite

Table 2-3. Selected microprobe analysis of olivine in chromitite, dunite and harzburgite from the northern Oman ophiolite. Mg# = $Mg/(Mg+Fe^{2+})$.

Table 2-4. Selected microprobe analysis of clinopyroxene in harzburgite from the northern Oman ophiolite.

Wadi	Hilti	Hilti	Hilti	Hilti	Hilti	Hilti	Hilti	Fizh	Fizh	Hilti
		Discor.				Concor.	Concor.	Discor.	Discor.	Discor.
Rock type	Dun.	Har.	Har.	Har.	Har.	Dun.	Har.	Dun.	Har.	Chr.
Remarks		proximal	proximal	proximal	ambient		proximal		proximal	imclusion
Texture		*0.5m*	*1.2 m*	*4.2 m*	*8.2 m*					Mas.
Sample	HD9	HD28-62	DH2	DH4	DH6	HC4-60	HC1-	FZD1	FZH1	HD3
SiO_2	55.76	54.99	54.85	54.21	54.03	54.58	54.42	55.50	55.12	55.19
TiO_2	0.06	0.05	0.00	0.03	0.05	0.10	0.04	0.08	0.03	0.06
Al_2O_3	1.11	1.77	2.13	2.03	2.41	1.67	1.68	1.04	1.01	0.99
Cr_2O_3	0.70	0.84	0.91	0.80	0.87	1.11	0.78	0.78	0.68	1.37
FeO*	1.58	1.85	2.10	2.24	1.87	1.63	1.86	1.66	1.71	1.01
MnO	0.05	0.06	0.05	0.05	0.02	0.06	0.10	0.10	0.05	0.06
MgO	17.54	17.44	17.53	18.90	17.39	17.02	17.63	18.53	18.53	20.70
CaO	24.23	24.17	24.05	22.16	24.02	25.23	24.21	22.27	22.43	20.61
Na_2O	0.31	0.13	0.13	0.07	0.02	0.22	0.19	0.80	0.81	0.40
K_2O	0.00	0.00	0.00	0.00	0.00	0.00	0.00	0.01	0.00	0.01
NiO	0.01	0.02	0.05	0.05	0.05	0.03	0.02	0.07	0.06	0.11
Total	101.36	101.31	101.81	100.54	100.72	101.64	100.93	100.83	100.43	100.51
Mg#	0.95	0.94	0.94	0.94	0.94	0.95	0.94	0.95	0.95	0.97

Abbreviations: Chr = chromitite, Dun = dunite, Har = harzburgite

Table 2-4. Selected microprobe analysis of clinopyroxene in chromitite, dunite and harzburgite from the northern Oman ophiolite. Mg# = $Mg/(Mg+Fe^{2+})$.

Table 2-5. Selected microprobe analysis of orthopyroxene inharzburgite from the northern Oman ophiolite.

Wadi	Hilti	Hilti	Hilti	Rajmi	Rajmi	Fizh
	Discor.	Concor.		Discor.	Concor.	Discor.
Rock type	Har.	Har.	Har.	Har.	Har.	Har.
Remarks	proximal	proximal	ambient	proximal	proximal	proximal
Texture						
Sample	HD28-68	HC4-60	DH17	WR3-9	KSH29	FZH
SiO_2	57.56	57.87	57.28	56.91	56.10	56.76
TiO_2	0.03	0.01	0.05	0.02	0.01	0.01
Al_2O_3	1.19	1.14	2.16	1.65	1.66	0.82
Cr_2O_3	0.54	0.44	0.61	0.47	0.51	0.21
FeO*	5.36	5.44	5.23	5.70	5.65	6.12
MnO	0.12	0.15	0.07	0.10	0.13	0.18
MgO	34.20	34.40	33.24	35.12	34.45	35.60
CaO	1.35	1.01	2.45	0.53	0.49	0.33
Na_2O	0.00	0.00	0.04	0.02	0.00	0.00
K_2O	0.01	0.00	0.01	0.00	0.00	0.00
NiO	0.10	0.05	0.10	0.09	0.09	0.09
Total	100.45	100.51	101.23	100.61	99.10	100.11
Mg#	0.92	0.92	0.92	0.92	0.92	0.91

Table 2-5. Selected microprobe analysis of orthopyroxene in harzburgite surrounding chromitites of the northern Oman ophiolite. Mg# = $Mg/(Mg+Fe^{2+})$.

Location	Wadi Hilti						Wadi Fizh	
	Discordant				Concordant		Discordant	
Rock type	Dun.	Har.	Har.	Har.	Dun.	Har.	Dun.	Har.
Remarks	envelope	proximal	proximal	ambient	envelope	proximal	envelope	proximal
Sample	HD14	DH2	DH4	DH6	SD3	SCH1	FZD1	FZH
Nb	0.045	0.084	0.072	0.067	0.030	0.070	0.080	0.085
La	0.027	0.008	-	-	0.067	0.113	0.106	0.023
Ce	0.079	0.016	-	-	0.125	0.383	0.366	0.100
Sr	0.731	0.559	0.079	0.064	3.499	0.881	13.699	2.344
Pr	0.009	-	-	-	0.016	0.050	0.072	0.024
Nd	0.064	-	-	0.001	0.090	0.223	0.437	0.160
Zr	1.129	0.085	0.074	0.058	0.788	0.769	1.611	0.771
Sm	0.040	-	-	-	0.056	0.091	0.231	0.093
Eu	0.019	-	-	-	0.023	0.035	0.073	0.043
Gd	0.115	-	-	-	0.099	0.197	0.307	0.183
Ti	432.552	170.657	157.015	296.275	483.704	368.065	391.391	385.302
Tb	0.032	0.006	0.007	0.012	0.030	0.049	0.062	0.044
Dy	0.385	-	-	-	0.345	0.457	0.511	0.390
Y	2.707	0.983	0.928	1.560	2.406	2.907	3.126	2.316
Ho	0.097	0.036	0.034	0.060	0.080	0.114	0.118	0.111
Er	0.352	0.157	0.159	0.219	0.284	0.406	0.401	0.266
Tm	0.050	0.033	0.030	0.039	0.045	0.061	0.055	0.042
Yb	0.296	0.262	0.256	0.268	0.246	0.471	0.443	0.311
Lu	0.043	0.047	0.043	0.041	0.033	0.064	0.068	0.043

Table 2-6. Selected trace element compositions of clinopyroxene in dunite and harzburgite surrounding chromitites of the northern Oman ophiolite.

- : not detected.

Chapter 3: Platinum-group element and mineral characteristics of chromitite xenoliths from the Takashima alkali basalt, Southwest Japan: Implications for the origin of ophiolitic chromitites

3.1: Abstract

Ophiolites provide us with an excellent opportunity for understanding the various processes in the crust-mantle section of oceanic lithosphere. However, their tectonic setting of formation is unclear. Chromitites, one of constituent rocks of ophiolites, are frequently used as a tracer of sub-arc mantle magmatism. Chromitite xenoliths from the Takashima alkali basalt, Southwest Japan arc, derived from the current sub-arc mantle, are compared with ophiolitic chromitite to constrain the origins of chromitite and ophiolite.

The Takashima chromitite xenoliths show various textures, e.g., nodular, anti-nodular and layered varieties. The range of chromian spinel Cr# of the Takashima chromitite xenoliths and dunites is similar to that in arc-related plutonic rocks, indicating arc-related feature. Laurites, one of typical PGMs (= platinum-group minerals) in chromitite, were commonly found as minute (<5 μm diameter) solitary grains of euhedral shape in spinel. Laurite grains in the Takashima chromitites are similar in its chemical characteristics to those in ophiolitic chromitites. Co-bearing pentlandite as very fine (around 1μm diameter) grains are sometimes associated with primary silicate inclusions in chromian spinel. Silicate inclusions, showing a concentric distribution in spinal, are mainly composed of pyroxenes and olivine. The chondrite-normalized PGE (= platinum-group element) patterns of Takashima chromitites show slightly negative slopes from Ru to Pt, similar to some ophiolitic chromitites. The Takashima chromitites are quite similar in its PGE chemistry, spinel chemistry and textural variations to some of the discordant chromitites in the northern Oman ophiolite, indicating a possible sub-arc origin for the latter. Similarities in some ways between the Takashima chromitite and the Oman discordant chromitites strongly indicate that the Oman discordant chromitites were formed at a supra-subduction mantle setting before ophiolite obduction.

3.2: Introduction

Peridotite xenoliths furnish us with direct information on mantle or deep-seated materials and processes, especially those of specific tectonic settings. Xenolith-bearing basalts mostly erupted at continental rift zones or hotspots, and mantle materials from these settings are relatively easily avaiable (e.g., Nixon 1987). In contrast, sub-arc mantle materials are relatively difficult to appear on the surface as xenoliths (e.g., Nixon 1987). Chromitites, one of mantle rock types, have been rarely described as xenoliths in magmas, possibly reflecting this situation (e.g., Thayer 1970). Peridotite xenoliths captured by basic magmas that erupted on the Japan arcs represent sub-arc upper mantle materials beneath the Japan arc (e.g., Arai *et al*. 2007; Arai and Ishimaru 2008). Chromitite xenoliths were rarely described from alkaline basalt of Takashima, Southwest Japan arc (Arai and Abe 1994), which verifies the existence of chromitite in the sub-arc mantle.

Ophiolites gives us excellent opportunities for observing and understanding various processes in the lithosphere. However, their derivation is unclear, and their origin has been controversial. Chromitite is one of key rocks in the ophiolite, although its abundance is very low, to interpret the origin of ophiolite. Ophiolitic chromitites have been frequently interpreted as a sub-arc deep magmatic product (e.g., Arai and Yurimoto 1995; Uysal et al. 2005; Miura et al. 2014). In this chapter, I examine the Takashima sub-arc chromitite xenoliths in detail for texture, mineral chemistry and PGE (platinum-group elements) character, and make a comparison with a chromitite suite (discordant chromitites from Wadi Rajmi) from the northern Oman ophiolite. It will promote our understanding of processes of chromitite formation as well as of tectonic setting for the Oman ophiolite formation.

3.3: Geological background

The Takashima alkali basalt of 3.0 Ma in age (Nakamura et al. 1986) is well known as one of the numerous Cenozoic monogenetic alkali basalt volcanoes of the Southwest Japan arc (Fig. 3-1). It was erupted on the northern margin of the Kyushu island that faces the Sea of Japan, a back-arc basin for the Japan island arcs. The magmatism of the Takashima alkali basalt was caused by mantle diapirism which

was most active in the Miocene and opened the Sea of Japan (Iwamori 1991). Many ultramafic xenoliths are observed on basaltic beach boulders around the Takashima island (Kobayashi and Arai 1981; Arai et al. 2001). The Takashima xenolith suite is mainly composed of peridotites, pyroxenites, gabbros, basement granodiorites and granulites (Arai et al. 2001). The Takashima ultramafic xenoliths are devided into two distinct groups, I and II, in terms of chemical characteristics and textures in the sence of Frey and Prinz (1978) (Arai et al. 2000). Group I xenoliths are characterized by green Cr-rich clinopyroxene (e.g., Frey and Printz 1978), and comprise mantle, dunite, wehrlite and pyroxenites. Group II xenoliths, mainly pyroxenites, contain black Al-rich clinopyroxene (e.g., Frey and Printz 1978), and are younger than Group I rocks (Arai et al. 2001). They are mainly found from monogenetic volcanoes forming volcano clusters in southwestern Japan (Arai et al. 2000). Chromitite xenolith from Takashima is classified as Group I (Arai and Abe 1994).

Group I dunite and clinopyroxenite are predominate over other species of xenoliths from the Takashima both in number and in size (Arai et al. 2000). Mantle harzburgite has never been found from the Takashima alkali basalt. On the other hand, the Kurose alkali basalt, exposed 30km to the northeast of the Takashima, encloses xenoliths of mantle peridotites and other Group I rocks (Arai et al. 2000). The equilibrium temperature (Wood and Banno 1973) of the Takashima and Kurose ultramafic xenoliths ranges from 1000 to 1100 °C (Arai et al. 2000). Ultramafic rocks from both the suites of xenoliths are free of olivine-garnet and olivine-plagioclase assemblages, indicating their formation within the spinel lherzolite stability depth (~ 1.0 to 1.5 GPa) (Arai et al. 2001).

3.4: Petrography

The Takashima chromitites show various textures, i.e., massive, nodular, anti-nodular, layered and schlieren) (Arai and Abe 1994) (Fig. 3-2). They are classified into two types in terms of their texture (Arai and Abe 1994). One (Type 1) shows massive, layered and schlieren textures, associated with dunite or wehrlite (Figs. 3-2). The olivine nodules in spinel-rich part (anti-nodular) texture, although the shape is incomplete, are occasionally found in the chromitite seam (Fig. 3-2e). The other

(Type 2) shows a nodular texture (Fig. 3-2d). Chromian spinels in the two types of the Takashima chromitite show a dark brown color in thin section, suggesting their Cr-rich character (Fig. 3-3).

Chromian spinels in Type 1 chromitite are relatively fine and euhedral to subhedral in shape (Fig. 3-3a). Fine-scale foliation or layering is frequently observed in Type 1 chromitites (Fig. 3-3b). The matrix minerals are mainly olivine and clinopyroxene (Fig. 3-3a). The matrix is sometimes wherlitic. Some of rounded olivine grains are poikilitically enclosed by pyroxenes. Two massive chromitites composed of fine-grained spinels were analyzed for whole-rock PGE chemistry (Figs. 3-2a, c, 3a). Olivine nodules in the anti-nodular textured part (Fig. 3-2e) are polycrystalline (Figs. 3-3c, d), and individual grains are coarser than those in enclosing chromitite and spinel-rich dunites (Fig. 3-3d). Spinels in Type 1 chromitite contain globular silicate inclusions, showing a concentric distribution indicating a primary origin (Fig. 3-3e). Raman spectroscopy indicates that the globular inclusions are composed of clinopyroxene and minor amount of olivine. Hydrous minerals, such as pargasite and phlogopite, have not been found from spinel of the Takashima chromitites.

Euhedral to subhedral laurites are included as minute (up to 5μm) solitary grains in chromian spinel (Figs. 3-4a, b). Subhedral to anhedral pentlandite inclusions appear as a trail or as solitary grains in spinel, olivine or pyroxenes (Figs. 3-4c, d). Very fine (around 1μm) grained pentlandites sometimes associated with the primary globular inclusions in spinel (Figs. 3-4e, f).

Type 2 chromitite is characterized by chromian spinel-rich nodules in a pyroxenitic or wehrlitic matrix (Fig. 3-3f). Orthopyroxenes of secondary origin (Arai et al. 2006) exist in the matrix. This type of chromitite is free of layering or foliation. Spinel in Type 2 chromitites sometimes contains the primary globular silicate inclusions, showing a concentric distribution, such as in Type 1 chromitites. Type 2 chromitite is very similar in appearance to some ophiolitic nodular chromitite (e.g., Thayer 1964; Nicolas 1989). Base-metal sulfides are also included by spinel in the same manner as in Type 1 chromitites (Fig. 3-4).

Dunite xenoliths from the Takashima alkali basalt are characterized by coarse-

grained and show mosaic-equigranular textures. Olivines in dunite sometimes exhibit kink band and wavy extinction. Spinels show reddish brown to black colors in thin section, suggesting their Cr-rich character. Sulfides (mainly pentlandite) appear as solitary or secondary inclusions in some olivine grains.

3.5: Analytical condition

Sulfide mineral chemistry

Sulfide minerals were also analyzed by a JEOL wave-length dispersive electron microprobe (JXA8800R) at Kanazawa University. Analytical conditions were 15 kV accelerating voltage, 20 nA probe current, and <1 μm probe diameter. Pure metals and sulfides were used as standards for the elements of Os, Ir, Ru, Rh, Pt, Pd, Fe, Ni, Co, Cu, Zn and Cr, whereas pentlandite for S. Representative analyses are listed in Tables 3-4 & -5.

Whole-rock PGE chemistry

Two fine-grained Takashima chromitite samples (Type 1) (Figs. 3-2, 3a) were analyzed for all PGEs (=Os, Ir, Ru, Rh, Pt, Pd) and Au (Table 3-3). Chromitite xenolith samples of enough amounts for bulk analysis were available from only two samples because of rarely occurrence of chromitite xenoliths from the alkali basalt. One (TKC-1) contains laurite grains (Fig. 3-4a), and the other (TKS-Cr-1) is apparently free of PGM in thin section. The other chromitite sample (WR3-3) from the discordant chromitite pod along Wadi Rajmi, northern Oman ophiolite, and two spinel-rich dunite xenolith samples (KR241 and KRC-1) from the Kurose alkali basalt were also analyzed for comparison. The Kurose samples are apparently free of PGM in thin section. The whole-rock PGE contents in samples were determined by using ICP-MS after the Ni-sulfide fire assay collection at the Genalysis Laboratory Services, Australia. The detection limits are 2ppb for Os, Ir, Ru, Pt and Pd, 1ppb for Rh. Au is below detection limits in all analysed samples.

3.6: Mineral chemistry

Spinels from the Takashima chromitite show relatively high Cr#s, 0.6 to 0.8, and low

TiO_2 contents, 0.16 to 0.63 wt% (Fig. 3-5; Table 3-1) (Arai and Abe 1994). Spinels in dunite xenoliths also show high Cr#s, 0.67 to 0.80, but slightly higher TiO_2 contents, up to 0.43wt%, than those from the chromitites. The Kurose harzburgite spinel shows a relatively low range of Cr#, 0.25 to 0.5 (Fig. 3-5) in comparison. Spinels in the Kurose chromitite are characterized by low Cr#s around 0.35, and high TiO_2 contents, up to around 0.40wt%.

Laurites (ideal formula of RuS_2) show Os-rich varieties, in which the Ru / (Ru+Os+Ir) atomic ratio ranges from 0.66 to 0.85 (Fig. 3-6). The Os content in laurites varies from about 8 up to 19 wt%, with an average of 15wt% (n= 6 analyses) (Table 3-4). The range of Ir content is from 6 to 9 wt%, with an average of 7 wt% (Table 3-4). Erlichmanite (ideal formula of OsS_2), one of end members of laurite-erlichmanite series, have not been found. The relatively high Cr content in some PGM grains was due to a fluorescence effect from host chromian spinel in microprobe analysis because of their small size (< 5um) (Fig. 3-4). Therefore, their compositions were corrected by subtraction of the expected spinel compositions. The Ni/ (Ni+Fe) atomic ratio of pentlandites in chromitites and dunites varies from 0.13 to 0.48 (Fig. 3-6d). Pentlandites are characterized by high Ni contents in chromitites than in dunites. Fine-grained pentlandite associated with silicate inclusions in spinel of Type 2 chromitite (Figs. 3-4e, f) contains 0.2 wt% Co (Table 3-5).

3.7: Platinum-group element chemistry

The PGM-bearing chromitite (TKC-1) is high in total PGE (209 ppb) relative to the PGM-free one (TKS-Cr-1) (100 ppb) (Fig. 3-6a) from the Takashima alkali basalt (Table 3-3). Two analyzed chromitite samples of the Takashima are similar to each other in their respective PGE patterns (Fig. 3-6b). Two samples of the Takashima chromitites are distinctly enriched in Ir subgroup PGE (IPGE: Os, Ir, Ru) in preference to Pd subgroup PGE (PPGE: Rh, Pt, Pd) (Fig. 3-6b). The chondrite-normalized (CN) PGE patterns of the Takashima chromitites are characterized by negative slopes from Ru to Pt (Ru/Pt=22.3 and 7.5), positive slopes from Pt to Pd, and low Pd/Ir ratios, 0.08 to 0.25 (Fig. 3-6b; Table 3-3). The Takashima chromitites are intermediate in their PGE patterns between the mantle discordant chromitites and

the MTZ chromitites from the northern Oman ophiolite (Ahmed and Arai 2002) (Fig. 3-6b). On the other hand, two samples of the Kurose spinel-rich dunite are characterized by low total PGE contents (38 to 43 ppb), low Ru/Pt ratios (2.50 to 4.33) and relatively high Pd/Ir ratios (0.83 to 2.17) (Fig. 3-6b; Table 3-3). The analyzd ophiolitic chromitite sample from the northern Oman ophiolite is enclosed in the reported range for the Oman ophiolite (Ahmed and Arai 2002) (Fig. 3-6b).

3.8: Discussion

3.8.1: *Origin of the Takashima chromitites*

The appearance of chromitite xenoliths from the Takashima alkali basalt clearly indicates that chromitites are present beneath the Southwest Japan arc (Arai and Abe, 1994) (Fig. 3-7a). Spinels in the Takashima chromitites and dunites are characterized by high Cr#s and low Ti contents, indicating that the Takashima chromitites and associated dunites were formed by arc-related magmatism, especially that of high-Mg andesites and boninites (e.g., Arai 1994; Arai et al. 2011) (Fig. 3-5). Arc-related features in the Takashima chromitites and dunites are consistent with the Sr-Nd-Os isotopic characteristics (Senda et al. 2007) that indicate the sub-arc environment.

In addition, the textural variations, e.g., nodular and anti-nodular textures, of the Takashima chromitites (Fig. 3-2) are also similar to those of ophiolitic chromitites (e.g., Thayer 1964; Arai and Abe 1994). The Takashima chromitite is also very similar in PGE characteristics to some ophiolitic chromitites (Fig. 3-6). The latter commonly contain 100 to 500 ppb of PGE and have moderate ratios of low Pd/Ir (0.8 to 0.1) (e.g., Leblanc 1991). The PGE contents of chromitites tend to increase with increasing Cr# of spinel (degree of partial melting) (e.g., Economou 1986). Their spinel Cr#s and total PGE concentrations of the Takashima chromitites are enclosed in the range of mantle chromitites from the northern Oman ophiolite (Ahmed and Arai 2002) (Fig. 3-6a). In contrast, those of the Kurose spinel-rich dunites are quite low concentrations of total PGE, and slightly close to the range of the Oman MTZ chromitite (Fig. 3-6a). This possibly indicates that the involved magma in the formation of the Kurose spinel-rich dunite was formed low degree of partial melting. The CN PGE patterns of the Takashima chromitites show slightly negative slopes

from Ru to Pt (Fig. 3-6b), which are again within the range for some of ophiolitic chromitites (*e.g.,* Zhou et al. 1998; Ahmed and Arai 2002; Uysal et al. 2005). Occurrence of laurite, one of the most common PGM in ophiolitic chromitites (e.g., Ahmed and Arai 2002), is consistent with the positive Ru anomaly observed in the PGE patterns of the Takashima chromitites (Fig. 3-6b). Laurite grains from the Takashima chromitites are plotted in the compositional range of laurites from the Oman chromitite (Ahmed and Arai 2003) (Fig. 3-6c). Here, it is important that the characteristics of the Takashima chromitites, in spinel chemistry, textural variations and PGE chemistry, are analogous to some of ophiolitic chromitites. This similarity implies that the Takashima chromitites are similar in the character of magmatic formation process to the ophiolitic chromitites.

The Japan arc has been on an active margin of the eastern Eurasian plate since the subduction initiation of the Pacific plate at around 520 Ma (Isozaki et al. 2011), although the current island arc setting has started at 20 Ma by spreading of the Sea of Japan backarc basin (Iwamori 1991) (Fig. 3-7a). Some arc-related characteristics of the Takashima chromitites and peridotites (e.g., Arai et al. 2001; Senda et al. 2007) had been obtained sometime before the eruption of the host Takashima alkali basalt (3.0 Ma, Nakamura et al. 1986), however, no age data has been obtained for the Takashima Group I xenoliths. Paleomagnetic and geochronological studies of volcanic rocks in the Southwest Japan indicate that the clockwise rotation of southwest Japan arc until 15 Ma was caused by the spreading of the Sea of Japan (Otofuji et al., 1991). Then, a young and hot oceanic lithosphere of the Philippine Sea plate has been subducted beneath the southwest Japan (Tatsumi and Maruyama 1989). The high-Mg andesitic magmatisms in the Southwest Japan were probably caused by the initiation of subduction of such a young and hot slab. Some high-Mg andesites in Southwest Japan consistently are younger than the age of subduction of the Philippine Sea plate at around 15 Ma (Tatsumi et al., 2001). More recently, high-Mg andesites, associated with basalts, of 8-6 Ma in age (Mashima 2009) erupted in the northwest Kyusyu island near Takashima, Southwest Japan arc.

3.8.2: *Comparison with discordant chromitites from the northern Oman ophiolite*

As shown in Chapter 2, spinels in the Oman discordant chromitites are also characterized by high-Cr#s (>0.7) and low TiO_2 contents (<0.1), indicating a sub-arc mantle origin (Fig. 2-11) (e.g., Arai *et al.* 2011). The Takashima chromitites are notably similar to chromitites from discordant pods from the northern Oman ophiolite. The Wadi Rajmi area has been well known for the abundance of various chromitite pods (Nicolas 1989; Augé 1987; Rollinson 2008) (Fig. 2-3b). The Takashima chromitites are strikingly analogous in some ways to a suite of discordant chromitites from Wadi Rajmi (Fig. 2-5), northern Oman, as described in Chapter 2 (Table 3-6).

The Takashima chromitite xenoliths are similar in their textural variation to the Rajmi discordant chromitite pod (Figs. 2-5, 3-2). In addition, the Rajmi chromitite pods and dunite envelopes show a compositional affinity to arc-related plutonic rocks as well as Takashima chromitite (Fig. 3-5). It is noteworthy that the spinel chemistry is similar between various textured chromitites from the Rajmi discordant pod examined (Fig. 3-5). The Cr#s of the surrounding harzburgite spinels are relatively high, 0.54 to 0.67 (Figs. 3-5b, c). One sample (WR3-3) of massive chromitites, showing a similar texture with the Takashima Type 1 chromitite analyzed for bulk PGE, was analyzed for comparison (Fig. 3-2f; Table 3-3). The PGE patterns of the Rajmi and Takashima chromitites also similar in some characteristics to each other (Fig. 3-6). Euhedral to subhedral laurite grains were also found as a solitary grain in spinel or as a phase associated with globular silicate inclusion in spinel from the Rajmi chromitites (Figs. 3-4g, h). Their appearance in the Rajmi discordant chromitites is also consistent with the positive Ru anomaly observed in the CN PGE pattern (Fig. 3-6b). Laurites from the Rajmi chromitites also show Os-rich variaties similar to that from the Takashima chromitites (Fig. 3-6c).

The Takashima chromitites are, however, different from typical discordant chromitites such as the Rajmi one from the Oman ophiolite. It is notable that harzburgite xenoliths have not been found from the Takashima alkali basalt (Arai et al. 2000, 2001). On the other hand, ordinary ophiolitic chromitite with dunite envelope are commonly found in the mantle harzburgites (*e.g.,* Arai 1997) (Fig. 2-5).

Beneath the Takashima island, chromitites probably occur within a thick dunite layer (Arai *et al*. 2001) (Fig. 3-7a). This is equivalent to a cumulus mantle (Takahashi 1978), mainly composed of dunite, wehrlite and pyroxenites. It is possibly equivalent to the MTZ of ophiolites, which comprises mainly dunite and wehrlite (e.g., Nicolas 1989; Arai and Abe 1994). Some thick MTZ in the northern Oman ophiolite is completely free of harzburgites (Negishi *et al*. 2013). The Takashima chromitites possibly occur in a thick Moho transition zone beneath Takashima, Southwest Japan arc (Arai *et al*. 2001) (Fig. 3-7a).

The difference in mineral species composing the primary inclusions in chromian spinel is also noteworthy. The mineral assemblage in inclusion is pyroxenes ± olivine for the Takashima chromitite and pyroxenes + pargasite + Na-phlogopite for the Rajmi chromitite. Hydrous minerals, e.g., pargasite and phlogopite, are typically found as primary inclusions in spinel from chromitites (*e.g.,* Arai and Matsukage 1998; Ahmed and Arai 2002; Borisova *et al*. 2012). These hydrous minerals can be stable in the condition shown by the Takashima xenoliths, 1000 to 1100°C and around 1.0 to 1.5 GPa (Frost 2006). The absence of hydrous minerals probably resulted from a low-water content in magma involved in formation of the Takashima chromitite. Some of podiform chromitites are free from hydrous mineral inclusion in spinel (*e.g.,* Arai and Yurimoto 1994).

In the Takashima chromitites, laurite grains are enclosed by chromian spinel as only solitary grains (Figs. 3-4a, b). On the other hand, the laurite grain is sometimes associated with silicate inclusion in spinel from the Rajmi discordant chromitite (Fig. 3-4h), as commonly observed in some ophiolitic chromitites (Garuti et al., 1999; Ahmed and Arai 2003). Instead, pentlandite is associated with silicate inclusion in spinel from the Takashima chromitites (Figs. 3-4e, f). Pentlandite and other sulfides inclusions are absent in spinel from the Rajmi chromitites. This difference in appearance of base-matal sulfides possibly results from the difference in temperature and/or sulfur fugacity during the chromitite formation. The PGMs, e.g., laurite, in spinel from chromitites, are considered as typically primary phases precipitated from the melt involved in chromitite formation (Garuti et al., 1999; Ahmed and Arai 2003) because the PGMs and chromian spinel can be liquidus phases (Andrews and Brenan

2002). Laurite is crystallized at high temperatures, around 1200 to 1300 °C, and a relatively low sulfur fugacity (Brenan and Andrews 2001). The Rajmi chromitites most probably formed at a high temperature, and possibly a low sulfur fugacity, relative to the Takashima chromitites. The existence of pentlandite in spinel and olivine from the Takashima chromitites and dunites possibly suggests a sulfur fugacity higher than that for the Rajmi chromitites. As pentlandite can be stable below around 865°C (Sugaki and Kitakaze 1998), the sulfides were entrapped by spinel as sulfide melt (e.g., Fig. 3-4c). Pentlandite and other base-metal sulfide phases were crystallized at a later low-temperature stage. The pentlandite showing a trail is possibly of metasomatic origin from melt (alkali basalt) involved in formation of Group II rocks.

The Rajmi and other Oman discordant chromitite pods show their arc-related feature in some ways (Chapter 2) (Figs. 2-5, 3-5, 6). Such arc-related features of the Oma discordant chromitites and the similarity to the Takashima sub-arc chromitite xenoliths strongly indicate that they were formed by arc-related magmatism at a young sub-arc mantle (Fig. 3-7b). Some ophiolitic chromitites, showing similar characteristics with the Takashima chromitites, probably are of sub-arc origin. The Takashima sub-arc chromitites indicate a genesis of the ophiolitic chromitites and a tectonic setting for the Oman ophiolite formation.

3.9: Figures and Tables

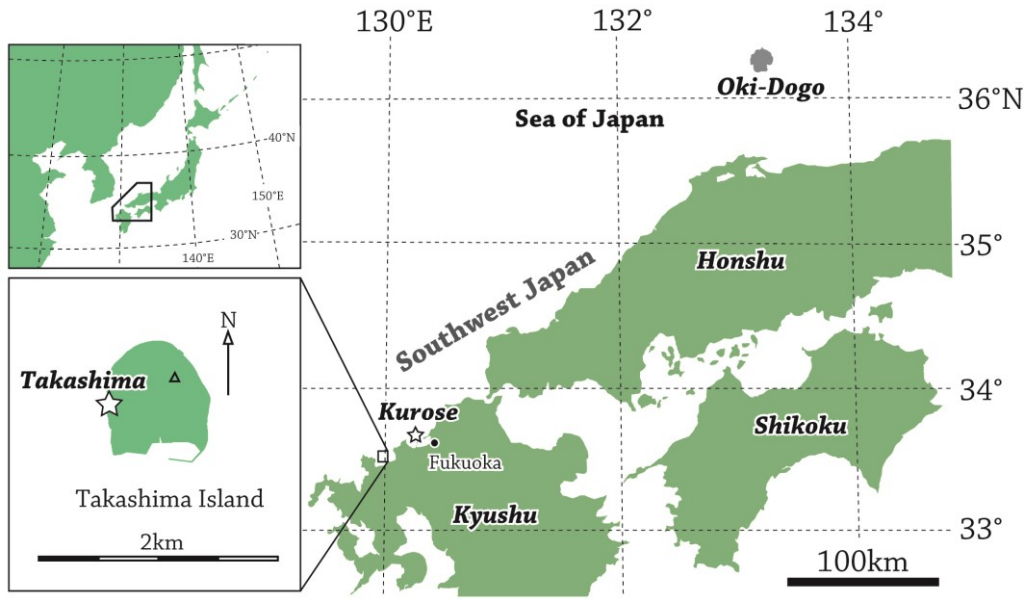

Figure 3-1. Locality maps of the Takashima and Kurose alkali basalts. Modified from Arai et al. (2001). Open star indicates the sampling locality.

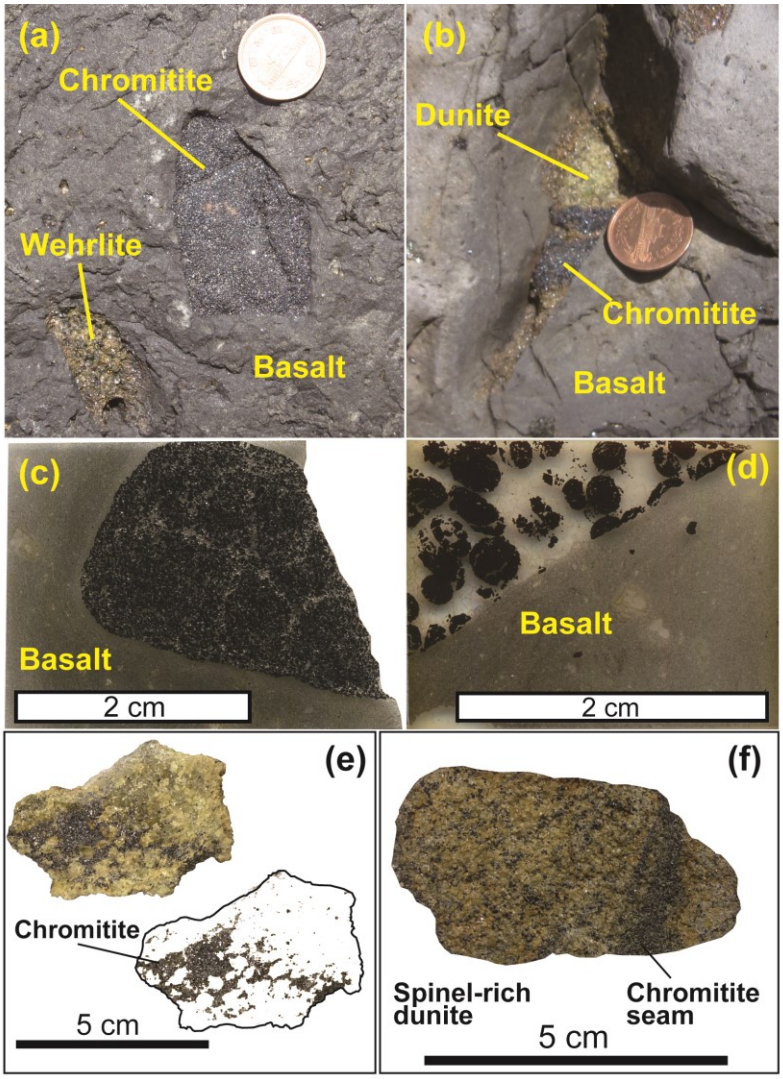

Figure 3-2. Appearances of chromitite xenoliths from the Takashima alkali basalt. (a) Massive chromitite (Type 1) xenoliths in the alkali basalt. This sample was analyzed for whole-rock bulk chemistry (TKC-1). (b) Xenolith of dunite with chromitite layer (Type 1). (c) Scanned image of thin section of a massive fine-grained chromitite (Type 1; the same as panel (a)). (d) Scanned image of thin section of a nodular textured chromitite xenolith (Type 2). (e) Anti-nodular chromitite xenolith (Type 1). Black-colored part shows chromian spinel concentrations. (f) Chromitite seam (Type 1) in a spinel-rich dunite.

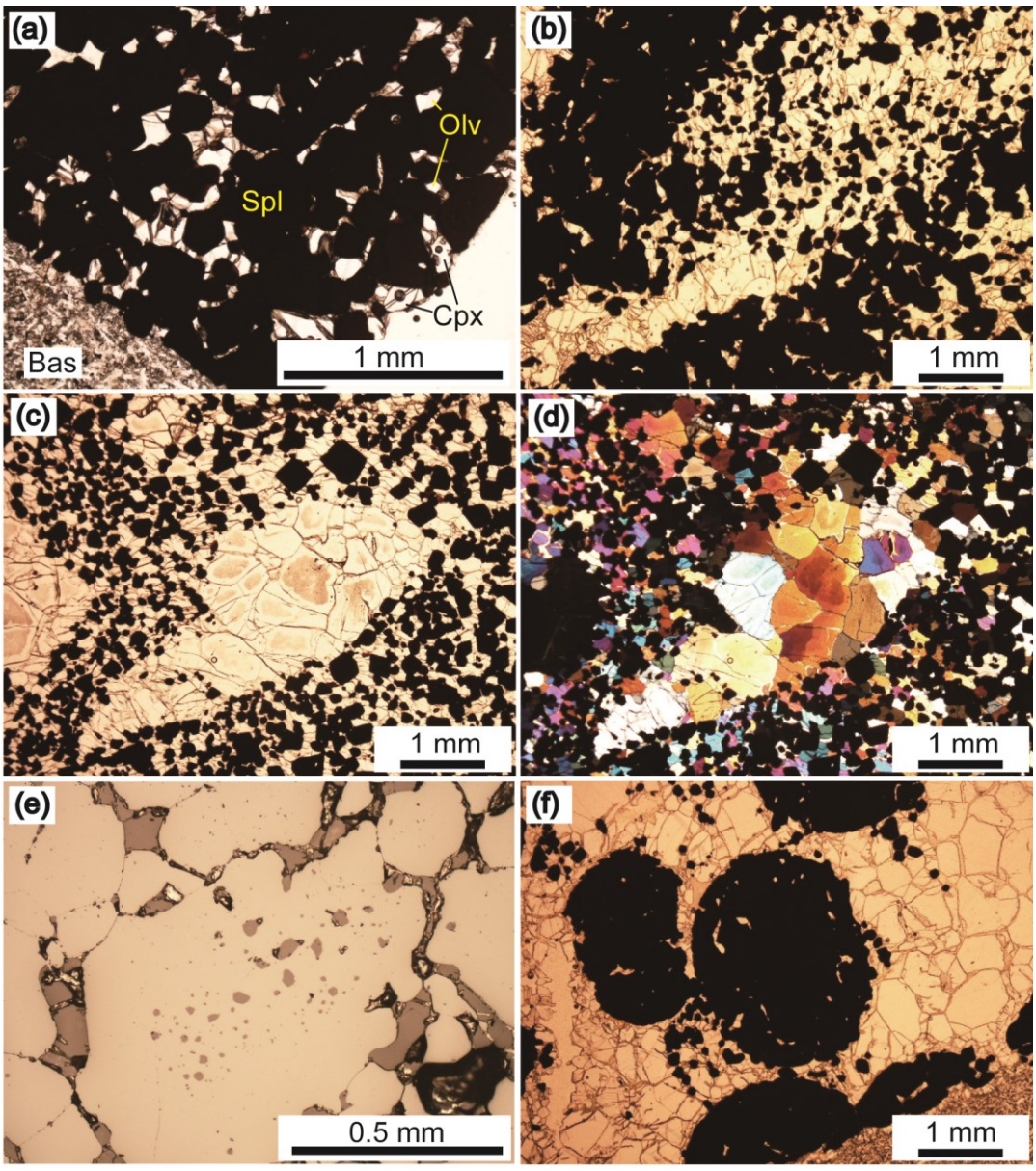

Figure 3-3. Photomicrographs of the Takashima chromitite xenoliths. Plane-polarized light (a-c, f), crosses-polarized light (d) and reflected light (e). Abbreviations; Spl, spinel: Olv, olivine: Cpx, clinopyroxene. (a) Fine-grained massive chromitite (Type 1) (TKC-1; the same as Fig. 3-2a) in the alkali basalt (Bas). (b) Finely layered texture in Type 1 chromitite. (c) Anti-nodular chromitite in Type 1 chromitite. (d) Crossed-polarized image of panel (c). Note that olivines composing nodule are coarser than those in surrounding spinel-rich part. (e) Spinel of the Type 1 chromitite, full of orbicular inclusions showing a concentric arrangement, which indicates a primary origin. (f) Nodular textured Type 2 chromitite xenolith.

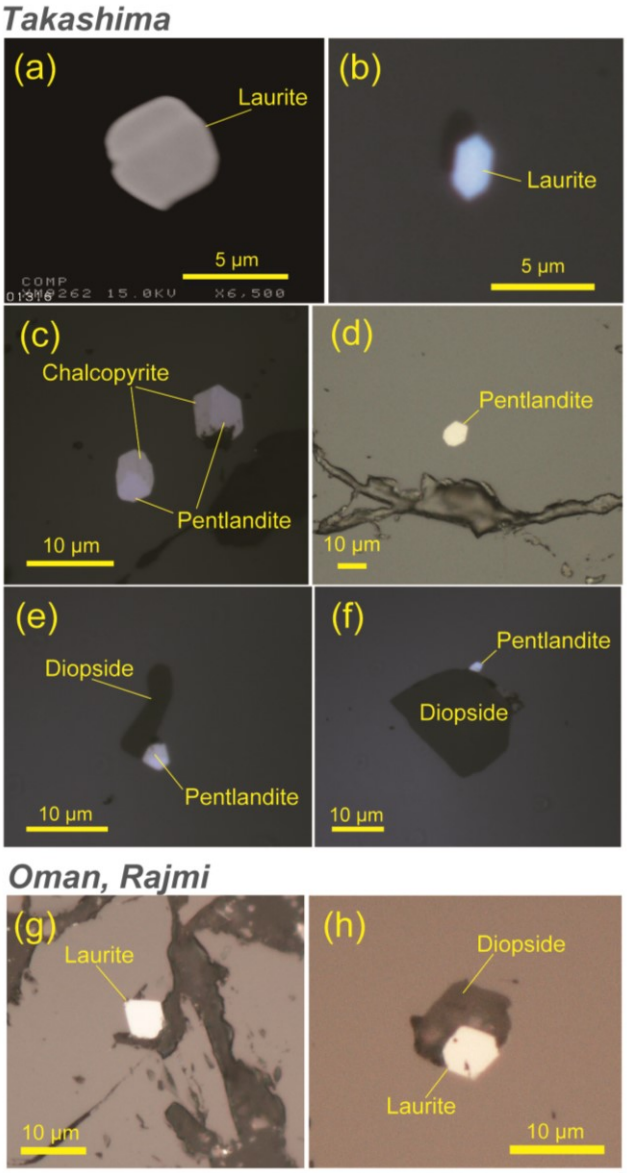

Figure 3-4. Backscattered electron micrographs and reflected-light images of sulfide inclusions in spinel from the Takashima and Rajmi chromitites. (a) Euhedral to subhedral laurite grain in chromian spinel from Type 1 chromitite. (b) Euhedral laurite inclusion in spinel in Type 2 chromitite. (c) Sulfide inclusions in spinel from Type 1 chromitite. (d) Pentlandite inclusion in spinel from Type 2 chromitite. (e) Pentlandite associated with a silicate mineral inclusion in spinel from Type 1 chromitite. (f) Pentlandite associated with a silicate inclusion in spinel from Type 2 chromitite. (g) Euhedral laurite grain in spinel from the Rajmi chromitite. (h) Laurite associated with a silicate mineral inclusion in spinel from the Rajmi chromitite. Note that pentlandite associating silicate inclusion as observed in spinel from the Takashima chromitite is free from the Rajmi chromitites.

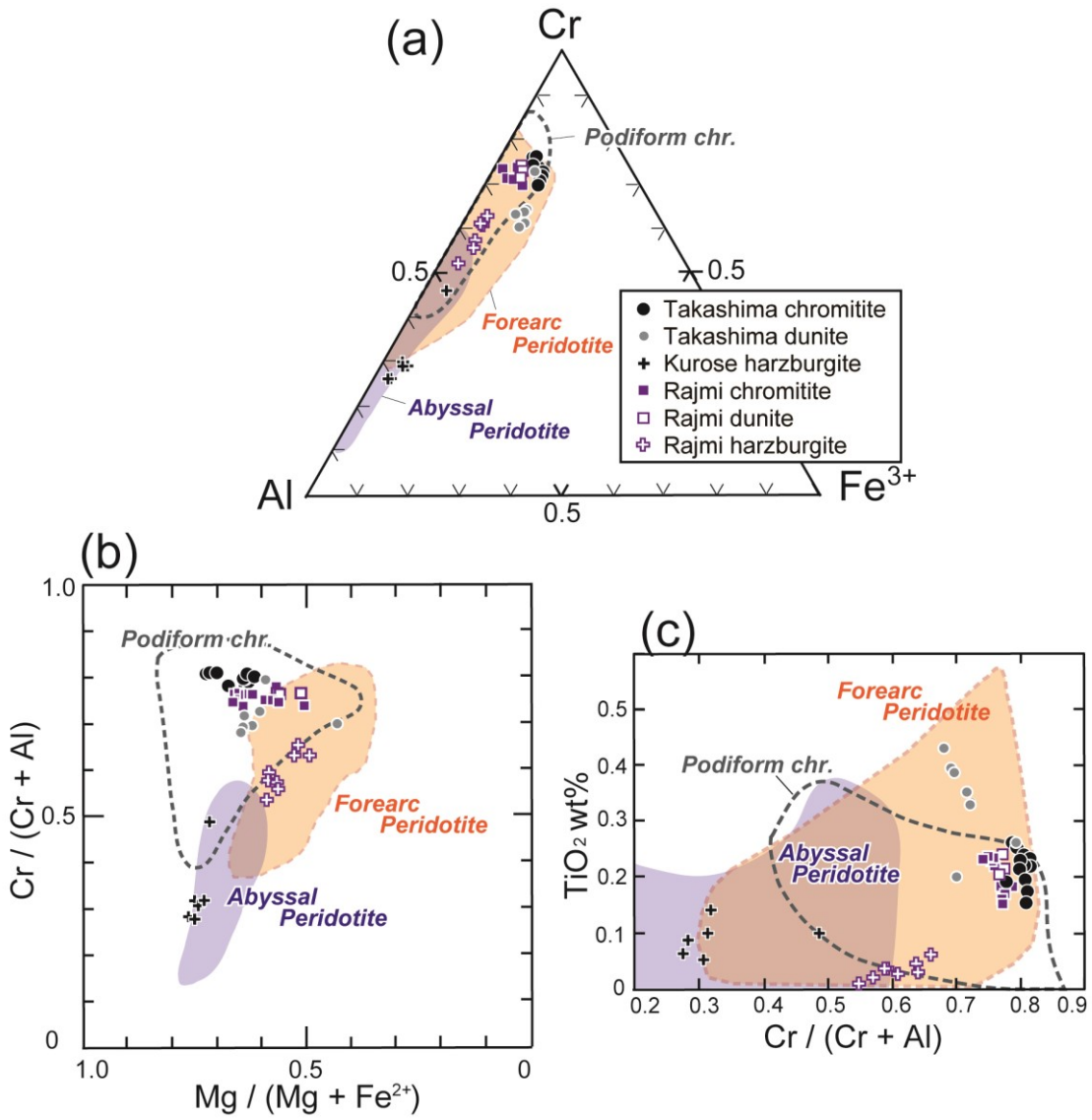

Figure 3-5. Chemical variations of chromian spinel in the Takashima and Kurose (left panels) xenoliths, and the Rajmi discordant chromitites (right panels). The Kurose harzburgites are plotted for comparison as the ambient mantle harzburgite. Abyssal peridotite fields are from Dick and Bullen (1984), Arai (1994) and Arai et al. (2011). Forearc peridotite fields are from Arai et al. (2011). Data of the Kurose harzburgites is from Hirai and Arai (unpublished data). (a) Trivalent cation ratios of chromian spinel in chromitites and associated peridotites. (b) Relationship between Cr# and Mg# of spinel from the two suites of chromitites and associated peridotites. (c) Relationship between TiO_2 content and Cr# of spinel in chromitites and associated peridotites. Note that compositional characteristics between the two textural types, Type 1 and Type 2, of chromitite are similar between the Takashima and Rajmi.

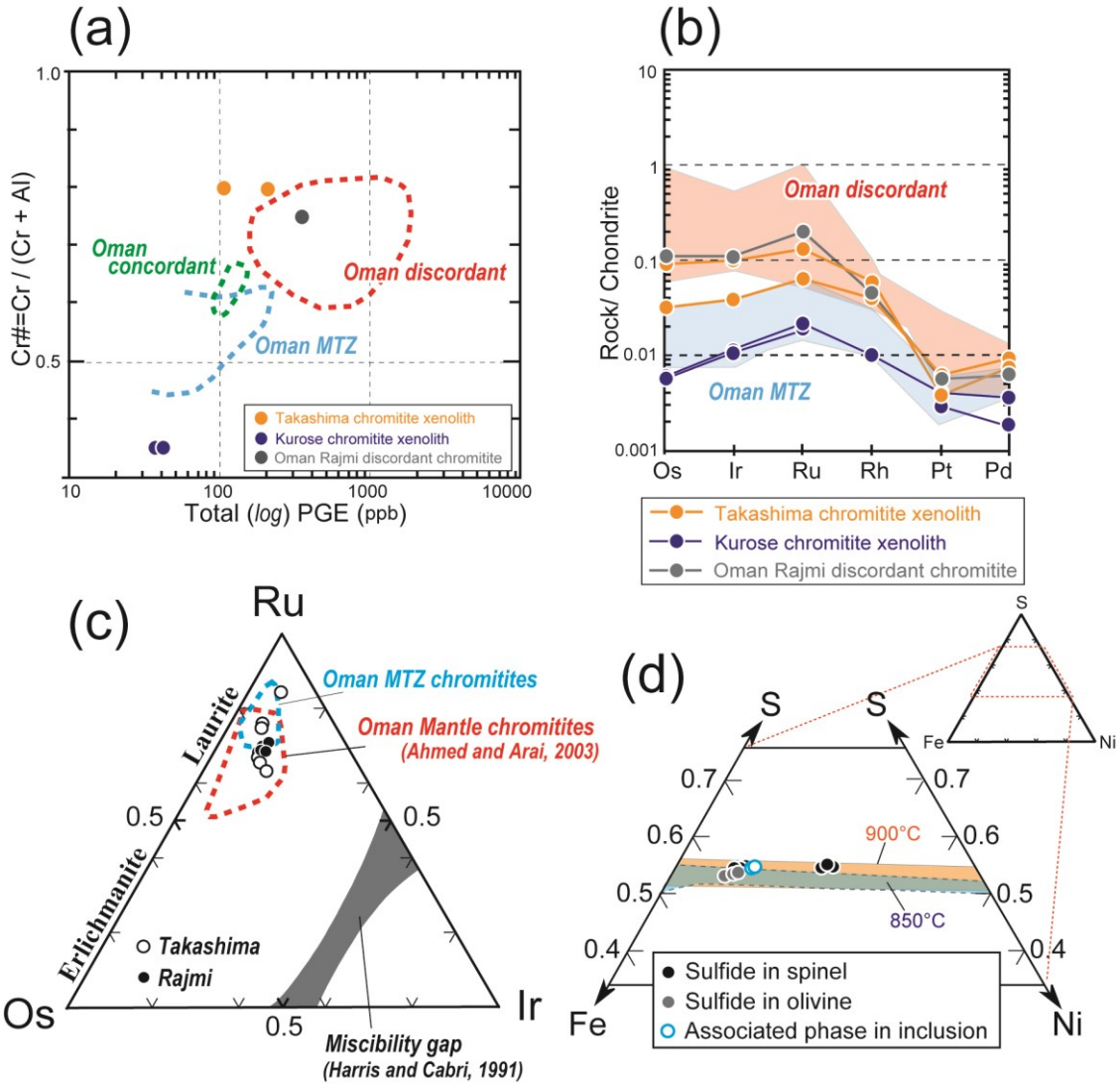

Figure 3-6. PGE characteristics of the Takashima and the Rajmi chromitites and the Kurose spinel-rich dunites. (a) Relationships between the spinel Cr# and the total PGE concentrations in the suites of chromitites and dunites. Oman MTZ and mantle chromitite variations are from Ahmed and Arai (2002). (c) Compositional variation of PGM in terms of Ru-Os-Ir in the laurite-erlichmanite series. (d) S-Fe-Ni atomic ratios of sulfides in the Takashima chromitites and dunites. Monosulfide solid solutions fields are from Ebel and Naldrett (1996, 1997).

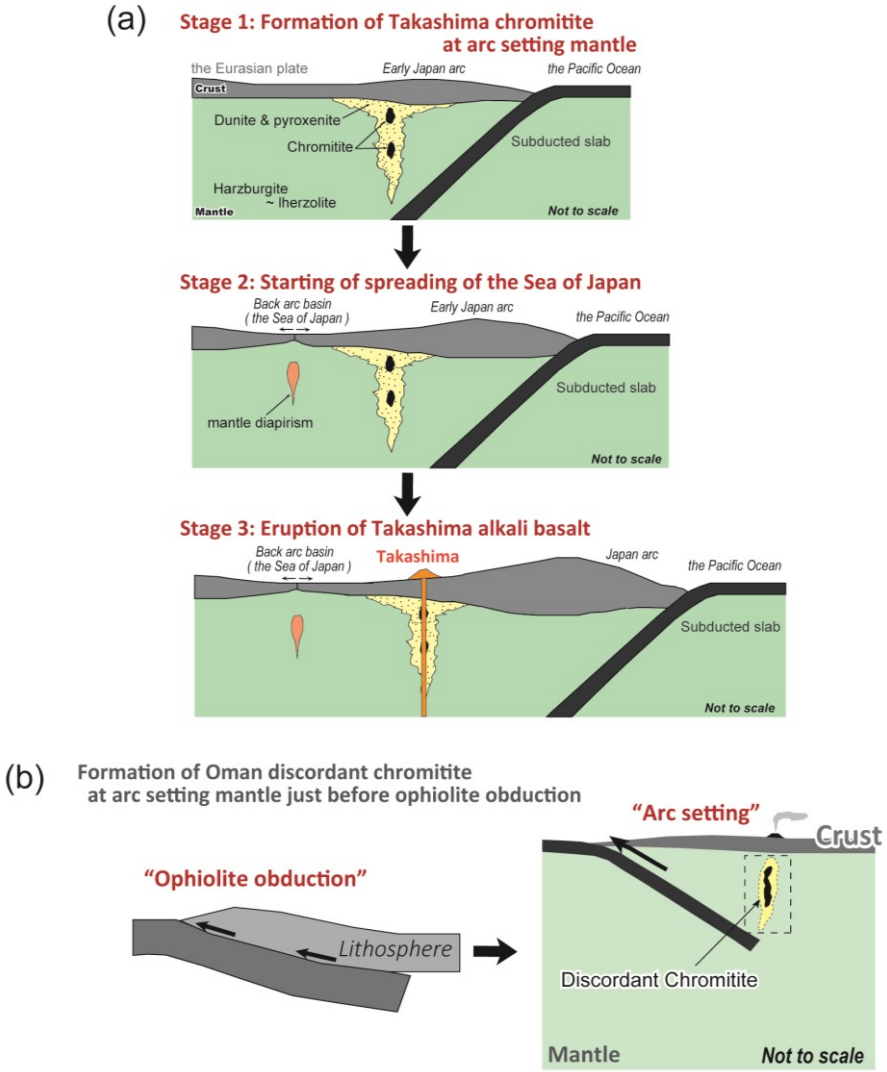

Figure 3-7. Petrologic models for sub-arc upper mantle containing discordant chromitites. (a) Takashima, southwest Japan arc. Note that chromitite exists in the thick MTZ mainly composed of dunite-wehrlite-pyroxenites (Arai et al., 2000). The Takashima chromitites were formed at sub-arc mantle sometime before the eruption of the host alkali basalt (around 3.0 Ma, Nakamura et al., 1986). (b) The discordant chromitite formed in a supra-subduction zone mantle before ophiolite obduction in the Oman ophiolite (c.f., Miura et al., 2012).

	Takashima					Kurose				Wadi Rajmi, Oman						
	Chromitite			Dunite		Spl-rich dunite		Harzburgite		Chromitite			Dunite		Harzburgite	
	Type 1		Type 2													
Texture	Mas.	Ant.	Nod.							Ant. ~Ma	Ant.	Nod.				
Sample	TKC-1	TKS-Cr-1	TKS-35	TKD-1	TKD-1	KR241-m5	KR241-m6	KR13	KR379	WR3-3-6	WR3-3-1	RNC-5	RND-7	WR3-3-1	RNH-9	WR3-9-8
	33	12	26	18	13	46	47			9	16	35	37	20	50	27
wt%																
SiO_2	0.04	0.02	0.10	0.04	0.01	0.02	0.04	0.04	0.01	0.01	0.00	0.00	0.00	0.00	0.05	0.00
TiO_2	0.24	0.23	0.22	0.26	0.34	0.38	0.37	0.06	0.10	0.16	0.19	0.23	0.24	0.04	0.06	0.03
Al_2O_3	9.84	9.62	9.53	9.87	12.96	35.05	35.04	40.94	28.71	11.67	11.05	12.24	12.98	21.39	17.71	20.82
Cr_2O_3	61.12	57.08	56.36	56.28	50.40	31.12	31.56	26.96	40.28	57.59	59.33	54.43	56.39	46.54	50.27	47.54
FeO*	14.96	20.03	19.69	20.19	21.64	16.18	16.26	13.65	14.09	16.71	17.80	21.47	18.13	19.19	20.83	18.60
MnO	0.25	0.26	0.30	0.31	0.27	0.19	0.17	0.16	0.23	0.26	0.32	0.32	0.29	0.28	0.28	0.27
MgO	15.47	13.23	12.67	12.15	12.59	17.00	16.96	18.05	16.52	13.58	11.79	11.80	10.74	12.55	10.99	12.66
CaO	0	0.01	0.05	0.01	0.00	0.00	0.00	0.01	0.00	0.00	0.00	0.00	0.01	0.00	0.01	0.00
Na_2O	0	0.00	0.00	0.04	0.03	0.00	0.00	0.00	0.00	0.00	0.05	0.00	0.00	0.01	0.01	0.01
K_2O	0	0.00	0.00	0.00	0.00	0.00	0.00	0.00	0.00	0.01	0.00	0.00	0.00	0.00	0.00	0.00
NiO	0.13	0.14	0.14	0.10	0.14	0.20	0.23	0.16	0.65	0.12	0.07	0.09	0.08	0.07	0.06	0.08
Total	102.04	100.62	99.06	99.24	98.37	100.13	100.64	100.02	100.59	100.12	100.59	100.59	98.85	100.07	100.25	100.01
Mg#	0.722	0.634	0.619	0.593	0.609	0.721	0.717	0.747	0.722	0.647	0.568	0.565	0.523	0.579	0.520	0.586
Cr#	0.807	0.799	0.799	0.793	0.723	0.373	0.377	0.306	0.485	0.768	0.783	0.749	0.745	0.593	0.656	0.605
$Cr/(Cr+Al+Fe^{3+})$	0.761	0.730	0.735	0.734	0.652	0.353	0.357	0.297	0.469	0.732	0.764	0.696	0.737	0.571	0.632	0.584
$Al/(Cr+Al+Fe^{3+})$	0.182	0.183	0.185	0.192	0.250	0.593	0.591	0.671	0.498	0.221	0.212	0.233	0.253	0.391	0.332	0.381
$Fe^{3+}/(Cr+Al+Fe^{3+})$	0.057	0.087	0.080	0.074	0.099	0.053	0.052	0.032	0.034	0.047	0.024	0.071	0.010	0.038	0.036	0.034

Abbreviations; Mas = massive, Ant = anti-nodular, Nod = nodular.
FeO* and Fe*, total iron as FeO and Fe, respectively.

Table 3-1. Selected microprobe analysis of spinel in the Takashima and Rajmi chromitites, dunite and harzburgite, and the Kurose spinel-rich dunite and harzburgite.

	Olivine					Cpx		Opx	
	Takashima				Kurose	Takashima		Takashima	Kurose
	Chromitite			Dunite	Harzburgite	Chromitite		Chromitite	Harzburgit
	Type 1		Type 2			Type 1			
Sample	TKC1-1	TKS-Cr-1	TKS-35-3	TKD-1	KR38	TKC-1-1	TKS-Cr-1	TKS-Cr-1	KR38
	40	8	25	20		30	18	7	
wt%									
SiO2	42.00	42.24	42.09	41.45	40.66	55.50	56.18	58.95	56.81
TiO2	0.00	0.00	0.00	0.00	0.01	0.08	0.06	0.04	0.05
Al2O3	0.00	0.00	0.01	0.02	0.01	1.04	0.92	0.64	2.36
Cr2O3	0.18	0.10	0.00	0.24	0.03	0.78	0.57	0.40	0.58
FeO	6.07	8.02	8.14	9.20	8.92	1.66	2.52	4.86	5.28
MnO	0.09	0.13	0.06	0.14	0.07	0.10	0.07	0.16	0.15
MgO	53.45	51.47	52.13	50.33	49.77	18.53	18.53	35.97	33.56
CaO	0.06	0.07	0.08	0.06	0.08	22.27	21.68	0.89	1.07
Na2O	0.01	0.00	0.00	0.00	0.00	0.80	0.77	0.07	0.02
K2O	0.01	0.00	0.00	0.00	0.00	0.01	0.00	0.00	0.00
NiO	0.53	0.40	0.38	0.31	0.44	0.07	0.04	0.06	0.08
Total	102.41	102.43	102.90	101.74	100.00	100.83	101.32	102.04	99.96
Mg#	0.940	0.920	0.919	0.907	0.909	0.952	0.929	0.929	0.919

FeO* and Fe*, total iron as FeO and Fe, respectively.

Table 3-2. Selected microprobe analysis of olivine in chromitite, dunite and harzburgite from the Takashima and Kurose alkali basalt, and the northern Oman ophiolite.

Location	Remarks	Texture	Sample	Os	Ir	Ru	Rh	Pt	Pd	Total	Pd/Ir	Ru/Pt
Takashima	Chromitite xenolith	Massive	TKC-1	47	53	89	12	4	4	209	0.08	22.25
Takashima	Chromitite xenolith	Massive	TKS-Cr-1	16	20	45	8	6	5	100	0.25	7.5
Kurose	Dunite xenolith	Spinel-rich	KR241	3	6	15	8	6	5	43	0.83	2.5
Kurose	Dunite xenolith	Spinel-rich	KRC-1	3	6	13	-	3	13	38	2.17	4.33
Rajmi	)iscordant pod in the Oman ophiolit	Massive	RA1	71	75	186	11	7	4	354	0.05	26.57

Table 3-3. Whole-rock analysis of bulk-rock platinum-group element compositions (ppb) in the Takashima and Rajmi chromitites and the Kurose spinel-rich dunitel.

Sample	Takashima					Rajmi		
	TK98 A2	TK98 A10	TKC1-1 A17	TKC1-4 A1	TKC1-4 A2	RNC2-1 702-01	RNC2-2 702-03	RNC2-3 702-04
wt%								
S	33.14	30.78	34.90	33.85	32.63	31.90	33.19	33.18
Os	18.72	18.41	7.77	15.14	15.36	16.53	17.71	15.68
Ir	8.64	9.24	6.23	6.18	6.62	9.32	9.24	9.65
Ru	31.62	28.38	42.23	37.55	36.34	31.05	33.64	33.56
Rh	2.15	1.90	3.31	3.11	3.06	2.01	2.19	2.10
Pt	0.35	0.65	0.55	0.00	0.00	0.00	0.01	0.17
Pd	1.64	1.47	2.14	2.02	1.99	1.57	1.84	1.78
Ni	0.04	0.06	0.49	0.02	0.07	0.27	0.28	0.09
Cu	0.01	0.00	0.26	0.00	0.00	0.00	0.00	0.00
Fe*	0.75	1.23	0.37	0.07	0.00	0.56	0.38	0.10
Fe	0.53	0.92	0.87	0.47	0.65	1.14	0.89	0.47
Cr	2.17	3.77	3.57	1.93	2.71	2.31	1.71	1.61
Total*	97.05	92.13	98.25	97.93	96.07	93.21	98.47	96.32
Atomic%								
S	67.023	66.463	65.820	66.412	65.995	66.935	66.379	67.153
Os	6.385	6.702	2.471	5.007	5.236	5.846	5.972	5.351
Ir	2.917	3.328	1.959	2.023	2.234	3.263	3.083	3.260
Ru	20.284	19.438	25.264	23.366	23.314	20.666	21.346	21.549
Rh	1.352	1.277	1.944	1.899	1.928	1.316	1.366	1.323
Pt	0.116	0.232	0.169	0.000	0.000	0.000	0.003	0.058
Pd	1.000	0.959	1.218	1.193	1.213	0.990	1.106	1.088
Ni	0.044	0.076	0.503	0.021	0.081	0.311	0.308	0.101
Cu	0.007	0.000	0.250	0.000	0.000	0.000	0.000	0.000
Fe*	0.871	1.525	0.401	0.079	0.000	0.675	0.436	0.116
Ru/(Ru+Os+Ir)	0.686	0.660	0.851	0.769	0.757	0.694	0.702	0.714

Fe*: Amount of Fe corrected for the chromian spinel matrix effect.

Table 3-4. Selected microprobe analyses of platinum-group minerals in spinels from the Takashima and Rajmi chromitites.

Sample	TKC1-3	TKS-Cr-1	TK98	TK98	TKD-1	TKD-1
	A7	A4	A3	A4	S7	S9
Rock type	Chromitite	Chromitite	Chromitite	Chromitite	Dunite	Dunite
Host mine	Spinel	Spinel	Sil. Inc.	Sil. Inc.	Olivine	Olivine
wt%						
Fe	24.59	34.20	41.49	40.76	45.54	49.92
Ni	23.79	24.58	14.66	13.96	12.56	7.87
Co	0.00	0.62	0.19	0.22	0.34	0.27
Cu	12.89	0.00	0.00	0.00	0.00	0.00
Zn	0.00	0.00	0.00	0.00	0.00	0.00
S	33.60	36.49	38.77	37.66	38.05	38.50
Si	0.00	0.06	0.03	0.07	0.04	0.00
Ti	0.00	0.02	0.02	0.00	0.00	0.03
Cr	3.04	2.74	2.09	2.00	0.03	2.87
Mn	0.04	0.04	0.00	0.00	0.02	0.00
Total	97.95	98.76	97.25	94.67	96.58	99.46
S	1.000	1.000	1.000	1.000	1.000	1.000
Fe	0.420	0.538	0.614	0.621	0.687	0.745
Ni	0.387	0.368	0.207	0.203	0.180	0.112
Co	0.000	0.009	0.003	0.003	0.005	0.004
Cu	0.194	0.000	0.000	0.000	0.000	0.000
Zn	0.000	0.000	0.000	0.000	0.000	0.000
Total	2.001	1.915	1.824	1.827	1.872	1.860
Ni/(Ni+Fe	0.479	0.406	0.252	0.246	0.208	0.130

Abbreviations; Sil. Inc. = silicate inclusion

Table 3-5. Selected microprobe analyses of other sulfide minerals in spinel from the Takashima chromitites. Sil. Inc. : silicate inclusion.

	Xenolithic chromitite	Ophiolitic chromitite	
	Takashima, Japan	**W. Rajmi, Oman**	**Ortaca, Turkey**
Textures	Mas + Dis + Nod + Ant + Lay	Mas + Dis + Nod + Ant + Lay	Mas + Dis + Nod + Ant + Lay
Composed minerals	Spl + Olv + Cpx	Spl + Olv	Spl + Olv
Primary inclusion in spinel	Cpx + Opx + Olv	Cpx + Opx + Amp + Phl	Cpx + Opx + Amp + Phl
Major element			
Cr# of spinel	0.78 - 0.81	0.75 - 0.80	0.73 - 0.81
TiO_2 wt% of spinel	0.14 - 0.25	0.10 - 0.22	0.04 - 0.24
PGE chemistry			
Range of total PGE (ppb)	100 - 209	354	63 - 266
Range of Pd/Ir ratio	0.08 - 0.25	0.05	0.23 - 1.73
Sulfides	Pen + Cha + Lau	Pen + Lau	Lau + Erl + Os-Ir alloy + Ni sulfide

Abbreviations: Textures Mas = massive, Dis = disseminated, Nod = nodular, Ant = anti-nodular, Lay = layered
Minerals Spl = spinel, Olv = olivine, Cpx = clinopyroxene, Opx = orthopyroxene
Pen = pentlandite, Cha = chalcopyrite, Lau = laurite, Erl = erlichmanite
Reference: Ortaca, Turkey (Uysal et al. 2005)

Table 3-6. A summary composition table between the Takashima and Rajmi chromitites.

Chapter 4: Comparison between low-pressure and ultrahigh-pressure chromitites from Luobusa ophiolite, Tibet, and Ray-Iz ophiolites, Polar Urals: Implications for mantle dynamics for chromitite formation

4.1: Abstract

Ultra-high pressure (=UHP) chromitites containing UHP minerals, such as diamond and moissanite, have been observed from the mantle section of Luobusa ophiolite, Tibet, and Ray-Iz ophiolite, Polar Urals. Some chromitites and surrounding peridotites from Luobusa and Ray-Iz ophiolites were compared with low-pressure (=LP) chromitites from the northern Oman ophiolite, to constrain peculiar characteristics of the UHP chromitite.

UHP chromitites from both the ophiolites are similar in some ways to each other. They are mostly concordant to the foliation of surrounding peridotite. Spinels show a high-Cr# and low-Ti character in both chromitites and surrounding dunite envelopes, indicating their arc-related feature. The UHP chromitites are similar in compositional characteristics of spinel to the discordant chromitites from the Oman ophiolite. Olivines in UHP chromitites are sometimes characterized by exceptionally high NiO contents (> 1 wt%), indicating long duration of cooling. Spinels in both UHP chromitites typically include numerous silicate exsolution lamellae. The UHP chromitites are divided into two types in terms of mineral species as inclusion in spinel. One is characterized by coesite lamella (Yamamoto et al., 2009) and Na amphibole primary inclusion in spinel. The other is characterized by the absence of primary amphibole inclusion. Coexistence of coesite and Na amphibole in the former spinel indicates their experience of relatively low-T (around 700 to 800 °C) and high-P (around 3 GPa) conditions. The former can be formed by UHP metamorphism in a subduction zone setting, because of stable condition of coesite and amphibole. Their similarity in characteristics of inclusion in spinel to chromitites of the Higashi-Akaishi ultramafic complex, which experienced high-P metamorphism, suggests that some of characteristics of the UHP chromitite can be formed by compression of low-P chromitites, such as deep recycling (Arai 2010, 2013).

4.2: Introduction

Ophiolitic chromitites, such as those in the Oman ophiolite, commonly show various lines of evidence for low-pressure (=LP) origin. However, some unusual minerals indicating ultrahigh-pressure and highly reduced condition, such as diamond, have been found from chromitites in some ophiolites such as the Luobusa ophiolite, Tibet (Robinson et al., 2004; Yang et al., 2007; Xu et al., 2009; Yamamoto et al., 2009) and the Ray-Iz ophiolite, Polar Urals (Yang et al., 2014). Origin of such ultrahigh-pressure (=UHP) chromitites is still very controversial, although many researchers have tackled this problem (e.g., Robinson et al., 2004; Ruskov et al., 2010; Arai 2010, 2013; Yang et al., 2014). Robinson et al. (2004) suggest that UHP minerals from the Luobusa chromitites are of xenocrystal origin. Lamellar coesite in chromian spinel from UHP chromitite from Luobusa, however, strongly indicates that the UHP chromitite has experienced some UHP condition, and negates the xenocrystal origin of UHP minerals (Yamamoto et al., 2009). Ruskov et al. (2010) and Yang et al. (2014) proposed a magmatic origin under UHP conditions and later modification under LP conditions by arc-related magma for the UHP chromitite. However, this hypothesis cannot well explain some characteristics of UHP chromitites, such as existence of dunite envelope and igneous textures similar to LP chromitites (Zhou et al., 1996; Yamamoto et al., 2009; Arai 2010; Xu et al., 2011). Arai (2010, 2013) proposed that UHP chromitites can be formed by deep recycling (UHP metamorphism) of LP magmatic chromitites via mantle convection flow. This hypothesis seems to explain many of features of UHP chromitites, however, geologic and petrographic data are not enough to validate this interpretation. In this Chapter, I describe detailed petrographic features of UHP chromitites from the Luobusa and the Ray-Iz ophiolites to constrain the origin of UHP chromitite.

4.3: Geological background

4.3.1: *Luobusa ophiolite, Tibet*

The Luobusa ophiolite is located at the east-end of the Indus-Yarlung-Zangbo suture zone, Tibet (Fig. 4-1). It has been interpreted to originate at a mid-ocean ridge setting between the Asia and the India continents, and to experience later modification at a

supra-subduction zone environment before obduction (e.g., Zhou et al., 1996, 2005; Yamamoto et al., 2007; Xu et al., 2011; Yamamoto et al., 2013). The Luobusa ophiolite is thus a slice of the Neo-Tethyan oceanic lithosphere, obducted in the Early Tertiary at around 65 Ma (e.g., Aitchison et al., 2002). The Luobusa ophiolite is mainly composed of clinopyroxene-bearing harzburgite, harzburgite, dunite, serpentine mélange and lower-crustal cumulates accompanied by minor basaltic pillow lavas and cherts (Zhou et al., 1996; Yamamoto et al., 2009) (Fig. 4-1). Minerals from spinel peridotite show an equilibrium pressure of around 1.5 GPa, and have no traces of UHP metamorphism (Huot et al., 2002; Hébert et al., 2003). Therefore, peridotites and chromitites in the Luobusa ophiolite were interpreted to have formed at relatively low-pressure condition (< 30 km), such as uppermost mantle (e.g., Zhou et al., 1996). In this study, chromitites and surrounding peridotites from the mantle sections in the western part (chromitite, LT55 and LT69; dunite, LT52 and LT40; harzburgite, LT39 and LT38), the central part (LA326) and the eastern part (Cr-11 chromitite body) of the Luobusa ophiolite sampled by the field survey by Yamamoto and others in 2001 (Yamamoto et al., 2007; Yamamoto et al., 2009) were used. Studied samples are listed in Table 4-1. One chromitite pod (LT69) and associated peridotites (dunite, LA40, LA52; harzburgite, LA39, LA38) were examined for their genetic relationship. LA326 chromitite in the central part contains a coesite lamella-bearing spinel (Yamamoto et al., 2009). The Cr-11 chromitite body (LA509-565) is well known as the largest chromitite body in the eastern Tibet and abundance of diamond and other UHP minerals (e.g., Xu et al., 2009).

4.3.2: *Ray-Iz ophiolite, Polar Urals*

The Ray-Iz ophiolite is located on the Polar Urals, and extends around 50-100km from SW to NE, along the northern Ural Mountains (Fig. 4-2). This ophiolite is interpreted to have been formed by the collision of the Magnitogosrk arc and the East Europian continent block in the mid-Paleozoic around 400 Ma ages, based on U-Pb age of zircon in the gabbro and diorite, and whole-rock Sm-Nd isotope study of peridotite (e.g., Savelieva and Nesbitt 1996; Shmelev and Meng 2013). Constituent rocks in this region reflect a series of westward-directed thrust stacks in which the oceanic and arc

sequences lie on the continental margin of the European plate (Savelieva and Nesbitt 1996). The Ray-Iz ophiolite complex mainly consists of lherzolite, harzburgite, dunite and gabbro (Shmelev 2011).

Studied chromitites were collected from No.384 chromitite body in the Central Chromitite Deposit area and p.t. 214 chromitite body in the western part of the Ray-Iz massif (Fig. 4-2, 3), by our field expedition in 2013 (Table 4-1). The Central Chromitite Deposit area is located in the thick dunite body in the mantle section close to the crustal section, and contain largest abundance of chromitite pods (e.g., Shmelev 2011; Yang et al., 2014). Diamond and other unusual UHP minerals were found both from the No.384 body in the Central Chromitite Deposite and from the p.t.214 chromitite body in the western part of the Ray-Iz massif (Yang et al., 2014).

4.4: Petrography

Chromitites and peridotites from the Luobusa ophiolite

Most of chromitites from the Luobusa ophiolite are vein-like or lenticular in shape, and exist with dunite envelopes (several centimeters to several meters thick) in fresh harzburgite (Zhou et al., 1996; Yamamoto et al., 2009; Xu et al., 2011). They are mostly concordant to foliation of the surrounding harzburgite (Yamamoto et al., 2009). Chromitites show various textures, such as massive, disseminated, nodular, anti-nodular, dunitic orbicular and banded textures (Zhou et al., 1996; Yamamoto et al., 2009; Xu et al., 2011). Most of them show massive textures (Xu et al., 2011).

The Luobusa chromitites comprise subhedral to anhedral chromian spinel and olivine, which is moderately to strongly serpentinized. Chromian spinels in the Luobusa chromitites are reddish to dark brown in thin section, indicating their Cr-rich character (Fig. 4-4). Spinels in the massive and nodular textured chromitite from Cr-11 body in the eastern part are sometimes cleaved by olivine-filled fracture, indicating deformation under high temperature condition (Fig. 4-4) (Arai 2013). Some of olivines from chromitites are kinked. Spinels from the Luobusa chromitites typically contain numerous needle- and rod- shaped exsolution lamellae of diopside and coesite, showing parallelism (Yamamoto et al., 2009). The silicate lamellae notably exist in spinel from massive and nodular textured chromitites. Chromian spinels from

disseminated chromitites are apparently poor in silicate lamellae. Spinels in the Luobusa chromitites are free of primary inclusions that show concentric arrangement such as those in the Oman discordant chromitite (Fig. 4-4a). Some of them, however, sometimes contain minute globular inclusions showing sparse distribution such as those in the Oman concordant pods (Fig. 4-5b). Trails of secondary inclusions, composed of serpentine and minor mount of chlorite, are typically contained in spinel from the Luobusa chromitites (Miura et al., 2012; Huang et al., 2014). Some of such secondary inclusions occur as negative crystals. Fluid-phase secondary inclusions sometimes exist in chromian spinel of chromitites. Some of chromian spinel grains in the Luobusa chromitites contain euhedral to subhedral metallic inclusion, showing an isolated distribution (Fig. 4-6a). Multi-phase metallic inclusions rarely appear within chromian spinel in the diamond-bearing UHP chromitite from the Cr-11 pod (Fig. 4-6b). Silicate mineral phases are sometimes associated with metallic inclusion (Fig. 4-6c, d) in the Luobusa chromitites except in the diamond-bearing UHP chromitite.

Dunites enveloping the LT69 chromitite located in the western part of Luobusa ophiolite are coarse-grained and moderately to strongly serpentized. Dunites comprise olivines, euhedral to subhedral spinels and minor amount of interstitial clinopyroxenes (Fig. 4-4), and show a porphyroclastic texture. Olivines sometimes show wavy extinction. Some spinel grains in the dunite envelope contain silicate inclusions composed of amphibole and chlorite.

Harzburgites, moderately serpentinized, around LT 69 pod show prominant porphyroclastic textures (Fig. 4-4), and comprise olivine, orthopyroxene, subhedral to anhedral spinel and small amount of clinopyroxene, which is closely associated with orthopyroxene. Some of their olivines and orthopyroxenes are kinked, suggesting deformation. Ambient harzburgites (LA 182, 246, 258) far from chromitites, containing clinopyroxene, show porphyroclastic texture. Their spinels are transparent reddish in color, indicating their Al-rich character (Fig. 4-4). In contrast, the ambient harzburgite (LA190) contain reddish brown colored spinels and small amounts of amphibole, suggesting hydration.

Chromitites and peridotites from the Ray-Iz ophiolite

The No.384 body in the Central Deposite of the Ray-Iz ophiolite extends about 150m in length and 2-3m in thickness, in a north-south direction. The p.t. 214 body in the western part of the Ray-Iz ophiolite extends 200m in length and 4-5m in thickness (Fig. 4-2, 3). Both chromitites are mostly concordant to the foliation of surrounding peridotites (Fig. 4-2). Chromitites in the Central Deposite show various textures, such as nodular, massive, disseminated and banded textures (Figs. 4-3b, c). Some of olivines are huge in size in the surrounding dunite of No.384 pod (Fig. 4-3d). Peridotites adjacent to No.384 pod typically contain talc+chlorite+tremolite aggregates, which are whitish on the outcrop (Figs. 4-3e, f), suggesting a low-T metamorphic feature. Chromitites from the p.t. 214 body in the western part of the Ray-Iz massif show various textures, such as nodular, anti-nodular, massive and disseminated textures, and contain kämmeririte (Cr-rich chlorite), indicating hydrothermal alteration.

Chromitites in the Central Deposite, including the No.384 body, are mainly composed of euhedral to subhedral chromian spinel and olivine, which is sometimes strongly serpentinized. Chromian spinels in the Central Deposite chromitites are reddish to dark brown in thin section, indicating their Cr-rich character (Fig. 4-4). Spinels in the massive and nodular textured chromitite are sometimes cleaved by olivine-filled fracture (Fig. 4-4). Spinels in the chromitites from the No.384 body typically contain numerous silicate lamellae, which are similar to those in the Luobusa UHP chromitites (Fig. 4-5). They show parallelism, possibly indicating a subdsolidus exsolution origin. Such lamellae notably exist in spinels from massive No.384 chromitite and nodular textured chromitite, although chromitites containing lamella-free spinel also exist in the Central Deposite. Cleavable olivines sometimes exist in chromitite and surrounding peridotite (Fig. 4-4). Spinels in the Central Deposite chromitites are free of primary inclusions, such as in the Oman discordant chromitite (Figs. 2-9a, 4-4g). Minute irregular shaped inclusions sometimes appear in spinel (Fig. 4-5b). Trails of secondary inclusion, composed of chlorite and rare serpentine, appear within spinel in the Central Deposite chromitites. Such secondary inclusions occur as negative crystals (Fig. 4-5i). The trails of fluid-phase secondary inclusions also exist within chromian spinel of chromitites (Fig. 4-5j).

Dunites forming the envelopes of the No.384 body chromitite and the p.t.214 body chromitite are coarse-grained and weakly serpentinized (Fig. 4-4l). Chromian spinel is euhedral to subhedral in both dunites. Some of olivines in dunites of the No.384 pod and the p.t. 214 pod have conspicuous cleavages (Fig. 4-4k, l). Opaque mineral inclusions are sometimes included by olivine in dunite envelopes of the No.384 pod and p.t. 214 pod (Fig. 4-4o). Grain boundaries of olivines in both dunites from two localities sometimes show 120-degree triple junctions in thin section, suggesting recrystallization.

Harzburgites surrounding the No.384 pod and the p.t.214 pod comprise subhedral to anhedral spinel, moderately serpentinized olivine, orthopyroxene, talc, chlorite and tremolite (Fig. 4-4m). Spinels are sometimes opaque in thin section. Many of spinels in harzburgites contain chlorite and serpentine inclusions along the rim of host spinel. Some of olivine grains in surrounding harzburgites are "cleavable" in some dunites enveloping chromitites of the No.384 and the p.t. 214 pods (Fig. 4-4n). Some of olivine and orthopyroxene grains in harzburgites from both the pods occasionally contain euhedral-shaped opaque inclusions. Orthopyroxene is relatively coarse and subhedral. Talc, chlorite and tremolite in harzburgites usually make an aggregate. Chlorite is sparsely distributed all around in harzburgites, especially around spinel. Tremolite is mostly subhedral, sometimes partly or completely included by orthopyroxene grains. Harzburgites examined in this study are free of clinopyroxene.

4.5: Mineral chemistry

4.5.1: *Major-element chemistry*

Chromitites and peridotites from the Luobusa ophiolite

Chromian spinels from diamond- and coesite-bearing chromitites from the Luobusa ophiolite are generally similar in chemical characteristics to each other (Fig. 4-8). Spinels from chromitites show high Cr#s around 0.75 to 0.80, and low TiO_2 contents around 0.10 to 0.25 wt% (Table 4-2). The Cr# of spinel in diamond-bearing chromitite (Cr-11 body) is around 0.8, and slightly higher than in other chromitites (Fig. 4-8). Spinels in dunite envelope (LT40, LT52) are characterized by relatively high Cr#s (0.50 to 0.75) and low TiO_2 contents (0.10 to 0.20) (Fig. 4-8). Chromian spinels from

harzburgites adjacent to dunite envelope around chromitite (LT69) show relatively low Cr#s, 0.40 to 0.45, and low TiO_2 contents, 0.10 to 0.20. Ambient harzburgites contain spinels characterized by low Cr#s (0.15 to 0.30) and low TiO_2 contents (< 0.10 wt%). The Cr# of spinel is noticeably higher in one distant harzburgite (LA190), which contains tremolite (Figs. 4-3, 8).

Olivines in the Luobusa chromitites show unusually high Fo (Fo_{96-98}) and NiO contents (0.65 to 1.15 wt%), probably due to subsolidus exchange (Fig. 4-8) as discussed before (Table 4-3). Olivines from dunite enveloping the LT69 chromitite are relatively high in Fo content (93-95) and NiO content (0.45 to 0.55 wt%) (Fig. 4-8; Table 4-5). Olivines in harzburgites adjacent to the dunite envelope are Fo_{91-93} and contain 0.37 to 0.45 wt% NiO. Ambient harzburgites far from chromitite pods contain olivines characterized by Fo_{90-91} and 0.25 to 0.48 wt% NiO (Fig. 4-8). Harzburgites plot almost in the field of residual mantle peridotite in mineral chemical spaces (e.g., Arai 1994) (Fig. 4-8).

Orthopyroxenes in the harzburgite adjacent to dunite show relatively low Al_2O_3 contents, 0.6 to 1.0 wt%, and CaO contents, 0.5 to 1.1 wt% (Fig. 4-8f; Table 4-5). The Al_2O_3 and CaO contents in orthopyroxenes in ambient harzburgites vary from 2.2 to 4.5 wt% and 0.4 to 1.6 wt%, respectively. The Mg# of clinopyroxenes in the harzburgite near dunite envelope, and the ambient harzburgites varies from 0.92 to 0.95 and 0.93 to 0.94, respectively (Fig. 4-8g). Clinopyroxenes in the dunite envelope show high Mg#s (0.95 to 0.97) and relatively low Al_2O_3 contents (0.4 to 1.5 wt%) (Table 4-4). The ambient harzburgite clinopyroxenes have relatively low TiO_2 contents (0.1 to 0.15 wt%) and Na_2O contents (0.1 to 0.2 wt%). Clinopyroxenes in the harzburgites adjacent to dunite are high in Na_2O (0.28 to 0.45 wt%) and relatively low in TiO_2 (0.05 to 0.15 wt%). Clinopyroxenes in the dunite envelope are characterized by high Na_2O contents, 0.2 to 0.52, and low TiO_2 contents, up to 0.08.

Qualitative and quantitative microprobe analyses revealed that the euhedral to subhedral metallic inclusions in spinels from the Luobusa diamond- and coesite-bearing chromitites are composed of erlichmanite (OsS_2), laurite (RuS_2), Ir-Ni sulfide and small amount of copper sulfide (Figs. 4-6a, b; Table 4-7). PGE alloys have not been found from the Luobusa UHP chromitites in this study, although Bai et al. (2000)

and Robinson et al. (2004) reported them. There is a distinct compositional gap between laurite and erlichmanite in the Luobusa chromitites. Laurites show an Os-rich variety, in which the Ru/(Ru+Os+Ir) atomic ratio ranges from 0.71 to 0.88 (Fig. 4-11b; Table 4-7). The Os content in laurites varies from 6.2 up to 23.1 wt%. The range of Ir content in laurite grains is from 2.4 to 8.9 wt%. Erlichmanites show a high variability in Os/(Ru+Os+Ir) atomic ratio, 0.44 to 0.71 (Fig. 4-11b). The Ir content in erlichmanite grain varies from 7.3 to 13.3 wt% (Fig. 4-11b). Unnamed Ir-Ni sulfide contains S, Ir, Rh, Ni, Cu and Fe, and shows a representative chemical formula of $(Ir_{0.97}Rh_{0.03})(Ni_{0.52}Cu_{0.26}Fe_{0.22})_{\Sigma 2}S_3$. Such an Ir-Ni sulfide has been reported by Garuti et al. (1999) and Ahmed and Arai (2003), as unnamed $(Ir,Rh)(Ni,Cu,Fe)_2S_3$. The (Ni+Cu+Fe)/(Ir+Rh) ratio varies from 1.86 to 4.10. The mineral contains minor amounts of Os, Ru and Pt, with average concentrations of 2.42, 2.95 and 0.47 wt%, respectively.

Chromitites and peridotites from the Ray-Iz ophiolite

Spinel in chromitites from the No.384 and p.t.214 pods show high Cr# (0.80 to 0.85) and low TiO_2 contents (up to 0.2 wt%) (Figure 4-8; Table 4-2). Chromian spinels in dunites enveloping chromitites from both the mines also are high in Cr# and low in TiO_2 contents as in chromitites, and obviously show higher $Fe^{3+}/(Cr+Al+Fe^{3+})$ cation ratios than in chromitites (Fig. 4-8). Spinels in harzburgites surrounding both the chromitites from the Central Deposite and the western deposite are characterized by greater variability of Cr# (0.68 to 1.0), Mg# (0.1 to 0.5), $Fe^{3+}/(Cr+Al+Fe^{3+})$ (up to around 0.8) and TiO_2 (up to 0.4 wt%) of spinel than in chromitites and dunites (Fig. 4-8).

Olivines in UHP chromiites from the Central mine and the western deposite show high Fo contents (Fo97-98) and high NiO contents (0.65 to 0.83 wt%) as in UHP chromitites from the Luobusa ophiolite (Fig. 4-8; Table 4-3). In addition, Yang et al. (2014) reported that olivines are extraordinarily high in NiO (up to 1.4 wt%) from the diamond-bearing UHP chromitites in the Ray-Iz ophiolite. Olivines from dunite enveloping the chromitite from the No.384 pod show relatively high Fo contents (93-97) and NiO contents (0.35 to 0.55 wt%) (Fig. 4-8). Olivines in harzburgites adjacent

to dunite envelope show Fo_{91-93} and 0.30 to 0.43 wt% NiO contents. Distant harzburgites contain olivines characterized by $Fo_{90.5-91.5}$ and 0.28 to 0.35 wt% NiO (Fig. 4-8). Harzburgites plot almost in the field of residual mantle peridotite in mineral chemical spaces, however they contain high-Cr# spinel and relatively high-Fo olivine (Fig. 4-8b).

Orthopyroxenes in the harzburgite from the Ray-Iz ophiolite show typically low Al_2O_3 contents, up to 0.5 wt%, and CaO contents, up to 0.2 wt% (Fig. 4-8f; Table 4-5). Their Cr_2O_3 contents in orthopyroxenes are also low, up to 0.1 wt%. Compositional characteristics of orthopyroxene are similar to those in some of meta-peridotite (e.g., Arai 1974).

4.5.2: *Trace-element chemistry*

Chondrite-normalized rare earth-element patterns of clinopyroxenes from dunite and harzburgites surrounding the LT69 chromitite pod in the Luobusa ophiolite are characterized by depletion in LREE (Fig. 4-10a; Table 4-6). Clinopyroxenes are more enriched in LREE, in the dunite envelope than in the surrounding harzburgites. Chondrite-normalized REE pattern of clinopyroxene in the dunite shows a decline from Dy to Lu, and shows overall higher levels of MREE than in the surrounding harzburgite (Fig. 4-10a). In contrast, depletion of HREE does not appear in REE patterns of clinopyroxenes in surrounding harzbugites. Clinopyroxenes are highly depleted in LREE in surrounding harzburgites. The concentrations of HREE, e.g., Yb and Lu, in clinopyroxene are lower in the harzburgites adjacent to dunite enveloping chromitite that in the distal harzburgite. Relationships of Ti and Zr in clinopyroxene indicate that surrounding harzburgites of LT69 chromitite pod are plotted around the compositional field of abyssal peridotites (Fig. 4-10). Clinopyroxenes show lower Zr contents in the ambient harzburgite than in the proximal harzburgite to chromitite pod. Dunite is slightly beyond the field for abyssal peridotites, and plotted along a residual trend under water saturated, and low-degree (10%) partial melting (Barth et al., 2003).

4.6: Raman spectroscopy of minute inclusions in minerals

Raman spectroscopy indicates that exsolution lamella in spinels are mainly composed

of clinopyroxene in chromitites both from Ray-Iz and Luobusa (Fig. 4-7a). Coesite lamella (Yamamoto et al., 2009) and UHP minerals have not been found from the Ray-Iz chromitites in spite of carefull search by Raman spectroscopy. Globular inclusions in chromian spinel from No.384 chromitite pod in the Central Deposite mainly consist of clinopyroxene (Fig. 4-7b). Minute globular inclusions in spinel in the coesite-bearing UHP chromitite (LA326) from Luobusa (Yamamoto et al., 2009) are mainly composed of clinopyroxene and pargasitic amphibole beased on Raman spectroscopic features. OH stretching modes (around 3672-3675 cm^{-1}) of the Raman spectrum of the inclusion strongly indicates that the globular inclusions consist of amphibole in the Luobusa coesite-bearing UHP chromitite (Fig. 4-7c). In contrast, globular inclusions in spinels in the diamond-bearing UHP chromitite (the Cr-11 body) from Luobusa and in the Ray-Iz UHP chromitites consist of clinopyroxne and subordinate olivine. Hydrous minerals, such as pargasite and Na phlogopite, have not observed in primary inclusions in spinel from the Luobusa diamond-bearing and the Ray-Iz UHP chromitites. Solid-phased secondary inclusions (Fig. 4-4) in spinel are mainly composed of serpentine from the Luobusa UHP chromitites (Miura et al., 2012; Huang et al., 2014), and consist of chlorite and subordinate serpentine from the Ray-Iz UHP chromitites. Raman spectra of fluid-phase secondary inclusions in spinel from the Luobusa and the Ray-Iz chromitites, unfortunately, have not been detected because of absorption of Raman scattering light by the host chromian spinel (showing dark reddish brown to black color in thin section). Secondary fluid inclusions in olivine in the Ray-Iz UHP chromitites are mainly composed of methane.

4.7: PGE chemistry of UHP chromitites

The Luobusa diamond-bearing and coesite-bearing chromitites are high in total PGE, 193 and 233ppb, respectively (Fig. 4-11c; Table 4-8). All chromitite samples from the Luobusa ophiolite are distinctly enriched in the Ir subgroup (IPGE), i.e. Os, Ir and Ru, in preference to the Pd subgroup (PPGE), i.e. Rh, Pt and Pd (Figs. 4-11c, d). Most of samples show negatively sloped chondrite-normalized PGE patterns (Figs. 4-11c, d), similar to chromitites from Tibet and other typical ophiolitic chromitites (e.g., Leblanc 1991; Zhou et al., 1996; Ahmed and Arai 2002). The diamond-bearing chromitite (the

Cr-11 body) shows a slightly higher concentration in PPGE and a gentler negative slope than the coesite-bearing chromitite (LA326) and others in the Luobusa ophiolite (Zhou et al., 1996). The Luobusa chromitites are generally intermediate in PGE patterns between the mantle discordant chromitites and the MTZ chromitites from the northern Oman ophiolite (Ahmed and Arai 2002).

The Ray-Iz diamond-bearing chromitite (No.384 body) and other chromitites are high in total PGE, 223 to 450 and 83 to 444 ppb, respectively (Table 4-8). The Ray-Iz chromitites show negative slopes from Ru to Pt in their chondrite-normalized PGE patterns (Fig. 4-11d) as in typical ophiolitic chromitites. The diamond-bearing Ray-Iz chromitite (No.384 body) shows a lower ratio of Pd/Ir (around 0.026) and a higher concentration in IPGE than other pods in the Ray-Iz ophiolite, which show a high Pd/Ir ratio around 0.282 and a positive slope from Pt to Pd (Fig. 4-11d).

4.8: Discussion

4.8.1: Similarity between the Luobusa and Ray-Iz UHP chromitites

The occurrence of UHP chromitites both in the Luobusa and in the Ray-Iz ophiolites are concordant to the foliation of surrounding harzburgite (Figs. 4-1c, 2c-d) (Yamamoto et al., 2009). This suggests that the UHP chromitites have experienced deformation via mantle convection flow (Cassard et al., 1981; Arai 2010, 2013). As this supportive evidence, spinels in the UHP chromitites in the Luobusa and the Ray-Iz ophiolites are sometimes cut by olivine-filled fracture, suggesting deformation in high-T condition (Arai 2013). Such a deformation texture is absent in LP chromitites from the Oman ophiolite. In addition, olivines in both UHP chromitites with high-T deformation textures show extraordinarily higher Mg and Ni contents than those in the Oman LP chromitites (Figs. 2-11, 4-8) (Yang et al., 2014). Atypical Mg and Ni contents in olivine in the UHP chromitites suggest that both the Luobusa and Ray-Iz UHP chromitites have experienced long duration of subsolidus cooling, which induced diffusion of Mg and Ni from chromian spinel in chromitites to olivines in the surrounding dunite (Fig. 4-8) (e.g., Ozawa 1984). Existence of silicate lamellae within spinel in UHP chromitites is apparently consistent with long subsolidus cooling. The concordant chromitite along Wadi Hilti, the northern Oman ophiolite, shows a trace of

Mg and Ni diffusion in olivine in the dunite envelope and contain spinels with pyroxene lamellae as shown in Chapter 2-8 (Miura et al., 2012). Such characteristics of the Oman concordant pod support the long duration of subsolidus cooling of the UHP chromitites. Chromian spinels show high Cr#s and low TiO_2 contents in both the UHP chromitites and their dunite envelope, indicating their arc-related signature (e.g., Arai 1994). Spinel chemistry of the UHP chromitites is similar to that of the discordant chromitites from the Oman ophiolite (Figs. 2-11, 4-8). These textural and petrological features of the UHP chromitites in the Luobusa and the Ray-Iz ophiolites suggest that the UHP chromitites possibly formed by at a similar tectonic setting. Peridotites surrounding the UHP chromitites in the Luobusa and the Ray-Iz ophiolites, however, show completely different characteristics from each other (Fig. 4-8). The Luobusa peridotites essentially show a residual feature after extraction of MORB-like magma (Figs. 4-8, 10) (Zhou et al., 1996, 2005), except one clinopyroxene-free hydrated sample (LA190). In contrast, surrounding peridotites in the Ray-Iz ophiolite are clearly of metamorphic origin under water-saturated and low-T conditions, based on the existence of chlorite+tremolite+talc aggregate and the mineral chemistry (Figs. 4-4, 8).

The primary hydrous mineral, such as pargasite, inclusions (Fig. 2-9) are apparently absent in spinels of the UHP chromitites from the Luobusa and the Ray-Iz ophiolites (Figs. 4-4, 5). Pargasitic amphibole inclusions showing sparce distribution, however, were found from spinel in the coesite-bearing Luobusa UHP chromitite (LA326), by carefull examination using Raman spectroscopy (Figs. 4-5b, 6, 7c). On the other hands, spinels in the diamond-bearing Luobusa chromitite (Cr-11 body) and Ray-Iz chromitites (No.384 and p.t.214 bodies) are free of amphibole inclusions. It is important to note that the coesite lamella possibly coexists with pargasitic amphibole in spinel of same UHP chromitite sample (LA326) in the Luobusa ophiolite, examined by Yamamoto et al. (2009). In consideration of the coexistence of coesite and Na amphibole (pargasite), the LA326 chromitite has possibly experienced relatively low-T (around 700 to 800 °C) and high-P (around 3 GPa) conditions (Fig. 4-13a) (e.g., Mirward and Massone 1980; Niida and Green 1999; Frost 2006; Naemura et al., 2011). If we consider geotherms of the upper mantle (Fig. 4-13a), coesite and amphibole bearing UHP chromitite can be formed by UHP metamorphism in a subduction zone

environment rather than deep mantle origin beneath mid-ocean ridge suggested by Ruskov et al. (2009) and Yang et al. (2014).

4.8.2: Comparison with the Higashi-Akaishi chromitite

Chromitites from the Higashi-akaishi ultramafic complex in the Cretaceous Sanbagawa metamorphic belt, Japan (e.g., Enami and Mizukami 2004), are compared with the UHP chromitites from the Luobusa and Ray-Iz ophiolites, to summarize the characteristics of high-P metamorphosed chromitite and constrain the origin of UHP chromitite. The Higashi-Akaishi ultramafic complex is characterized by the presence of garnet-bearing peridotites and pyroxenites, and interpreted as a high-P metamorphic (up to around 3.8 Pa) complex originally formed at a lower-P condition (Enami and Mizukami 2004; Mizukami and Wallis 2005; Hattori et al., 2010). The chromitites from the Higashi-Akaishi ultramafic complex had also experienced the high-P metamorphism. The Higashi-Akaishi chromitites will give us information on the behavior of low-P chromitite upon compression via subduction (Arai 2013).

Chromian spinels in the Higashi-Akaishi chromitite show high Cr#s (0.8 to 0.85) and low TiO_2 contents (around 0.1 wt%), suggesting an arc-related feature (Arai 1994). The compositional range of the Higashi-Akaishi chromitites is similar to those of the Luobusa and the Ray-Iz UHP chromitites (Fig. 4-8). Primary globular inclusions of hydrous minerals, such as pargasite and Na phlogopite, are completely absent in spinels in the Higashi-Akaishi chromitites (Fig. 4-12a). In addition, spinels in the Higashi-Akaishi chromitites contain thin lamellae of diopside (Fig. 4-12b). Solid-phase secondary inclusions are mostly composed of chlorite and serpentine. The Higashi-Akaishi chromitite is similar in these characteristics of inclusions in spinel to the UHP chromitites from the Luobusa and the Ray-Iz ophiolites. This suggests that some of characteristics of the UHP chromitite can be formed by compression of low-P chromitite, e.g., by its recycling suggested by Arai (2013).

4.8.3: Systematic differences between the UHP and Oman LP chromitites

The UHP chromitites in the Luobusa and the Ray-Iz ophiolites are similar in texture (typically nodular) such as nodular texture, as well as in spinel chemistry to the

discordant chromitites from the Oman ophiolite (Ahmed and Arai 2002; Miura et al., 2012). Characteristics of micro inclusions in spinel, such as primary hydrous mineral inclusion and silicate exsolution lamella, however, are completely different betweem the UHP chromitites and the discordant chromitites (Figs. 2-9, 4-5). The Oman concordant chromitites have similar characteristics in some ways to the UHP chromitites. However, the appearance of primary hydrous mineral inclusion in spinel and the lack of UHP mineral are clearly different ways between the Oman concordant chromitites and the UHP chromitites. Such contrasted characteristics between the UHP chromitites and the LP chromitites indicate the difference in their origins and history; the former have experienced UHP metamorphism (compression) and long duration of subsolidus cooling, the latter was of shallow magmatic origin.

4.8.4: Origin of UHP chromitites

Rare-earth element patterns of clinopyroxene in dunite enveloping the amphibole-bearing Luobusa chromitite (LT69) show a depletion in HREE, i.e. Lu and Yb (Fig. 4-10a). The depletion in HREE of clinopyroxene suggests that it has been equilibrated with garnet (e.g., Ionov 2003), but, such any features of involvement of garnet could not be found in harzburgites adjacent to the dunite and chromitite (Fig. 4-10a). For example, garnets and their breakdown products, such as spinel-pyroxenes symplectite, are not observed in dunite and harzburgite (e.g., Kushiro and Yoder 1966; Morishita and Arai 2003). These are two possibilities for depletion of HREE contents in clinopyroxene from the dunite envelope; (1) the dunite and chromitite formation (melt/wall rock reaction and subsequent melt mixing) at the garnet-stability depth, and (2) formation of garnet peridotite from spinel-peridotite phase secondary through deep recycling at a subduction zone. Coexistence of coesite and amphibole in spinel from the LA326 chromitite from Luobusa, suggests the UHP metamorphism in a supra-subduction zone (Fig. 4-13). Furthermore, Huang et al. (2014) suggested that UHP chromitites (Cr-11 body) and surrounding peridotites in the Luobusa ophiolite experienced deserpentinization and subsequent high-pressure metamorphism, forming UHP minerals, based on the occurrence of serpentine minerals in chromitite and surrounding harzburgites. These characteristics of other chromitite pods in Tibet seem

likely to be consistent with the latter possibility, deep recycling at a subduction zone (Arai 2013). This is supported by the similarity in characteristics of inclusion in spinel between the Luobusa UHP chromitites and the Higashi-Akaishi chromitite, which experienced the high-P metamorphism due to subduction (Fig. 4-10) (e.g., Enami and Mizukami 2004). If we consider the UHP metamorphism at a subduction zone for the origin of some of the Luobusa chromitites, the HREE-depleted pattern of clinopyroxene in surrounding harzburgites was possibly reset to the flat-HREE pattern via reaction and recrystallization due to partial melting at the spinel-peridotite depth (Fig. 4-10). Dunite envelope has retained HREE characteristics of clinopyroxene. On the other hand, peridotites surrounding the Ray-Iz chromitites are characterized by the presence of high-Fo and cleavable olivine, magnetite inclusion in olivine and chlorite+tremolite+talc mineral species, suggesting high-P deserpentinization and recrystallization (Figs. 4-4, 8). The enrichment of Mg and Ni in olivine in the dunite adjacent to the Ray-Iz UHP chromitite probably indicates their diffusion from chromitite due to cooling after deserpentinization and recrystallization (Fig. 4-9). As mentioned above, petrological characteristics of surrounding peridotites from Luobusa and Ray-Iz suggest that the surrounding peridotites from both the ophiolites have experienced high-P metamorphism at a subduction zone.

However, some unusal minerals may suggest their origin from deeper mantle, such as the mantle transition zone, rather than in a subduction zone mantle (Robinson et al., 2004; Yang et al., 2007, 2014; Xu et al., 2009; Yamamoto et al., 2009). For example, possible coesite pseudomorphs after stishovite would require pressures around > 9 GPa (Yang et al., 2007). Such unusual minerals seem likely to originate from the mantle transition zone beneath a mid-ocean ridge (e.g., Robinson et al., 2004; Yang et al., 2007, 2014), if we consider transportation of UHP minerals by mantle upwelling flow and abyssal nature for surrounding peridotite (e.g., Zhou et al., 1996, 2005). Some PGE and other alloys have been found from the Luobusa UHP chromitites (Bai et al., 2000; Robinson et al., 2004; Yang et al., 2014). Some PGE (Os-Ir-Ru) alloys from the Luobusa UHP chromitites show unusually older ages (around 270 Ma) than the host Luobusa ophiolite age (around 170 Ma), based on Os isotopic study (Shi et al., 2007). Robinson et al. (2004) and Yang et al. (2014) suggested that

PGE and other alloys from the UHP chromitites were possibly originated from highly reduced deep mantle, such as the mantle transition zone. Arai (2013) explained that PGE alloys were formed by heating of originally PGE sulfides in LP chromitites (e.g., Ahmed and Arai 2002) via deep recycling, because of the absence of PGE sulfides in the Luobusa UHP chromitites reported by Bai et al. (2000). However, some PGE sulfides, such as laurite and erlichmanite, coexist with alloys in the same sample of the Luobusa UHP chromitites (Fig. 4-6). Their origin and relatihonship with PGE alloys are unclear, because detailed studies based on PGM and PGE are very limited at present. The PGE sulfides, associated with hydrous silicate inclusions showing sparce distribution (Fig. 4-6), seems likely to be of primary origin. Ruskov et al. (2010) and Yang et al. (2014) suggested the UHP magmatic origin. However, it cannot well explain some characteristics of UHP chromitites, such as the presence of dunite envelope and other igneous textures similarly seen in LP chromitites (Arai 2013).

At present, although systematical studies are very limited, the recycling origin of the UHP chromitites (Arai 2013) is convincing, because it can well explain the coexistence of UHP and LP chromitite in the same ophiolite, similarities in the presence of dunite envelope and textures between UHP and LP chromitites, formation of silicate lamellae, and clearly older model age for PGE alloy and zircons in chromitite (Shi et al., 2007; Yamamoto et al., 2013). PGE patterns of UHP chromitites in the Luobusa and the Ray-Iz chromitites show slightly low Pd/Ir ratios and total PGE contents relative to those of the discordant chromitites in the northern Oman ophiolite (Fig. 4-11). Such a PGE distribution pattern can be formed by deep recycling of LP chromitite, because primary igneous PGE sulfides in LP chromitite are expected to be resolved into PGE alloys and S-rich melts or fluids at high-T condition (Andrews and Brenan 2002; Arai 2013). The UHP chromitites in the Luobusa and the Ray-Iz ophiolites are divided into two types in terms of mineral species as inclusion in spinel. One contains the coesite lamella (Yamamoto et al., 2009) and the amphibole primary inclusions in spinel. The other is characterized by the absence of the amphibole primary inclusion. The former can be formed by UHP metamorphism in a subduction zone, because of stable condition of coesite and amphibole. The latter UHP chromitites are possibly of deeper origin because of the absence of amphibole (Figs. 4-13, 14).

Silicate lamellae in spinel were possibly originated from the primary hydrous mineral inclusions, which commonly characterize the LP chromitite (Fig. 2-9) (Arai and Matsukage 1998; Borisova et al., 2012; Arai 2010, 2013). Primary inclusions are decomposed and silicate components are expected to be dissolved in host chromian spinel by compression and heating due to recycling (Fig. 4-14) (Brey et al., 1999; Aranovich and Kawasaki 2007; Arai 2010, 2013). Subsolidus cooling and decompression of chromitite probably triggered the exsolution of silicate components from chromian spinel (Yamamoto et al., 2009; Arai 2010, 2013). The high contents in Fo and Ni of olivine in UHP chromitites and their dunite envelopes suggest their long duration of subsolidus cooling and decompression (Fig. 4-8). The Ca-ferrite or Ca-titanite structures of high-P spinel as the precursor phase (Chen et al., 2003) probably are not necessary for origin of coesite and diopside lamellae (Yamamoto et al., 2009).

4.9: Figures and Tables

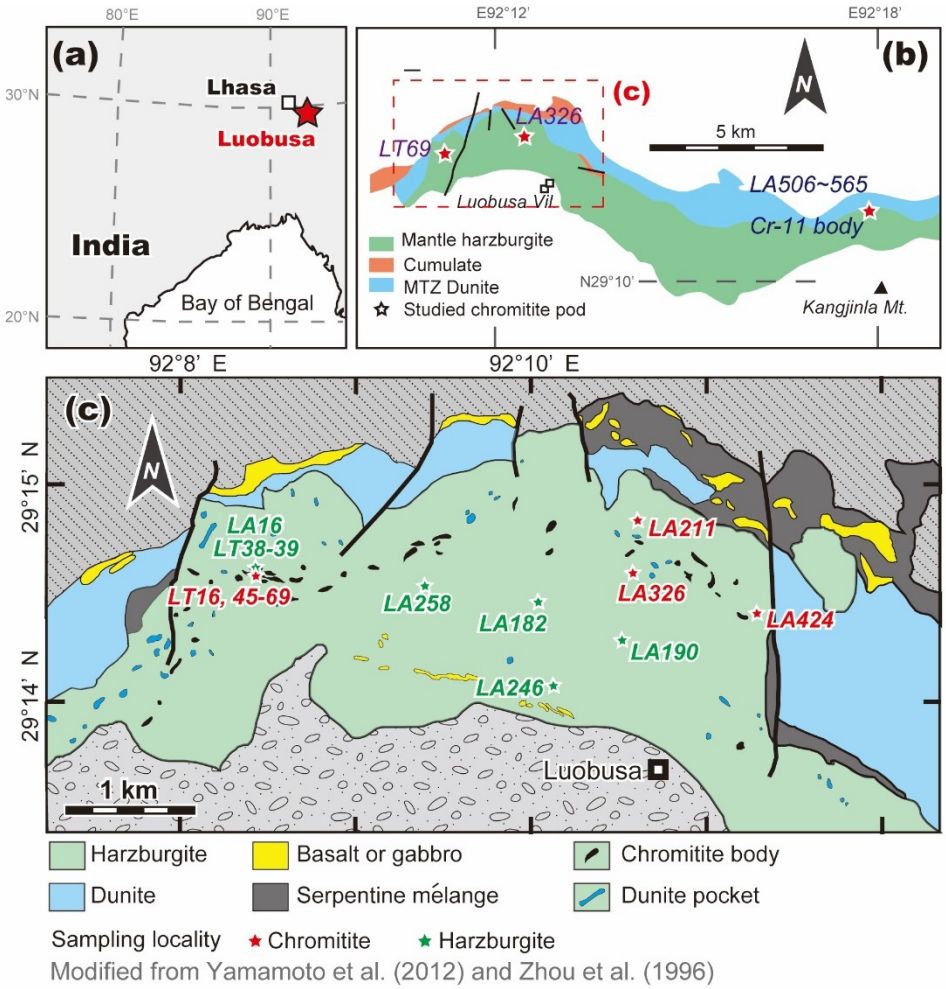

Figure 4-1. Locality and geological sketch maps of the Luobusa ophiolite. Modified from Zhou et al. (1996) and Yamamoto et al. (2009, 2012). (a) Location of the Luobusa ophiolite. (b) General geological sketch of the Luobusa ophiolite, Tibet. The Cr-11 chromitite body (diamond-bearing UHP chromitite) is located on the eastern part of the Luobusa ophiolite. (c) Distribution of chromitites on the geological sketch map of the Luobusa ophiolite. Star, sampling localities (The field expedition by Yamamoto and others 2002). Red star and green star indicate sampling locality of chromitite and harzburgite, respectively.

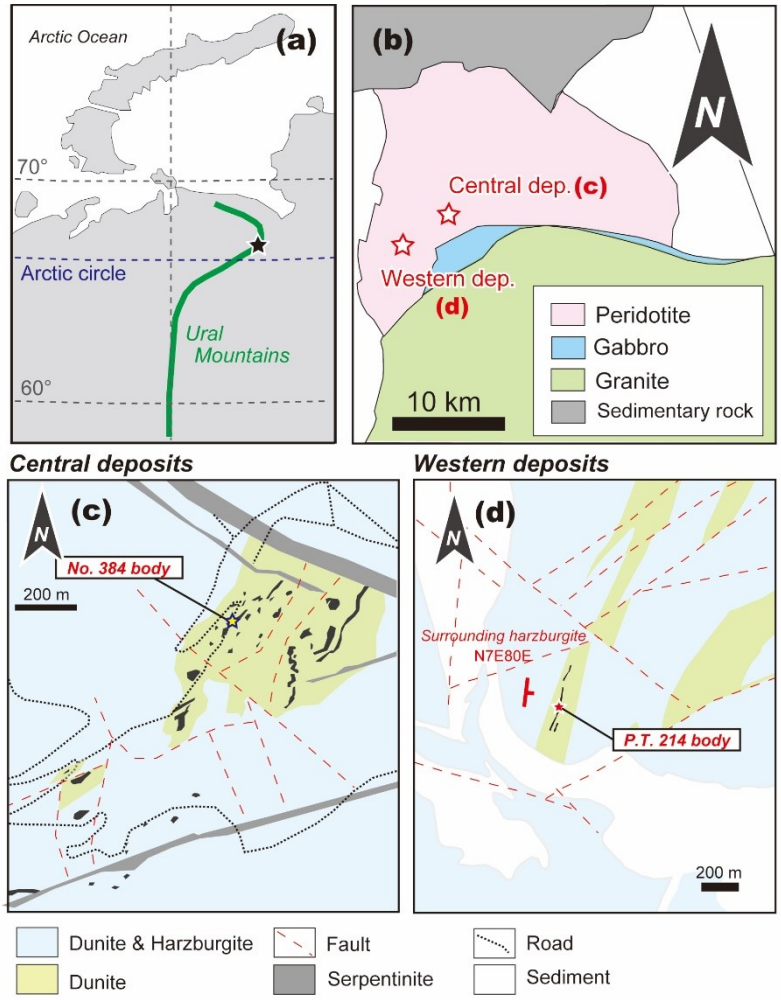

Modified from Shmelev et al. (2014) and Yang et al. (2014)

Figure 4-2. Locality and geological maps of the Ray-Iz ophiolite, Polar Urals. Modified from Shmelev (2011) and Yang et al. (2014). (a) Location of the Ray-Iz ophiolite. (b) Geological sketch map of the Ray-Iz ophiolite. (c) Geological sketch of No. 384 chromitite body in the central area of the Ray-Iz. (d) Geological sketch of p.t. 214 chromitite body in the western part of the Ray-Iz. Note that the ultrahigh-pressure chromitites in the Ray-Iz ophiolite are almost concordant to the foliation of the surrounding peridotite.

Figure 4-3. Outcrop photographs of ultrahigh-pressure chromitites and related rocks in the Ray-Iz ophiolite, Polar Urals. (a) No.384 chromitite pod, showing a sheet-like in shape, in dunite body in the central mine of Ray-Iz massif. (b) Disseminated to nodular textured chromitite from the central mine. (c) Nodular chromitite from the central mine. Yellow arrow shows olivine-filled fracture in grained spinel. (d) Megacrystalline olivine in dunite from from the central mine. (e) Foliated harzburgitic peridotite adjacent to the ultrahigh-pressure chromitite in the central mine. Arrow indicates chlorite + talc + tremolite aggregate, showing whitish part on the outcrop. (f) Distant harzburgite from ultrahigh-pressure chromitite in the central mine. (g) P.t. 214 chromitite body in the western part of Ray-Iz massif. (h) Massive to anti-nodular chromitite from p.t. 214 chromitite body.

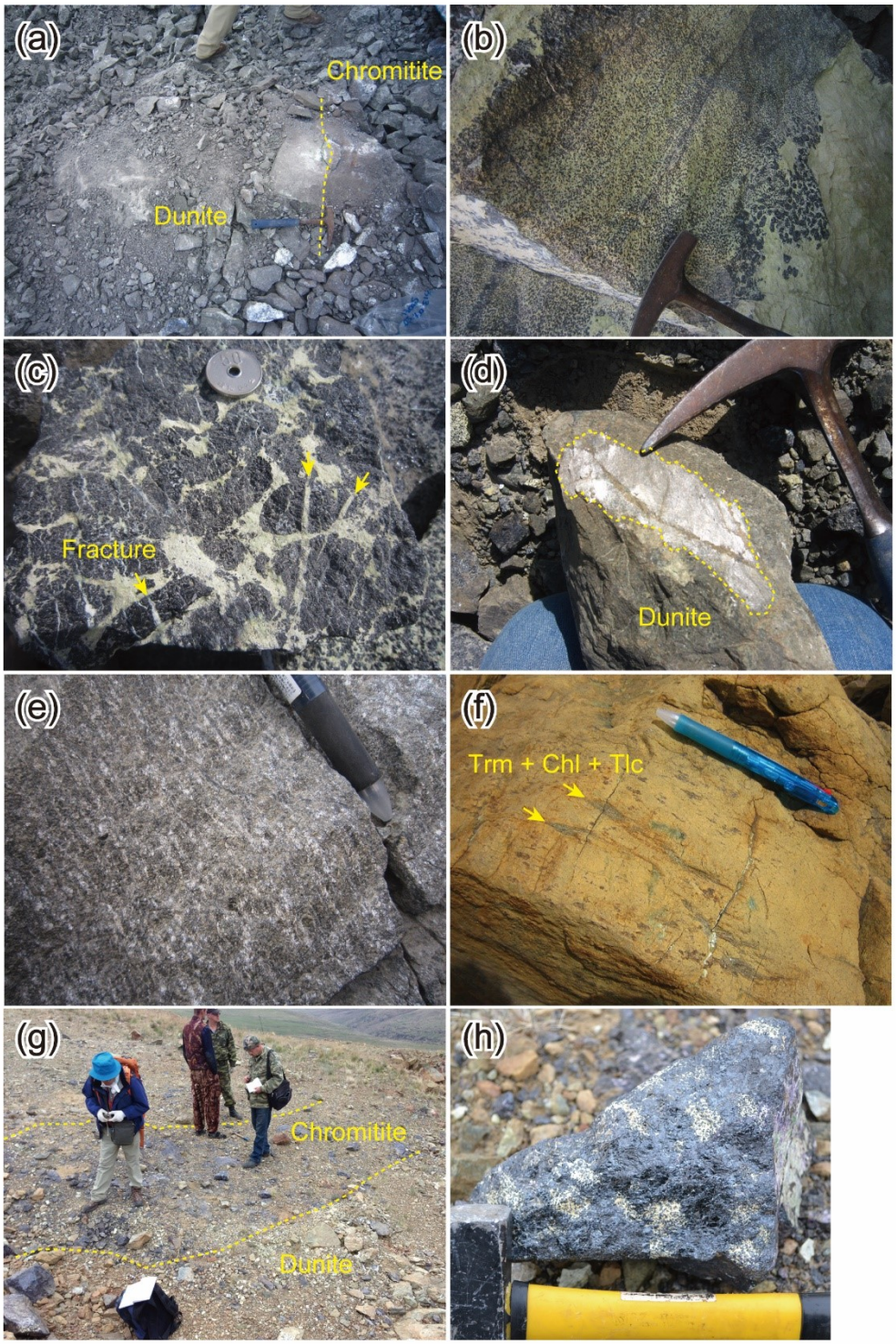
(a)
Chromitite
Dunite
(b)
(c)
Fracture
(d)
Dunite
(e)
(f)
Trm + Chl + Tlc
(g)
Chromitite
Dunite
(h)

Figure 4-3.

Figure 4-4. Photomicrographs of chromitites, dunites and surrounding harzburgites from the Luobusa ophiolite (a-h), and the Ray-Iz ophiolite (j-o). (a) Massive UHP chromitite (LA565) from Cr-11 chromitite body from Luobusa. Spinel grain is apparently free of primary hydrous mineral inclusions in contrast to in the Oman discordant chromitite. (b) Olivine-filled fracture in spinel in the diamond-bearing UHP chromitite (Cr-11). (c) Dunite enveloping chromitite (LT69) in the western part of Luobusa ophiolite (Fig. 4-1c). (d) Wavy extinction of olivine in the dunite envelope (LT69). (e) The harzburgite adjacent to chromitite (LT69) in the western part of the Luobusa ophiolite. (f) Ambient clinopyroxene-bearing harzburgite from Tibet. (g) Clinopyroxene-free harzburgite (LA190) distant from the chromitite pod. (h) Tremolite in the ambient harzburgite (LA190) from the Luobusa ophiolite. (i) Massive UHP chromitite from the No.384 body in the Central Deposite of the Ray-Iz ophiolite. (j) Olivine-filled fracture in spinel in the UHP chromitite (No.384 body). (k) Cleavable olivine in the UHP chromitite (No. 384 body). (l) Cleavable olivine in dunite enveloping the UHP chromitite (p.t.214 body). (m) Surrounding harzburgite adjacent to the No.384 UHP chromitite body. Note that the harzburgite typically contains tremolite, chlorite and talc. (n) Cleavable olivine in a surrounding harzburgite in the Central Deposite of the Ray-Iz ophiolite. (o) Magnetite inclusion in olivine from the surrounding harzburgite. (p) Mosaic olivines sometimes showing 120° angle grain boundaries.

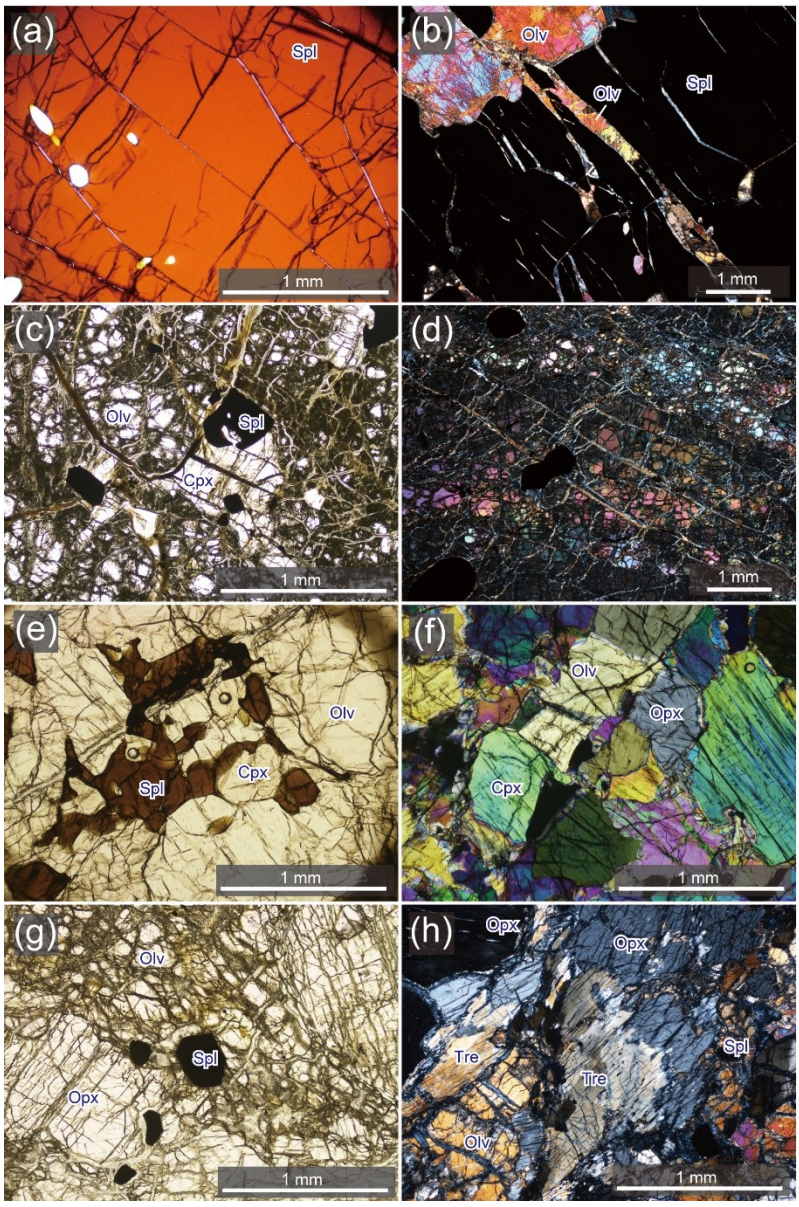
(a)
Spl
1 mm
(b)
Olv
Olv
Spl
1 mm
(c)
Olv
Spl
Cpx
1 mm
(d)
1 mm
(e)
Olv
Cpx
Spl
1 mm
(f)
Olv
Opx
Cpx
1 mm
(g)
Olv
Spl
Opx
1 mm
(h)
Opx
Opx
Spl
Tre
Tre
Olv
1 mm

Figure 4-4a-h.

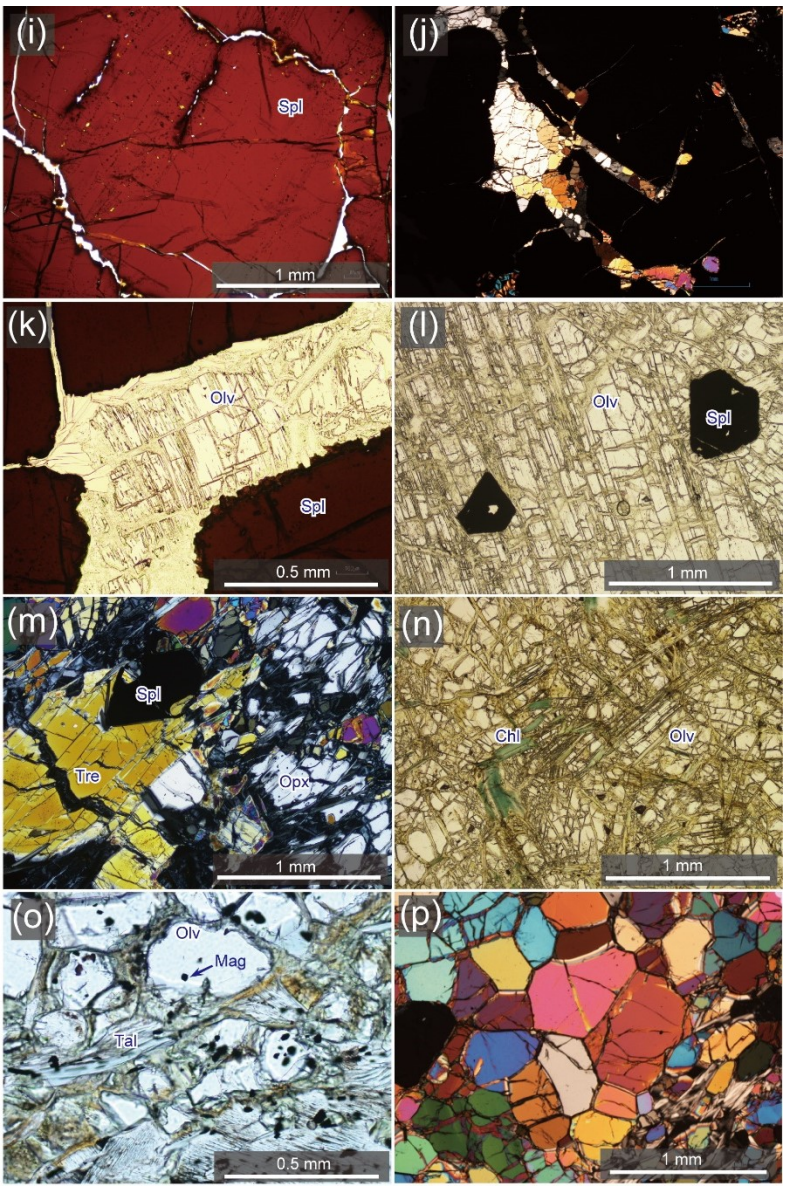
(i)
Spl
1 mm
(j)
(k)
Olv
Spl
0.5 mm
(l)
Olv
Spl
1 mm
(m)
Spl
Tre
Opx
1 mm
(n)
Chl
Olv
1 mm
(o)
Olv
Mag
Tal
0.5 mm
(p)
1 mm

Figure 4-4i-p.

Figure 4-5. Photomicrographs of micro inclusions in chromian spinel from UHP chromitties from the Luobusa (a-d) and Ray-Iz (e-j) ophiolites. (a) Spinel of the chromitite (LA565) from the Cr-11 body in the eastern part of the Luobusa ophiolite. Note that the primary hydrous mineral inclusions, which are common in spinels in the Oman discordant chromitite, are apparently free in spinel from the Luobusa chromitites. Spinel in the Luobusa chromitites typically contain numerous diopside lamellae. (b) Globular inclusions in spinel from coesite lamella-bearing chromitite (LA326) in the Luobusa ophiolite. (c) Trail of solid-phase secondary inclusions in spinel of the UHP chromitite from the Luobusa ophiolite. (d) Secondary fluid inclusions in spinel from the Luobusa chromitite. (e) Spinel in the chromitite from No. 384 body in the central mine of the Ray-Iz ophiolite. Spinels in the Ray-Iz chromitite are similar in characteristics of micro inclusion, such as lack of primary hydrous mineral inclusion and appearance of silicate exsolution lamellae to those in the Luobusa chromitite. (f) Globular silicate inclusions in spinel from No.384 chromitite. (g) Close-up of one of needle-like pyroxene lamellae in spinel. (h) Close-up of one of rod-shaped pyroxene inclusions in spinel of the chromitite from the No.384 pod. (i) Secondary solid inclusions in the Ray-Iz chromitite. The inclusions are composed of chlorite and serpentine. (j) Secondary fluid inclusions in spinel from the Ray-Iz chromitite.

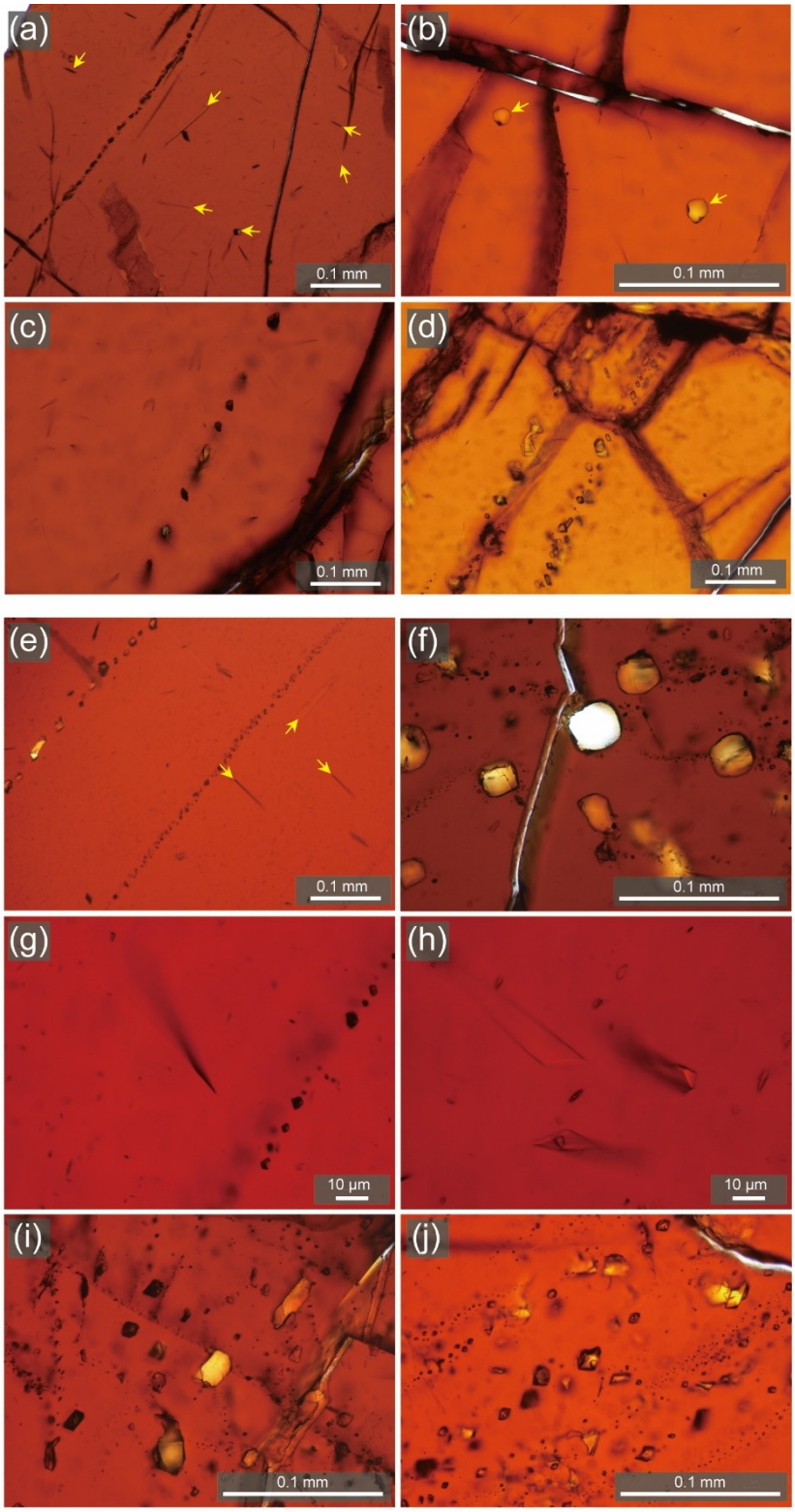
(a)
0.1 mm
(b)
0.1 mm
(c)
0.1 mm
(d)
0.1 mm
(e)
0.1 mm
(f)
0.1 mm
(g)
10 µm
(h)
10 µm
(i)
0.1 mm
(j)
0.1 mm

Figure 4-5.

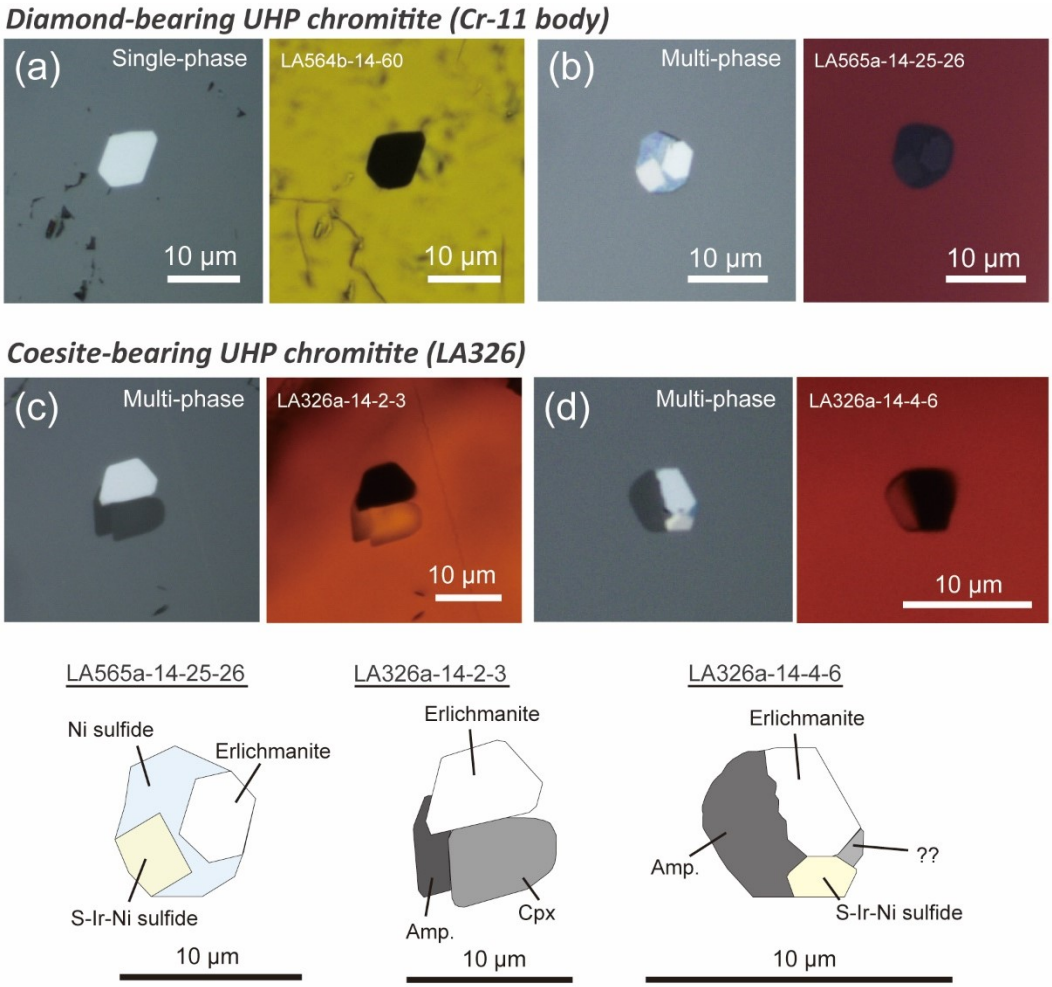

Figure 4-6. Photomicrographs of sulfide mineral inclusions in chromian spinel from the Luobusa ophiolite. Left, reflected light. Right, plane-polarized transmitted light. (a) Euhedral erlichmanite grain in spinel of chromitite (LA565) from the Cr-11 body, showing solitary distribution. (b) Multi-phase sulfide inclusion in spinel from chromitite (LA565). The inclusion is composed of Erlichmanite, Ir-Ni sulfide and Cu sulfide. (c) Multi-phase inclusion, composed of erlichmanite + diopside + pargasite, in spinel of chromitite (LA326), where coesite was found by Yamamoto et al. (2009). (d) Multi-phase inclusion in spinel from LA326 sample consists of erlichmanite, Ir-Ni sulfide and pargasite.

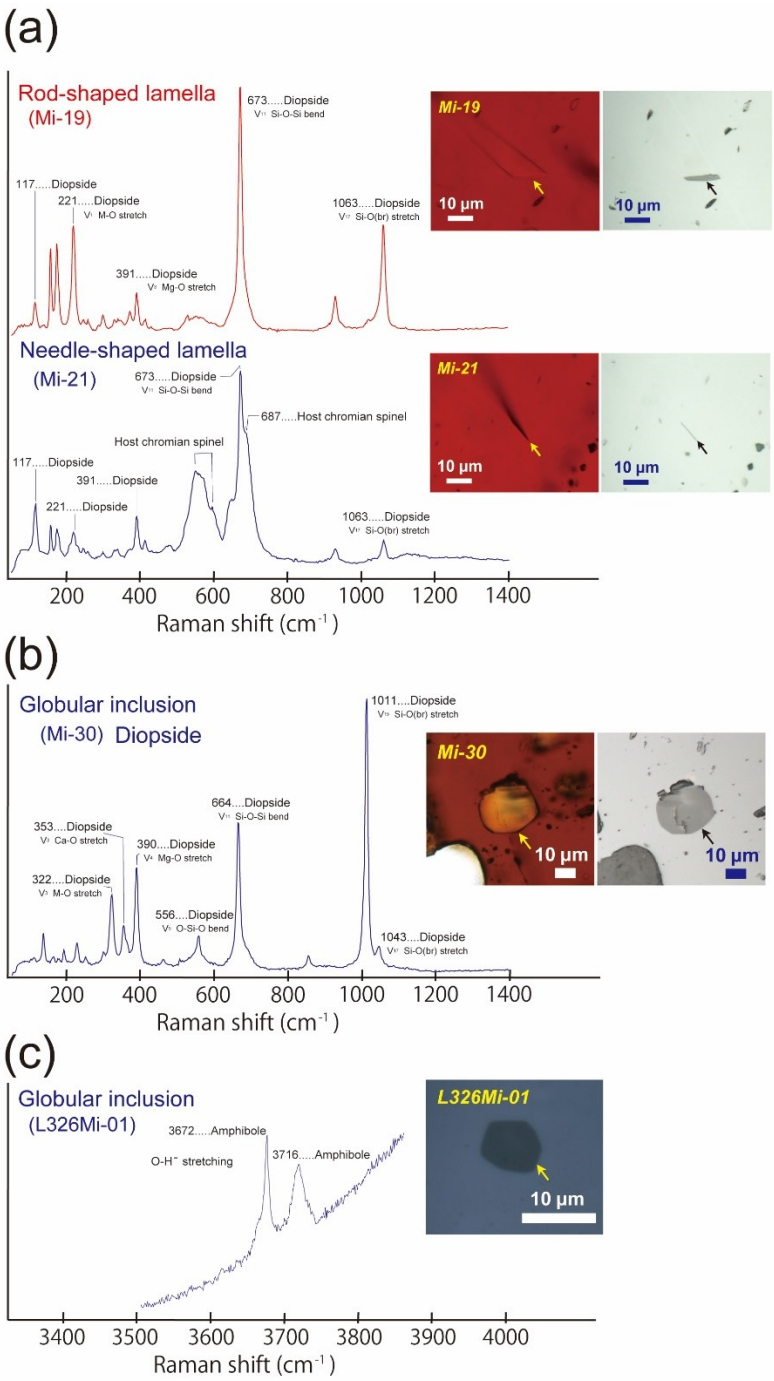

Figure 4-7. Raman spectra of micro inclusions in spinel of chromitites from the Luobusa ophiolite and the Ray-Iz ophiolite. (a) Rod- and needle-shaped exsolution lamellae in spinel from the No.384 chromitite (RY01-01) in the Ray-Iz ophiolite. Their Raman spectra indicate that they mainly consist of diopside. (b) Globular inclusion in chromian spinel from the Ray-Iz chromitite (RY01-01). (c) Amphibole globular inclusion in spinel from coesite-bearing chromitite (LA326) (Yamamoto et al., 2009) in the Luobusa ophiolite.

Figure 4-8. Major-element chemical characteristics of minerals from chromitites, dunites and surrounding harzburgites of the Luobusa and Ray-Iz ophiolites. Abyssal peridotite fields are from Dick and Bullen (1984) and Arai et al. (2011). Forearc peridotite field is from Arai et al. (2011). (a) Relationships between Fo and NiO contents in olivine. (b) Relationships between Fo content of olivine and the Cr# of spinel in harzburgite from the Luobusa and the Ray-Iz ophiolites. OSMA is the olivine-spinel mantle array, a residual spinel peridotite trend as defined by Arai (1994). (c) Trivalent cation ratios of spinel in chromitites and associated rocks. Note that chromitites from the Luobusa and the Ray-Iz ophiolites are similar in spinel chemistry to each other, although surrounding peridotites are not similar. (d) Relationships between Cr# and Mg# of chromian spinel in chromitites and surrounding peridotites. Note that the harzburgites surrounding the Luobusa chromitite are similar to some abyssal peridotites. (e) Relationships between TiO_2 content and Cr# of chromian spinel in chromitites and associated rocks. (f) Relationships between CaO and Al_2O_3 contents of orthopyroxene from harzburgites in the Luobusa and the Ray-Iz ophiolites. Note that orthopyroxenes from the Ray-Iz harzburgite show low CaO and Al_2O_3 contents, indicating a low-T metamorphic feature (e.g., Arai 1974). (g) Relationships between Mg# and Al_2O_3 contents of clinopyroxene from dunite enveloping chromitite and surrounding harzburgites in the Luobusa ophiolite. (h) Relationships between TiO_2 and Na_2O contents of clinopyroxene from dunite and harzburgites in the Luobuca ophiolite. (i) Relationships between Cr# of spinel and Na_2O content of clinopyroxene from dunite and harzburgites in the Luobuca ophiolite.

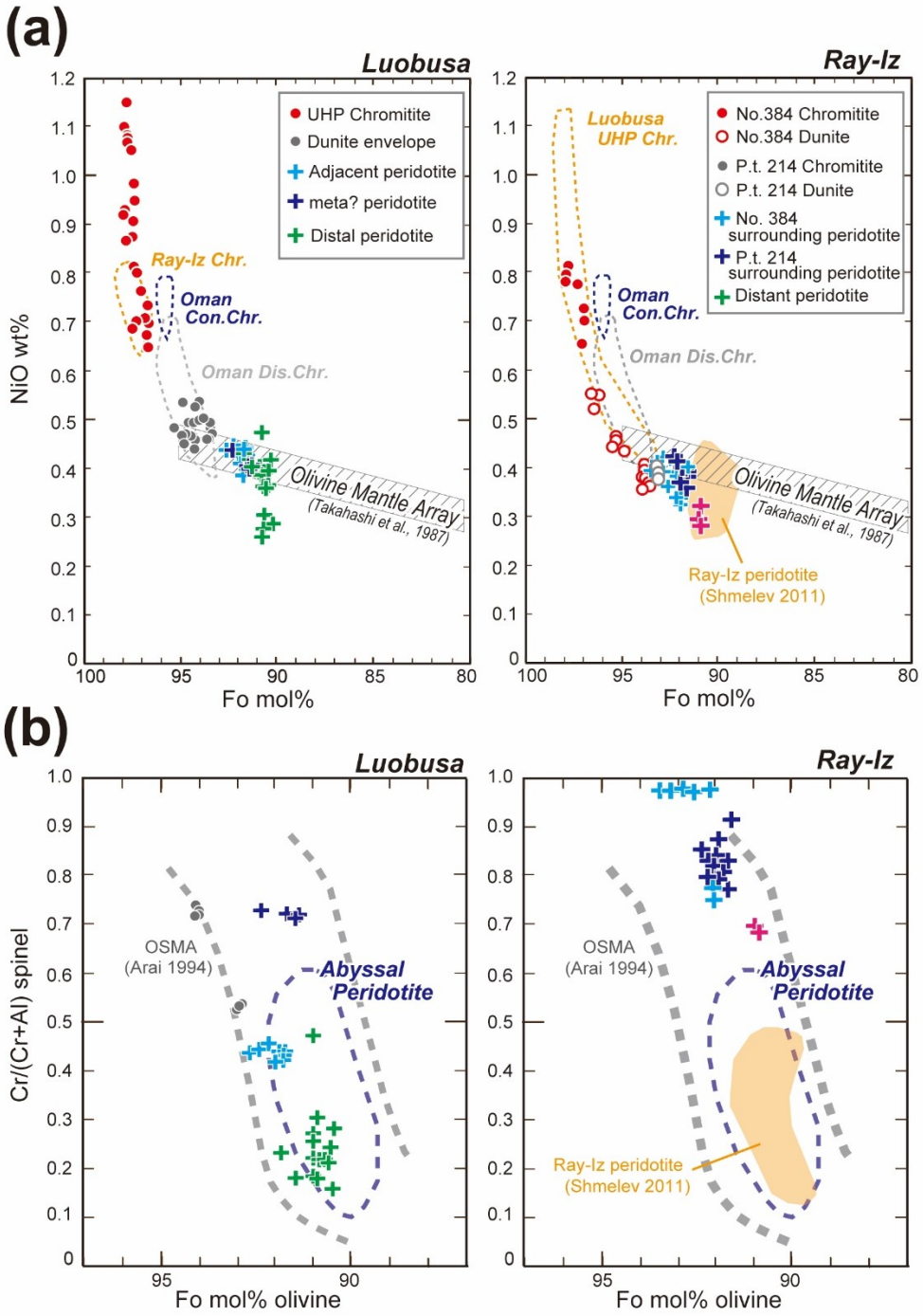
(a)
Luobusa
Ray-Iz
NiO wt%
Fo mol%
UHP Chromitite
Dunite envelope
Adjacent peridotite
meta? peridotite
Distal peridotite
Ray-Iz Chr.
Oman Con.Chr.
Oman Dis.Chr.
Olivine Mantle Array
(Takahashi et al., 1987)
Luobusa UHP Chr.
No.384 Chromitite
No.384 Dunite
P.t. 214 Chromitite
P.t. 214 Dunite
No. 384 surrounding peridotite
P.t. 214 surrounding peridotite
Distant peridotite
Ray-Iz peridotite
(Shmelev 2011)
(b)
Cr/(Cr+Al) spinel
Fo mol% olivine
OSMA
(Arai 1994)
Abyssal Peridotite

Figure 4-8a-b.

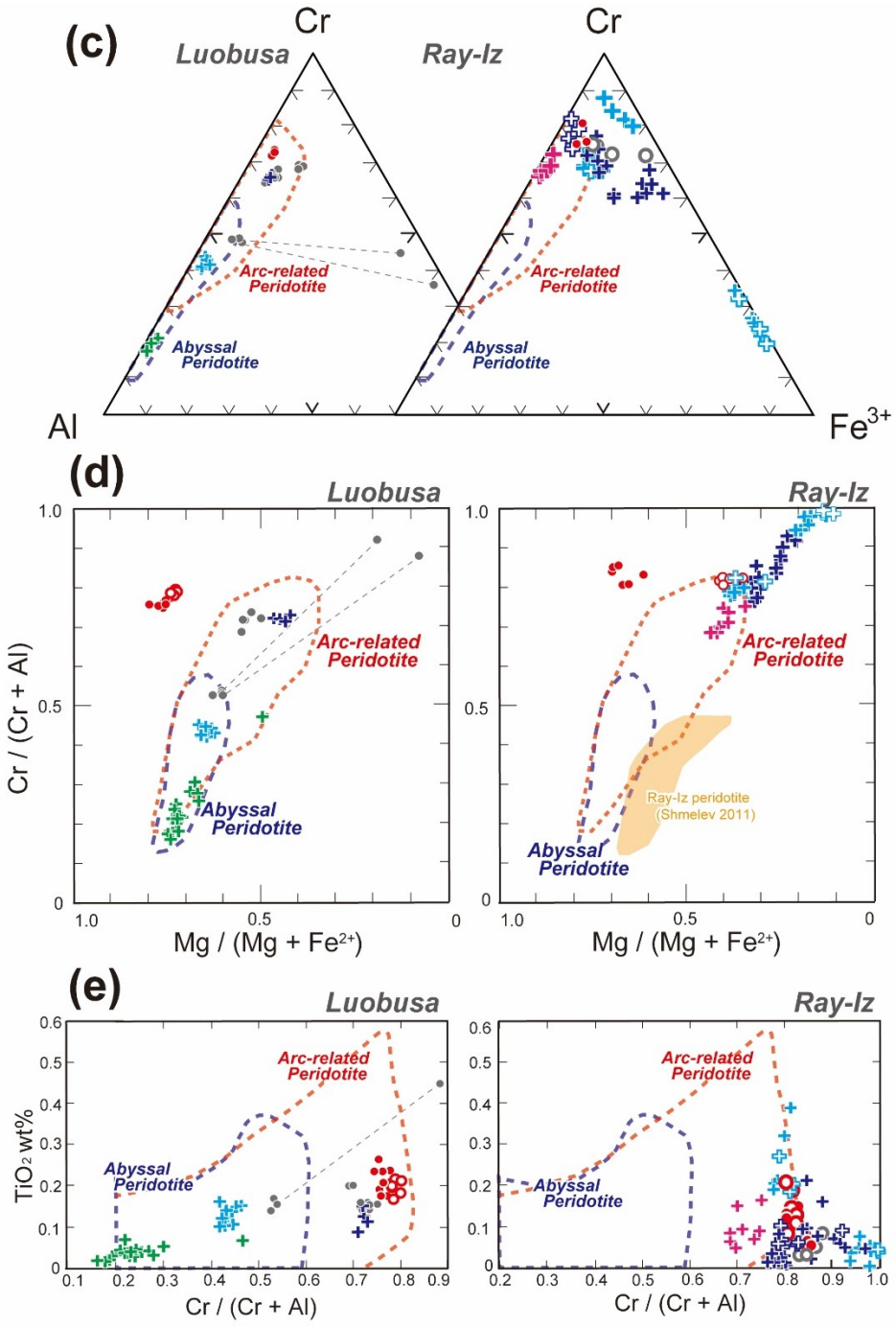
(c)
Luobusa
Ray-Iz
Cr
Cr
Al
Fe3+
Arc-related Peridotite
Abyssal Peridotite
(d)
Luobusa
Ray-Iz
Cr / (Cr + Al)
Mg / (Mg + Fe2+)
Ray-Iz peridotite (Shmelev 2011)
(e)
TiO2 wt%
Cr / (Cr + Al)

Figure 4-8d-e.

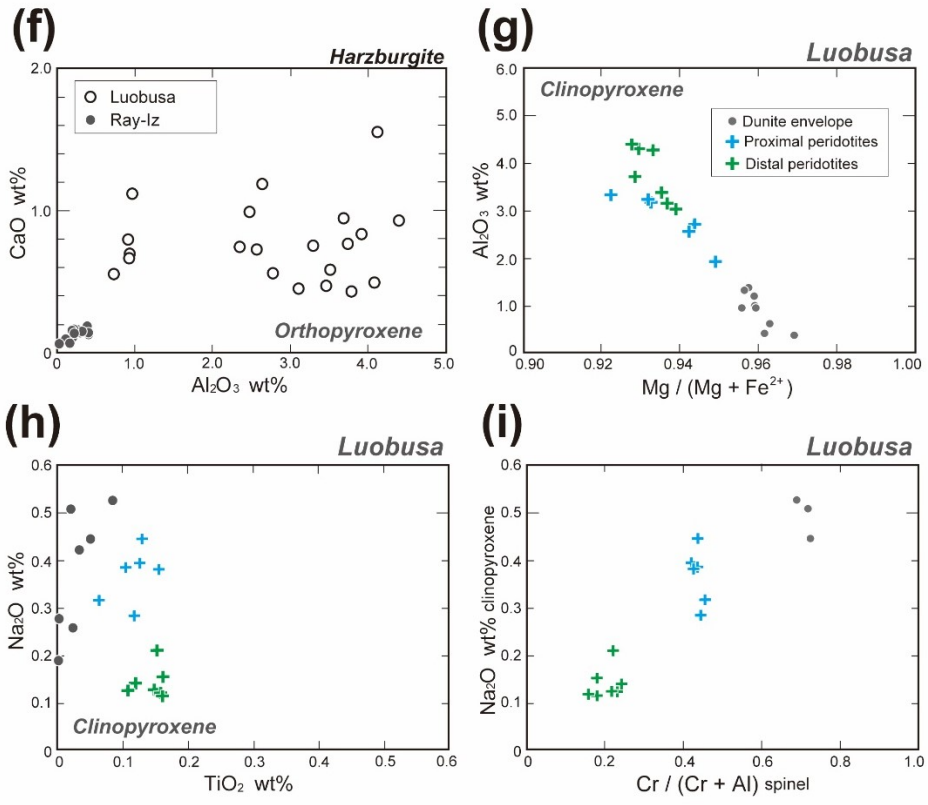
(f)
Harzburgite
Luobusa
Ray-Iz
CaO wt%
Orthopyroxene
Al2O3 wt%
(g)
Luobusa
Clinopyroxene
Dunite envelope
Proximal peridotites
Distal peridotites
Al2O3 wt%
Mg / (Mg + Fe2+)
(h)
Luobusa
Na2O wt%
Clinopyroxene
TiO2 wt%
(i)
Luobusa
Na2O wt% clinopyroxene
Cr / (Cr + Al) spinel

Figure 4-8f-i.

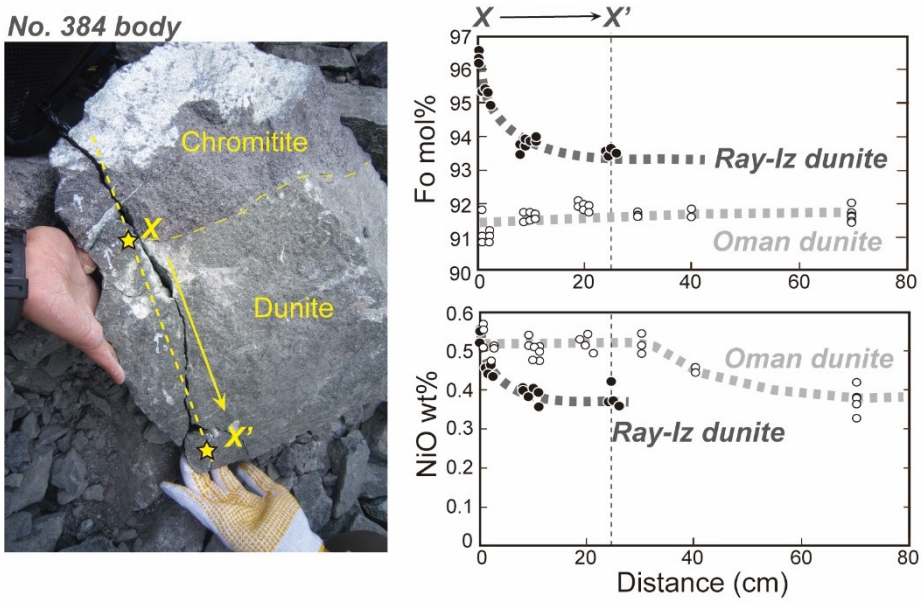

Figure 4-9. Compositional profiles in Fo and NiO contents of olivine in a dunite enveloping chromitite (No.384 body) in the central mine of the Ray-Iz massif. Profiles of dunite envelope around the Hilti concordant chromitite in the Oman ophiolite are shown for comparison. Note that the dunite close (~5 cm) to chromitite shows high Fo and NiO contents in olivine relative to a distant one (~ 20 cm).

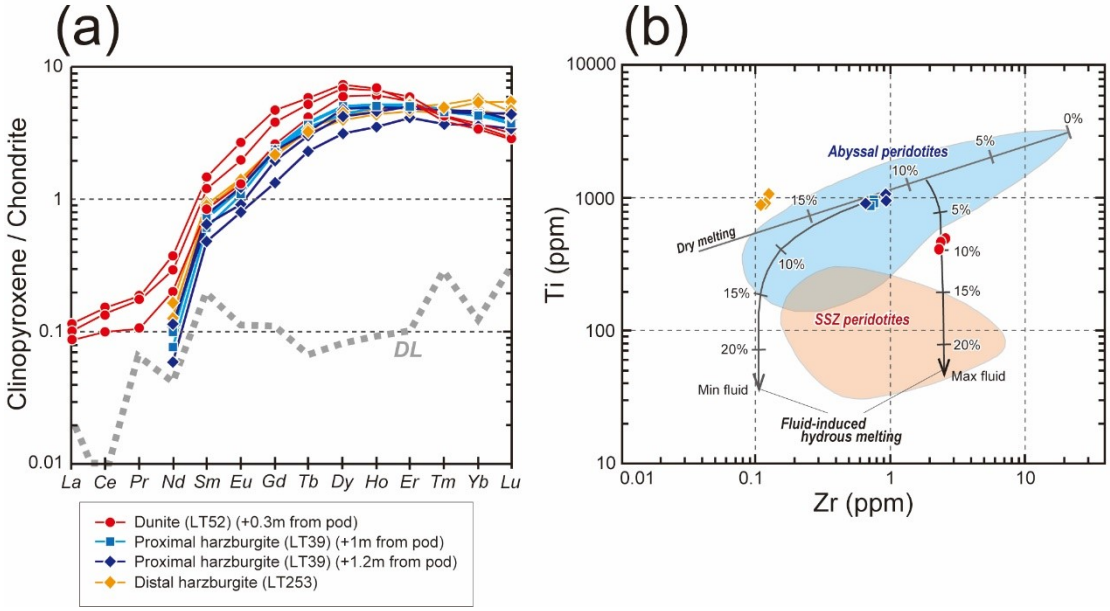

Figure 4-10. Rare earth element (REE) characteristics of clinopyroxenes from dunite envelope and surrounding harzburgite around chromitite (LT69) in the Luobusa ophiolite. (a) Chondrite-normalized REE patterns of clinopyroxenes. Note that clinopyroxne shows a HREE-depleted feature, from Lu to Dy, in the dunite envelope. (b) Relationships between Ti and Zr (in ppm) in clinopyroxene. Melting trends and compositional range of abyssal- and SSZ- peridotites are from Barth et al. (2003).

Figure 4-11. Platinum-group element characteristics of the Luobusa and the Ray-Iz chromitites. (a) Wavelength dispersive X-ray spectra on analyzing crystals TAP, LIF, PETJ from top to bottom, showing the major constituent elements of laurite grains within spinel in the Luobusa UHP chromitite (Cr-11 body). (b) Compositional variation of PGMs in terms of Ru-Os-Ir in the laurite-erlichmanite series. (c) Chondrite-normalized PGE patterns of the Luobusa UHP chromitites. (d) Chondrite-normalized PGE patterns of the Ray-Iz chromitites. (e) Relationships between the total PGE content and the spinel Cr#. Oman MTZ and mantle chromitite fields are from Ahmed and Arai (2002, 2003). (f) Relationships between the total PGE content and the Pd/Ir ratio in chromitites. Note that the Luobusan and the Ray-Iz chromitites show slightly low contents of total PGE and Pd/Ir ratio relative to the Oman discordant chromitites.

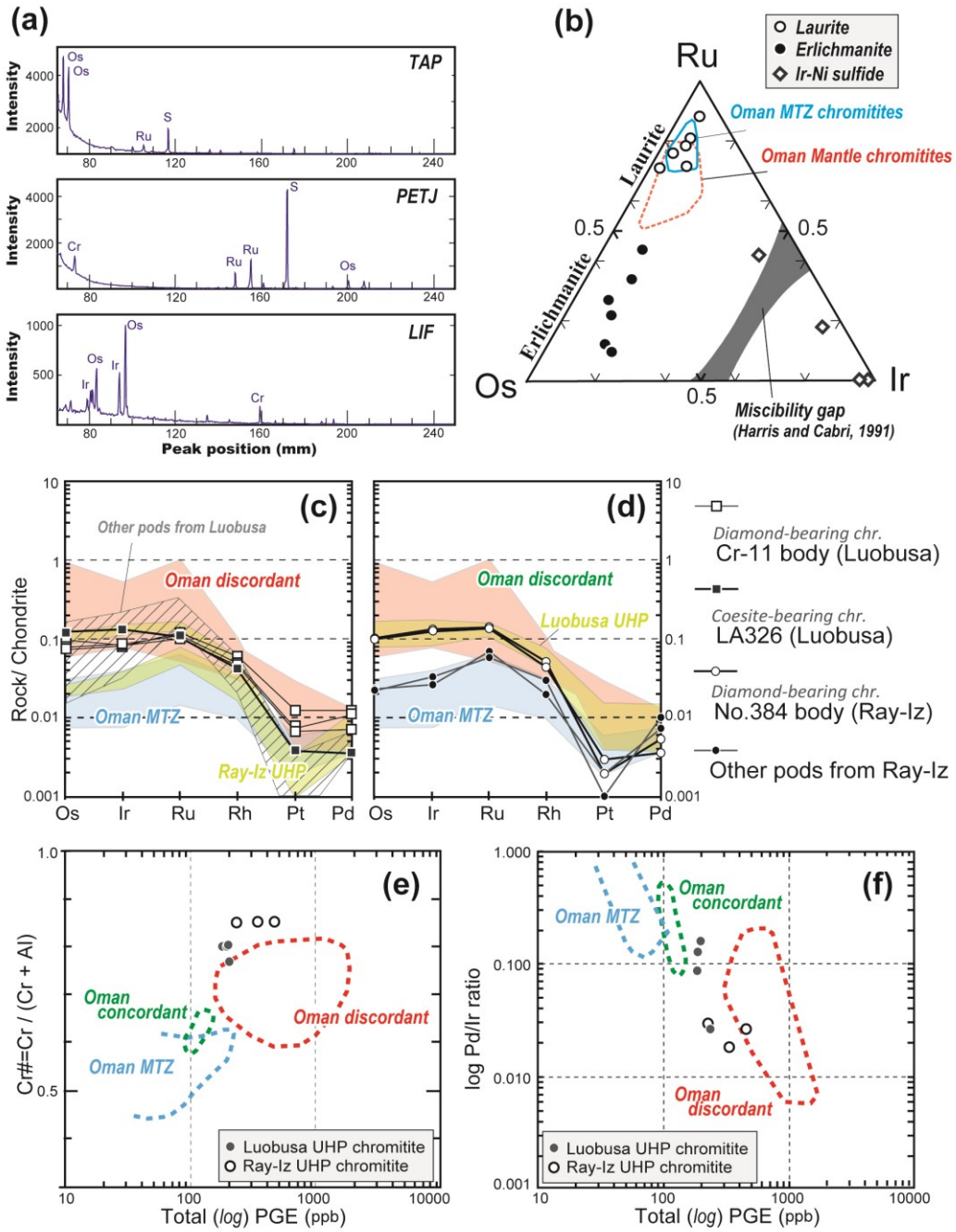
(a)
TAP
PETJ
LIF
Intensity
Peak position (mm)
(b)
Laurite
Erlichmanite
Ir-Ni sulfide
Oman MTZ chromitites
Oman Mantle chromitites
Miscibility gap
(Harris and Cabri, 1991)
(c)
(d)
Other pods from Luobusa
Oman discordant
Oman MTZ
Ray-Iz UHP
Luobusa UHP
Rock/ Chondrite
Diamond-bearing chr.
Cr-11 body (Luobusa)
Coesite-bearing chr.
LA326 (Luobusa)
Diamond-bearing chr.
No.384 body (Ray-Iz)
Other pods from Ray-Iz
(e)
(f)
Oman concordant
Cr#=Cr / (Cr + Al)
log Pd/Ir ratio
Luobusa UHP chromitite
Ray-Iz UHP chromitite
Total (log) PGE (ppb)

Figure 4-11.

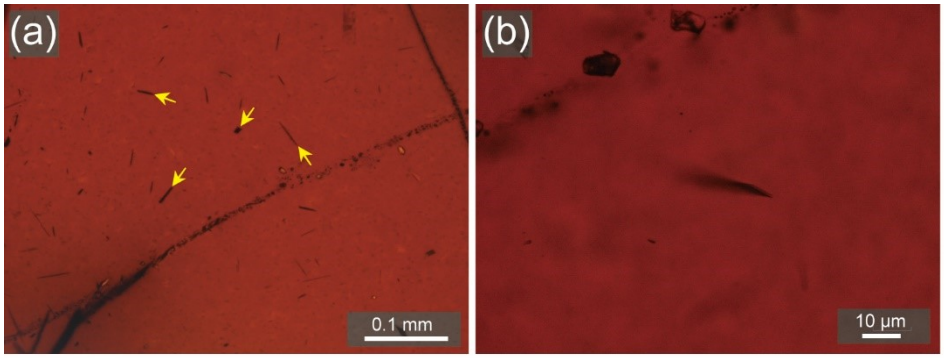

Figure 4-12. Photomicrographs of micro-inclusion in chromian spinel from chromitite in the Higashi-Akaishi ultramafic complex, Japan. (a) Numerous diopside lamellae (arrow) similar to that in the UHP chromitites from the Luobusa and the Ray-Iz ophiolites. Note that the primary hydrous mineral inclusions, such as spinel in the Oman discordant chromitite, are apparently free. (b) Close-up of one of needle-like pyroxene lamellae in spinel.

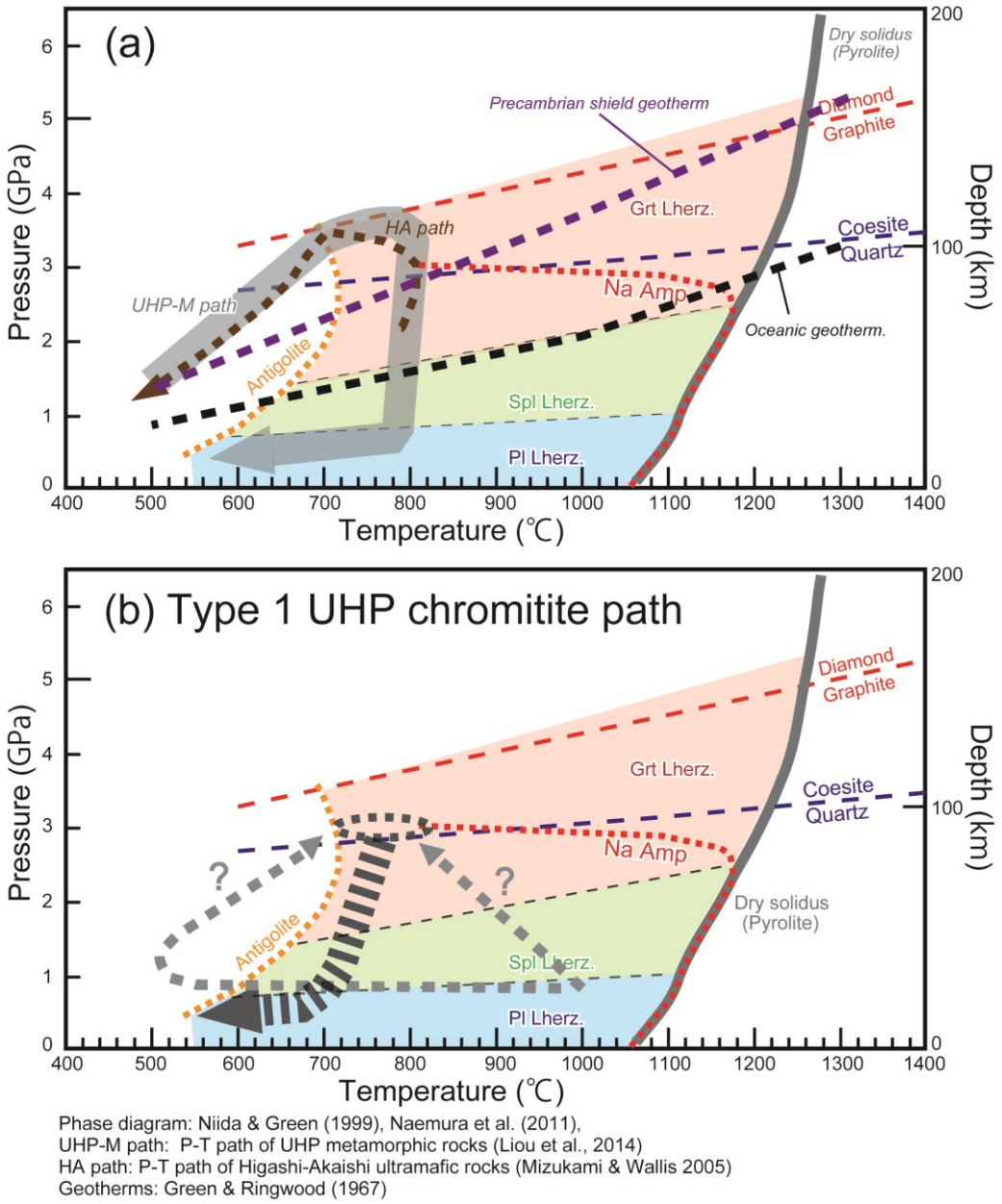

Figure 4-13. Phase diagrams for the stability condition of peridotites and minerals. Modified from Green and Ringwood (1967), Mirward and Massone (1980), Niida and Green (1999), Frost (2006) and Naemura et al. (2011). P-T paths for the UHP metamorphic rocks and the Higashi-Akaishi ultramafic complex are referred from Liou et al. (2014) and Mizukami and Wallis (2005), respectively. (a) Relationships of stability condition of peridotites and minerals in the upper mantle. (b) Possible P-T path of coesite-bearing UHP chromitite in the Luobusa chromitite is shown by grey and black arrows.

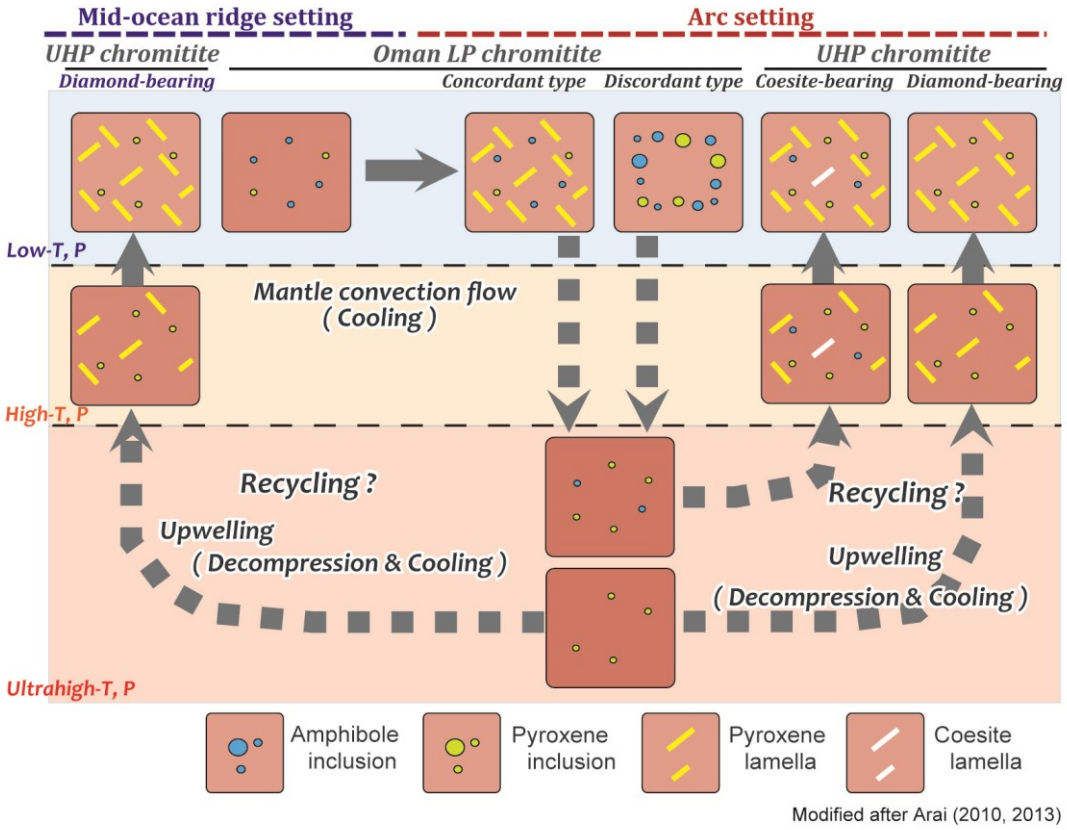

Figure 4-14. Cartoon for genesis of low-pressure and ultrahigh-pressure chromitites.

(a) Sample list of chromitites and surrounding peridotites from the Luobusa and Ray-Iz ophiolites

Sample Name	Rock type	Orebody name & lacation	Texture	Fracture in spl	Mineral species	Lamella	Primary inclusion	Remarks
LA565	chromitite	Cr-11 body, eastern Tibet	Massive to nodular	○	Spl + Olv	Cpx	Cpx + Olv + PGE sulfide	Diamond-bearing chromitite
LA509	chromitite	Cr-11 body, eastern Tibet	Nodular	?	Spl + Olv	Cpx	Cpx + Olv	Diamond-bearing chromitite
LA539	chromitite	Cr-11 body, eastern Tibet	Disseminated	?	Spl + Olv	Cpx	Cpx + Olv + PGE sulfide	Diamond-bearing chromitite
LA492	chromitite	Cr-11 body, eastern Tibet	Nodular	○	Spl + Olv	Cpx	Cpx + Olv	Diamond-bearing chromitite
LA326	chromitite	Central Tibet	Massive	×	Spl + Olv	Cpx + Coe	Cpx + Amp + PGE sulfide	Coesite-bearing chromitite *(Yamamoto et al., 2009)*
LA211	chromitite	No.3 site, Central Tibet	Disseminated	×	Spl + Olv	Cpx	Cpx	-
LT69	chromitite	No.3 site 2, western Tibet	Massive	×	Spl + Olv	Cpx	Cpx + Amp + PGE sulfide	-
LT58	chromitite	No.3 site 2, western Tibet	Massive	×	Spl + Olv	Cpx	Cpx + Amp + PGE sulfide	-
LT52	dunite	No.3 site 2, western Tibet	Porphyroclastic	×	Olv + Spl + Diop	×	Amp + chlorite	Dunite enveloping LT69 pod
LT40	dunite	No.3 site 2, western Tibet	Porphyroclastic	×	Olv + Spl	×	Amp + chlorite	Dunite enveloping LT69 pod
LT39	harzburgite	No.3 site 2, western Tibet	Porphyroclastic	×	Olv + Opx + Cpx + Spl	×	×	Harzburgite surrounding LT69 pod
LT38	harzburgite	No.3 site 2, western Tibet	Porphyroclastic	×	Olv + Opx + Cpx + Spl	×	×	Harzburgite surrounding LT69 pod
LA182	Cpx harzburgite	Central Tibet	Porphyroclastic	×	Olv + Opx + Cpx + Spl	×	×	Ambient harzburgite
LA190	harzburgite	Central Tibet	Porphyroclastic	×	Olv + Opx + Amp+ Spl	×	Amp	Ambient harzburgite
LA258	Cpx harzburgite	Central Tibet	Porphyroclastic	×	Olv + Opx + Cpx + Spl	×	×	Ambient harzburgite
LA246	harzburgite	Central Tibet	Porphyroclastic	×	Olv + Opx + Cpx + Spl	×	×	Ambient harzburgite

(b) Sample list of chromitites and surrounding peridotites from the Ray-Iz ophiolites

Sample Name	Rock type	Orebody name & lacation	Texture	Fracture in spl	Mineral species	Lamella	Primary inclusion	Remarks
RY01-01	chromitite	No.384 body, central Ray-Iz	Massive to disseminated	○	Spl + Olv + Chl	Cpx	Cpx	Diamond-bearing chromitite
RY01-03~7	dunite	No.384 body, central Ray-Iz	Equigranular	×	Olv + Spl + Chl + Trm	×	Ser + Chl	Dunite enveloping No.384 body
RY04-20a	chromitite	Central mine of Ray-Iz	Nodular	○	Spl + Olv + Chl	Cpx	Cpx	-
RY24-1b	chromitite	Central mine of Ray-Iz	Massive	○	Spl + Olv + Chl	Cpx	Cpx	-
RY08-3~4	harzburgite	No.384 body, central Ray-Iz	Porphyroclastic	×	Olv + Opx + Amp + Chl + Tal	×	×	Proximal harzburgite
RY14-1~6	peridotite	No.384 body, central Ray-Iz	Porphyroclastic	×	Olv + Amp + Chl + Tal	×	×	Surrounding peridotite
RY19-5	chromitite	p.t.214 body, western Ray-Iz	Massive	?	Spl + Chl	Cpx	Cpx	Diamond-bearing chromitite
RY19-3	dunite	p.t.214 body, western Ray-Iz	Equigranular	×	Olv + Spl + Chl	×	×	Dunite enveloping p.t.214 body
RY19-1~2	harzburgite	p.t.214 body, western Ray-Iz	Porphyroclastic	×	Olv + Opx + Amp + Tal	×	×	Harzburgite surrounding p.t.214 body

Abbreviations: Minerals Spl = spinal, Olv = olivine, Cpx = clinopyroxene, Opx = orthopyroxene, Amp = amphibole, Chl = chlorite, Tal = talc
Reference: Yamamoto et al. (2009), Xu et al. (2009), Yang et al. (2014)

Table 4-1. A list for samples of UHP chromitites and surrounding peridotites used in this study. Samples from Tibet were corrected by Yamamoto and others in 2001 field expedition.

Location	Luobusa	Luobusa	Luobusa	Luobusa	Luobusa	Luobusa	Luobusa	Luobusa	Luobusa	Luobusa	Luobusa	Luobusa
	No.3 site 2	No.3 site 2	No.3 site 2	No.3 site 2	No.3 site 2	Central	Cr-11 body	Cr-11 body	Cr-11 body			
Rock type	Chr.	Dun.	Dun.	Har.	Har.	Chr.	Chr.	Chr.	Chr.	Har.	C-Har.	C-Har.
Remarks		envelope	envelope	proximal	proximal	C-bearing	D-bearing	D-bearing	D-bearing	ambient	ambient	ambient
Texture	Mas.					Mas.	Nod.	Dis.	Nod.			
Sample	LT69	LT52	LT40	LT39	LT38	LA326	LA509	LA539	LA565	LA190	LA253	LA182
SiO_2	0.01	0.03	0.00	0.01	0.00	0.00	0.00	0.07	0.00	0.00	0.00	0.00
TiO_2	0.24	0.16	0.17	0.10	0.14	0.18	0.16	0.20	0.20	0.11	0.01	0.02
Al_2O_3	12.82	12.58	23.70	32.53	31.54	12.25	10.24	11.04	10.54	12.84	50.52	50.72
Cr_2O_3	58.16	53.26	40.08	35.29	36.52	58.96	61.07	60.25	60.38	51.38	16.58	16.58
FeO*	12.26	22.92	22.87	17.23	17.25	12.45	12.77	13.54	14.03	26.29	14.32	12.66
MnO	0.20	0.37	0.27	0.20	0.24	0.23	0.22	0.28	0.26	0.39	0.13	0.11
MgO	16.47	10.85	13.34	14.82	15.03	16.26	16.31	15.43	15.06	8.70	17.86	18.54
CaO	0.01	0.02	0.00	0.00	0.00	0.00	0.00	0.04	0.00	0.03	0.00	0.00
Na_2O	0.02	0.00	0.01	0.01	0.01	0.01	0.00	0.01	0.00	0.02	0.00	0.00
K_2O	0.00	0.00	0.00	0.00	0.00	0.00	0.00	0.01	0.00	0.00	0.00	0.00
NiO	0.15	0.07	0.16	0.11	0.12	0.15	0.09	0.11	0.13	0.07	0.24	0.25
Total	100.34	100.24	100.60	100.30	100.85	100.48	100.86	100.96	100.60	99.82	99.65	98.87
Mg#	0.76	0.52	0.60	0.64	0.65	0.76	0.76	0.72	0.71	0.43	0.72	0.75
Cr#	0.75	0.74	0.53	0.42	0.44	0.76	0.80	0.79	0.79	0.73	0.18	0.18
$Cr/(Cr+Al+Fe^{3+})$	0.721	0.686	0.483	0.408	0.422	0.732	0.761	0.756	0.761	0.673	0.177	0.177
$Al/(Cr+Al+Fe^{3+})$	0.237	0.241	0.425	0.561	0.543	0.227	0.190	0.208	0.198	0.251	0.803	0.807
$Fe^{3+}/(Cr+Al+Fe^{3+})$	0.042	0.073	0.092	0.032	0.035	0.041	0.049	0.036	0.041	0.077	0.020	0.016

Abbreviations: Chr = chromitite, Dun = dunite, Har = harzburgite, C-Har = clinopyroxene-bearing harzburgite
Mas = massive, Nod = nodular, Dis = disseminated

Table 4-2. Continued

Location	Ray-Iz	Ray-Iz	Ray-Iz	Ray-Iz	Ray-Iz	Ray-Iz	Ray-Iz	Ray-Iz	Ray-Iz	Ray-Iz	Ray-Iz	Ray-Iz	Ray-Iz
	No.384	No.384	No.384	No.384	No.384	No.384	No.384	No.384		p.t.214	p.t.214	p.t.214	p.t.214
Rock type	Chr.	Dun.	Dun.	Dun.	Har.	Har.	Har.	Har.	Har.	Chr.	Dun.	Har.	Har.
Remarks		Contact	+10cm	+25cm		grain	inclusion	ambient	ambient		envelope	proximal	inclusion
Texture	Mas.												
Sample	RY01-1	RY01-3	RY01-5	RY01-7	RY08-4	RY08-3	RY08-3	RY11-3	R35	RY19-5	RY19-3	RY19-1	RY19-1
SiO_2	0.00	0.00	0.00	0.00	0.10	0.02	0.08	0.03	0.07	0.00	0.05	0.02	0.33
TiO_2	0.07	0.21	0.13	0.14	0.20	0.05	0.00	0.01	0.05	0.08	0.05	0.02	0.16
Al_2O_3	7.48	8.54	7.74	8.09	7.91	0.16	0.20	2.56	14.37	7.72	5.53	6.42	4.20
Cr_2O_3	62.49	52.50	53.97	52.57	53.72	17.89	14.30	60.88	52.65	62.47	52.85	56.38	45.03
FeO*	14.36	29.45	29.74	29.95	29.59	72.68	75.14	29.59	24.01	14.23	35.72	29.85	42.46
MnO	0.26	0.43	0.46	0.43	0.41	0.33	0.26	0.58	0.42	0.24	0.54	0.45	0.52
MgO	14.39	7.93	7.65	7.92	7.35	2.45	2.29	3.88	7.96	14.45	5.23	6.18	4.74
CaO	0.00	0.00	0.00	0.00	0.00	0.01	0.00	0.00	0.02	0.00	0.00	0.00	0.00
Na_2O	0.02	0.04	0.03	0.03	0.01	0.00	0.00	0.01	0.01	0.00	0.00	0.00	0.00
K_2O	0.00	0.00	0.00	0.00	0.00	0.00	0.00	0.00	0.00	0.01	0.03	0.02	0.02
NiO	0.09	0.09	0.12	0.10	0.10	0.49	0.69	0.02	0.02	0.08	0.11	0.01	0.23
Total	99.14	99.17	99.83	99.22	99.39	94.07	92.95	97.55	99.59	99.29	100.10	99.35	97.69
Mg#	0.70	0.40	0.39	0.40	0.37	0.14	0.13	0.21	0.39	0.70	0.27	0.32	0.25
Cr#	0.85	0.80	0.82	0.81	0.82	0.99	0.98	0.94	0.71	0.84	0.87	0.85	0.88
$Cr/(Cr+Al+Fe^{3+})$	0.809	0.709	0.728	0.710	0.730	0.269	0.218	0.884	0.690	0.807	0.730	0.775	0.643
$Al/(Cr+Al+Fe^{3+})$	0.144	0.172	0.156	0.163	0.160	0.003	0.005	0.055	0.281	0.149	0.114	0.131	0.089
$Fe^{3+}/(Cr+Al+Fe^{3+})$	0.047	0.119	0.117	0.127	0.110	0.727	0.777	0.061	0.029	0.045	0.157	0.094	0.268

Table 4-2. Selected microprobe analyses of spinels in UHP chromitites and surrounding peridotites from the Luobusa and Ray-Iz ophiolites.

Location	Luobusa	Luobusa	Luobusa	Luobusa	Luobusa	Luobusa	Luobusa	Luobusa	Luobusa	Luobusa
	No.3 site 2	No.3 site 2	No.3 site 2	No.3 site 2	Cr-11 body	Cr-11 body	Cr-11 body			
Rock type	Dun.	Dun.	Har.	Har.	Chr.	Chr.	Chr.	Har.	C-Har.	C-Har.
Remarks	envelope	envelope	proximal	proximal	Nod.	Dis.	Nod.			
Texture					Nod.	Dis.	Nod.			
Sample	LT52	LT40	LT39	LT38	LA509	LA539	LA565	LA190	LA253	LA182
SiO_2	41.56	42.10	42.03	41.68	42.31	42.01	41.55	41.62	41.87	41.84
TiO_2	0.00	0.01	0.00	0.00	0.00	0.00	0.01	0.00	0.02	0.00
Al_2O_3	0.00	0.00	0.00	0.01	0.00	0.00	0.00	0.00	0.00	0.00
Cr_2O_3	0.00	0.01	0.00	0.00	0.00	0.00	0.30	0.00	0.00	0.00
FeO*	6.08	7.12	8.02	8.26	2.42	3.98	2.03	8.47	9.67	9.04
MnO	0.11	0.13	0.12	0.16	0.03	0.05	0.03	0.14	0.13	0.09
MgO	53.00	52.24	51.43	51.15	56.00	54.28	55.69	51.43	51.19	51.01
CaO	0.05	0.01	0.04	0.01	0.00	0.11	0.00	0.01	0.02	0.02
Na_2O	0.00	0.00	0.00	0.00	0.00	0.00	0.00	0.00	0.00	0.00
K_2O	0.00	0.00	0.00	0.00	0.00	0.01	0.00	0.00	0.00	0.00
NiO	0.47	0.41	0.41	0.40	1.06	0.63	1.10	0.40	0.42	0.40
Total	101.27	102.03	102.04	101.66	101.81	101.06	100.72	102.06	103.32	102.40
Fo	93.9561	92.8917	91.9503	91.6894	97.634	96.0484	97.9924	91.5398	90.4116	90.95

Location	Ray-Iz	Ray-Iz	Ray-Iz	Ray-Iz	Ray-Iz	Ray-Iz	Ray-Iz	Ray-Iz	Ray-Iz	Ray-Iz	Ray-Iz
	No.384	No.384	No.384	No.384	No.384	No.384	No.384		p.t.214	p.t.214	p.t.214
Rock type	Chr.	Dun.	Dun.	Dun.	Har.	Har.	Har.	Har.	Dun.	Har.	Har.
Remarks		Contact	+10cm	+25cm	proximal	proximal	ambient	ambient	envelope	proximal	proximal
Texture	Mas.										
Sample	RY01-1	RY01-3	RY01-5	RY01-7	RY08-4	RY08-3	RY11-3	R35	RY19-3	RY19-1	RY19-2
SiO_2	42.33	42.12	41.03	41.96	41.74	41.47	41.10	41.68	42.62	42.00	41.55
TiO_2	0.00	0.00	0.00	0.00	0.00	0.00	0.00	0.00	0.00	0.00	0.00
Al_2O_3	0.00	0.00	0.00	0.00	0.00	0.00	0.00	0.00	0.00	0.00	0.00
Cr_2O_3	0.11	0.00	0.00	0.00	0.00	0.00	0.00	0.00	0.00	0.00	0.00
FeO*	2.09	3.81	6.48	6.47	7.90	8.16	8.32	8.86	7.07	7.87	8.30
MnO	0.02	0.03	0.11	0.10	0.10	0.13	0.11	0.14	0.12	0.16	0.13
MgO	55.33	54.65	51.85	52.65	51.49	50.97	50.17	49.71	53.26	51.30	50.96
CaO	0.00	0.00	0.00	0.00	0.00	0.00	0.01	0.00	0.00	0.01	0.01
Na_2O	0.00	0.00	0.00	0.00	0.00	0.00	0.00	0.00	0.01	0.00	0.02
K_2O	0.00	0.00	0.00	0.00	0.00	0.00	0.00	0.00	0.01	0.00	0.00
NiO	0.79	0.55	0.40	0.37	0.39	0.35	0.35	0.28	0.37	0.37	0.38
Total	100.65	101.17	99.87	101.56	101.63	101.08	100.05	100.66	103.47	101.702	101.36
Fo	97.9278	96.2327	93.4483	93.5485	92.068	91.7532	91.486	90.9088	93.0638	92.0751	91.6215

Table 4-3. Selected microprobe analyses of olivines in UHP chromitites and surrounding peridotites from the Luobusa and Ray-Iz ophiolites.

Location	Luobusa	Luobusa	Luobusa	Luobusa	Luobusa
	No.3 site 2	No.3 site 2	No.3 site 2		
Rock type	Dun.	Har.	Har.	C-Har.	C-Har.
Texture					
Sample	LT52	LT39	LT38	LA253	LA182
SiO_2	56.09	54.46	54.95	53.59	52.61
TiO_2	0.00	0.13	0.12	0.16	0.15
Al_2O_3	0.44	3.18	1.94	3.39	4.39
Cr_2O_3	0.08	1.19	0.68	0.74	0.94
FeO*	1.25	2.42	1.67	2.07	2.28
MnO	0.04	0.08	0.06	0.06	0.08
MgO	17.60	18.78	17.49	16.85	16.51
CaO	25.52	21.43	24.66	24.15	23.69
Na_2O	0.28	0.40	0.28	0.11	0.21
K_2O	0.01	0.00	0.01	0.01	0.00
NiO	0.04	0.03	0.05	0.01	0.04
Total	101.34	102.09	101.92	101.15	100.89
Mg#	0.96	0.93	0.95	0.94	0.93

Abbreviations:
un = dunite, Har = harzburgite, C-Har = clinopyroxene-bearing harzburg

Table 4-4. Selected microprobe analyses of clinopyroxenes in dunite and harzburgite from the Luobusa ophiolite.

Location	Luobusa	Luobusa	Luobusa	Luobusa	Luobusa	Ray-Iz	Ray-Iz	Ray-Iz	Ray-Iz
	No.3 site 2	No.3 site 2				No.384 body			
Rock type	Har.	Har.	Har.	C-Har.	C-Har.	Har.	Har.	Har.	Har.
Remarks	proximal	proximal	ambient	ambient	ambient	proximal	ambient	proximal	proximal
Sample	LT39	LT38	LA190	LA253	LA182	RY08-4	R35	RY19-1	RY19-2
SiO_2	57.60	57.23	58.79	55.89	55.98	59.01	58.69	59.44	59.28
TiO_2	0.06	0.06	0.03	0.05	0.05	0.00	0.00	0.00	0.00
Al_2O_3	2.78	2.57	0.97	3.68	3.79	0.17	0.40	0.26	0.31
Cr_2O_3	0.73	0.56	0.37	0.56	0.50	0.02	0.10	0.01	0.04
FeO*	5.43	5.37	5.42	6.00	6.04	5.42	6.16	5.41	5.67
MnO	0.11	0.12	0.12	0.13	0.16	0.09	0.13	0.16	0.16
MgO	35.00	34.87	35.20	33.65	33.71	36.56	34.97	36.97	36.26
CaO	0.56	0.73	1.12	0.95	0.43	0.12	0.14	0.16	0.15
Na_2O	0.01	0.00	0.01	0.02	0.00	0.00	0.00	0.00	0.00
K_2O	0.00	0.00	0.00	0.01	0.00	0.01	0.00	0.04	0.00
NiO	0.09	0.10	0.08	0.09	0.09	0.08	0.05	0.08	0.08
Total	102.36	101.60	102.10	101.02	100.75	101.48	100.65	102.53	101.93
Mg#	0.92	0.92	0.92	0.91	0.91	0.92	0.91	0.92	0.92

Abbreviations: Har = harzburgite, C-Har = clinopyroxene-bearing harzburgite

Table 4-5. Selected microprobe analyses of orthopyroxenes in harzburgite from the Luobusa and Ray-Iz ophiolites.

Location	western Tibet No.3 site 2 orebody						Luobusa	Luobusa
Rock type	Dun.	Dun.	Har.	Har.	Har.	Har.	C-Har.	C-Har.
Remarks	envelope	envelope	proximal	proximal	proximal	proximal		
Sample	LT52a	LT52b	LT39a	LT39b	LT38a	LT38b	LA253	LA253
Nb	0.053	0.053	0.054	0.033	0.060	0.033	0.032	0.034
La	0.024	0.020	-	-	-	-	-	-
Ce	0.084	0.061	0.006	0.005	0.005	-	-	-
Sr	2.889	2.093	0.434	0.338	0.374	0.383	0.143	0.161
Pr	0.016	0.010	-	-	-	-	-	-
Nd	0.137	0.093	0.050	0.055	0.063	0.029	0.063	0.057
Zr	2.412	2.282	0.692	0.754	0.921	0.652	0.112	0.124
Sm	0.184	0.131	0.119	0.112	0.119	0.081	0.141	0.136
Eu	0.116	0.077	0.075	0.079	0.078	0.049	0.079	0.080
Gd	0.771	0.541	0.531	0.499	0.524	0.289	0.469	0.444
Ti	465.915	411.867	922.992	955.414	977.733	910.876	897.549	1049.082
Tb	0.199	0.157	0.137	0.137	0.131	0.091	0.115	0.127
Dy	1.747	1.538	1.209	1.273	1.282	0.831	1.080	1.075
Y	9.273	8.734	7.434	7.484	7.623	5.945	6.453	7.062
Ho	0.378	0.342	0.287	0.299	0.294	0.205	0.266	0.278
Er	0.981	0.914	0.887	0.879	0.898	0.706	0.758	0.842
Tm	0.108	0.100	0.125	0.121	0.125	0.101	0.120	0.124
Yb	0.639	0.585	0.787	0.762	0.819	0.649	0.751	0.929
Lu	0.079	0.072	0.102	0.097	0.106	0.090	0.110	0.114

Table 4-6. Selected trace-element analyses of clinopyroxenes in dunite and harzburgite from the Luobusa ophiolites. -: not detected.

Location	Central	Central	Central	Cr-11	Cr-11	Cr-11	Cr-11	Western	Western
	C-bearing	C-bearing	C-bearing	D-bearing	D-bearing	D-bearing	D-bearing		
Texture	Mas.	Mas.	Mas.	Nod.	Nod.	Nod.	Nod.	Mas.	Mas.
Sample	LA326	LA326	LA326	LA565	LA565	LA565	LA565	LT69	LT69
Mineral name	Erl.	Lau.	Ir-Ni S.	Erl.	Erl.	Lau.	Ir-Ni S.	Lau.	Lau.
S	25.12	33.17	24.50	26.67	28.78	32.22	23.51	34.90	32.73
Os	46.92	15.52	2.15	44.96	34.43	12.52	0.69	11.95	23.17
Ir	13.26	8.99	42.69	7.26	8.80	5.52	29.14	6.41	2.43
Ru	3.48	32.74	0.00	10.31	17.87	34.63	0.00	41.45	33.31
Rh	0.54	1.69	0.77	0.56	1.15	2.00	4.01	1.80	1.63
Pt	0.72	0.48	0.30	0.74	0.47	0.77	0.63	0.41	0.96
Pd	0.29	1.59	0.13	0.45	0.98	1.67	1.23	1.84	1.50
Ni	0.00	0.45	12.96	0.00	0.00	0.06	12.32	0.06	0.03
Cu	0.10	0.67	6.96	0.03	1.04	0.11	7.93	0.08	0.03
Fe	0.56	0.81	5.28	0.55	0.60	1.17	8.48	0.38	0.30
Cr	1.68	2.91	2.05	2.18	2.27	4.87	7.92	1.59	1.83
Total	92.67	99.03	97.79	93.70	96.38	95.53	95.86	100.87	97.91
Atomic %									
S	77.706	67.128	55.033	68.053	66.925	67.716	54.689	66.611	67.241
Os	15.016	5.296	0.815	19.347	13.496	4.435	0.270	3.845	8.026
Ir	4.198	3.034	16.002	3.093	3.416	1.935	11.314	2.043	0.833
Ru	2.092	21.013	0.000	8.348	13.183	23.089	0.000	25.101	21.708
Rh	0.318	1.067	0.541	0.445	0.830	1.313	2.911	1.071	1.044
Pt	0.224	0.161	0.112	0.309	0.178	0.267	0.240	0.129	0.325
Pd	0.168	0.972	0.089	0.342	0.690	1.058	0.860	1.061	0.928
Ni	0.000	0.498	15.909	0.000	0.000	0.064	15.669	0.067	0.031
Cu	0.100	0.682	7.895	0.033	1.218	0.111	9.311	0.073	0.030
Fe*	0.178	0.148	3.605	0.030	0.064	0.011	4.736	0.001	0.000
Ru/(Ru+Os+Ir)	0.098	0.716	0.000	0.271	0.784	0.438	0.000	0.810	0.710
Os/(Ru+Os+Ir)	0.705	0.181	0.048	0.628	0.151	0.448	0.023	0.124	0.263
Ir/(Ru+Os+Ir)	0.197	0.103	0.952	0.100	0.066	0.113	0.977	0.066	0.027

Abbreviations: C-bearing, coesite-bearing UHP chromitite; D-bearing, diamond-bearing UHP chromitite
Mas, massive; Nod, nodular; Erl, erlichmanite; Lau, laurite; Ir-Ni S, Ir-Ni sulfide
Fe*: Amount of Fe corrected for the chromian spinel matrix effect.

Table 4-7. Selected microprobe analyses of PGMs in chromitites from the Luobusa ophiolites.

Location	Remarks	Texture	Sample	Os	Ir	Ru	Rh	Pt	Pd	Total	Pd/Ir	Ru/Pt
Luobusa, central	Coesite-bearing sample	Massive	LA326	66	74	78	9	4	2	233	0.03	19.50
Luobusa, central	No.3 site sample	Disseminated	LA211	122	108	70	10	2	4	316	0.04	35.00
Luobusa, eastern	Cr-11 orebody, Diamond-bearing	Nodular	LA482	8	9	27	5	3	4	56	0.44	9.00
Luobusa, eastern	Cr-11 orebody, Diamond-bearing	Nodular	LA509	41	46	74	10	8	6	185	0.13	9.25
Luobusa, eastern	Cr-11 orebody, Diamond-bearing	Disseminated	LA539	48	45	70	9	7	4	183	0.09	10.00
Luobusa, eastern	Cr-11 orebody, Diamond-bearing	Nodular	LA564	37	43	81	12	13	7	193	0.16	6.23
Luobusa, western	No.3 site 1 orebody sample	Massive	LT16	186	184	97	11	5	4	487	0.02	19.40
Ray-Iz, central	sample from Central mine (No.384)	Massive	R-30	51	66	92	9	3	2	223	0.03	30.67
Ray-Iz, central	sample from Central mine (No.384)	Massive	R-31	151	148	126	11	10	4	450	0.03	12.60
Ray-Iz, central	sample from Central mine (No.384)	Massive	R-33	94	107	114	10	3	2	330	0.02	38.00
Ray-Iz	sample frm other mine	Massive	R-27	12	14	48	4	2	4	84	0.29	24.00
Ray-Iz	sample frm other mine	Disseminated	R-36	12	18	41	6	1	5	83	0.28	41.00

Table 4-8. Whole-rock analyses of bulk-rock platinum-group element compositions (ppb) in the chromitites from the Luobusa and Ray-Iz ophiolites.

Chapter 5: Conclusions, acknowledgements and references.

5.1: Conclusion

5.1.1: *The genesis of podiform chromitites from the northern Oman ophiolite*

Discordant chromitite pods in the mantle section along Wadi Hilti, Rajmi and Fizh, have some arc-related features. Numerous inclusions of primary hydrous mineral, e.g., pargasite and Na phlogopite, in spinel from discordant pods suggest that hydrous magma was involved in formation of chromitites. Chromian spinels from discordant pods and dunites are characterized by high Cr#s and low Ti contents, an arc-related feature. Harzburgite adjacent to discordant pods also shows high-depletion of magmatic components, i.e. high-Cr#s and low-Ti contents of spinel and low-HREE contents in clinopyroxene. Trace element characteristics of clinopyroxenes in dunite enveloping Hilti and Fizh discordant pods suggest that high-Mg andesitic, such as boninitic, melts were involved in their formation. Such arc-related magma were probably generated by flux melting of depleted harzburgite, based on LREE enrichment in spinel and clinopyroxene from the harzburgites adjacent to discordant pods. In the case of the harzburgite surrounding the discordant pod along Wadi Hilti, we can see the transition from sub-arc mantle to sub-oceanic mantle peridotite within several meters, in terms of spinel chemistry and clinopyroxene trace-element chemistry. These observations from the surrounding peridotites of Hilti discordant pod suggest that the melt/harzburgite reaction plays an important role in the evolution or formation of boninitic magma and chromitite in the sub-arc uppermost mantle.

Concordant pods along Wadi Hilti and Rajmi are distinctly different from discordant pods in mineral chemistry and in micro-inclusions in spinel. Spinels from concordant pods and surrounding peridotites show low Cr#s, around 0.5 to 0.65, possibly showing a sub-oceanic feature. They contain primary hydrous mineral inclusions as in discordant pods, although they are far less abundant and smaller in size than in discordant pods. Numerous pyroxene lamellae are typically available only from concordant pods. In addition, olivines in the dunite enveloping a concordant pod along Wadi Hilti, are extraordinarily high in Ni contents, suggesting Ni diffusion from the chromitite. Exsolution of silicate lamellae in spinel and subsolidus Ni diffusion in olivine from dunite envelope were probably due to longer duration of subsolidus

cooling.

Coexistence of the two contrasted types of chromitites in the Oman ophiolite reflects the switch of tectonic setting from oceanic mantle to sub-arc mantle. The involved melt was clearly different between the two types of chromitite. Concordant chromitite and surrounding peridotites have a sub-oceanic affinity, and discordant pods and surrounding rocks show an arc-related feature. Concordant chromitite pods have probably experienced longer duration of subsolidus cooling, which facilitated the exsolution of silicate lamellae in spinel and Ni diffusion in olivine from dunite envelope. The longer duration of cooling was due to transportation and deformation of the pod by horizontal mantle flow after chromitite formation at a spreading ridge. Discordant chromitites, dunites and surrounding highly depleted harzburgites were probably formed by arc-related magmatism at the supra-subduction zone environment before ophiolite obduction. In addition, concordant and discordant chromitites are of low-P origin because of the existence of primary amphibole mineral inclusion in spinel and the lack of UHP minerals.

5.1.2: *The Takashima chromitite xenoliths and their implications*

The Takashima chromitites are characterized by various textures, e.g., massive, layered, anti-nodular and nodular. Chromian spinels from the chromitite and dunite xenoliths show high Cr#s and low TiO_2 contents, indicating an arc-related feature. Laurites, one of typical PGMs in ophiolitic chromitite, were found as minute (up to 5 μm diameter) soliary grains of euhedral to subhedral shape in spinel from the chromitites. Chemical characteristics of laurite grains in the Takashima chromitites are analogous to those in ophiolitic chromitites. Silicate inclusions, showing a concentric distribution in spinel, are mainly composed of pyroxenes and olivine. Hydrous minerals, such as pargasite and Na phlogopite, are not found from the Takashima chromitites. The chondrite-normalized PGE patterns of the Takashima chromitite xenoliths show slightly negative slopes from Ru to Pt, and low Pd/Ir ratios (0.08 to 0.25), similar to those of typical ophiolitic chromitites. The Takashima chromitites are quite similar in their textural variations, spinel chemistry and PGE chemistry to some of discordant chromitite pods from the northern Oman ophiolite, indicating a sub-arc

origin for the latter.

The Takashima chromitites possibly occur in a thick MTZ, beneath Takashima because of their PGE chemical characteristics and the lack of associated mantle harzburgite xenoliths. Some of ophiolitic chromitites, showing similar characteristics to the Takashima chromitite xenoliths, probably are of sub-arc origin. Charactersitics of the Takashima chromitites indicate an origin of ophiolitic chromitites and a tectonic setting for host ophiolite formation.

5.1.3: *The origin of UHP chromitites from Luobusa and Ray-Iz ophiolites*

UHP chromitites from the two ophiolites are similar in some ways to each other. They are mostly concordant to the foliation of surrounding peridotite, suggesting that they have experienced deformation via mantle convection flow. As the evidence supportive of deformation at high-T condition, spinels from both UHP chromitites are sometimes cut by olivine-filled fracture. Spinels from the two UHP chromitites show high Cr#s (around 0.8 to 0.85) and low TiO_2 contents (up to 0.2 wt%), indicating their arc-related feature. Olivines in the two UHP chromitites are sometimes characterized by extraordinarily high Mg (Mg#= around 0.98) and Ni contents (up to 1.2 wt%), suggesting long duration of subsolidus cooling. This is consistent with the existence of numerous silicate lamellae in spinels. Silicate lamellae in spinel from UHP chromitites mainly consist of diopside. UHP chromitites from both the ophiolites are divided into two types in terms of mineral species as inclusion in spinel. One is characterized by coexistence of coesite lamella and primary Na amphibole inclusion in spinels. The other is free of primary Na amphibole inclusion. Coexistence of coesite and Na amphibole in the former spinel indicates their experience of relatively low-T (around 700 to 800 °C) and high-P (around 3 GPa) conditions. If we consider geotherms of the upper mantle, the former can be formed by UHP metamorphism in a subduction zone environment rather than deep mantle igneous origin beneath the mid-ocean ridge. On the other hand, the latter are possibly of deeper mantle origin than the former because of the absence of primary amphibole inclusion in spinel. Their similarity to chromitites of the Higashi-Akaishi ultramafic complex, which experienced high-P metamorphism, suggests that some of the characteristics of the

UHP chromitites can be formed by compression of low-P chromitites, such as deep recycling.

5.2: Acknowledgements

I would like to express my sincere gratitude to Professor S. Arai (Kanazawa University) for his supervising me and providing me with considerable encouragements, discussions and suggestions throughout this study. This thesis has been greatly improved by his comments. He especially provided me with opportunities for overseas field works and attending international conferences.

I am grateful to my current supervisor Prof. S. Umino (Kanazawa University) for discussions and suggestions about boninite formation in the initiation of sub-arc mantle.

I thank Dr. T. Mizukami (Kanazawa University) for discussions and suggestions of inclusion in minerals. He greatly assisted me with Raman spectroscopy analysis since my master's thesis, and provided me with samples from the Higashi-Akaishi ultramafic complex.

I am grateful to Prof. T. Morishita (Kanazawa University) and Dr. S. Ishimaru (Kumamoto University) for discussion and assistance in microprobe analysis. Dr. S. Ishimaru also assisted me in field expeditions to Oman, Turkey and the Polar Urals.

I thank Dr. A. Tamura (Kanazawa University) for discussions and suggestions. He greatly assisted me in LA-ICP-MS analysis.

I appreciate Dr. S. Yamamoto (University of Tokyo) and Dr. V. Shmelev (Ural Branch, Russian Academy of Sciences) for discussion and suggestion about ophiolites and UHP chromitites from Tibet and the Polar Urals. Dr. S. Yamamoto provided me with a lot of UHP chromitite and surrounding peridotite samples from Tibet, and teaching me about exsolution lamella in spinel. Dr. V. Shmelev gave me samples of UHP chromitites from the Polar Urals, and assisted me in field expedition to the Polar Urals.

I am grateful to Dr. A.H. Ahmed (King Abdulaziz University) for suggestion and discussion. He kindly taught me how to find and analyze PGMs in chromitite.

I thank Dr. M. Python (Hokkaido University), Dr. Y. Soda (Kanazawa University),

Dr. Y. Kusano (Kanazawa University), Dr. K. Kanayama (Kanazawa University), Ms. F. Zaeimnia (University of Tehran) and Dr. K. Abbou-Kebir (Kanazawa University; now Kyoto University) for discussions and suggestions. Dr. M. Python and Dr. K. Abbou-Kebir kindly shared information and samples of chromitites from the Oman ophiolite with me.

Dr. N. Akizawa (Kanazawa University), Mr. H. Negishi (Kanazawa University), Ms. M. Takeuchi (Kanazawa University), Mr. D. Deguchi (Kanazawa University), Mr. S. Takano (Kanazawa University), Mr. C. Hoshikawa (Kanazawa University), Ms. R. Muroi (Kanazawa University), Prof. O. Parlak (Cukurova University), Mr. D. Kuznecov (Ural Branch, Russian Academy of Sciences) and Dr. M.Z. Khedr (Kanazawa University) encouraged and assisted me in my field expeditions to Oman, Turkey and the Polar Urals. Mr. H. Negishi especially assisted me in field expeditions to Oman. Mr. D. Deguchi also especially assisted me in field expedition to Oman, and made many thin sections used in this study. Mr. S. Ishigami (Kanazawa University) provided me with chromitite samples, which were used in this study, from the Higashi-Akaishi ultramafic complex.

I am grateful to Mr. Salim Al Busaidi, Dr. M. Alaraimi and other people of the Ministry of Commerce and Industry, Sultanate of Oman for their hospitality and assistance.

This study was supported in part by JSPS KAKENHI Grant Number 25·8426.

5.3: References

Abbou-Kebir, K., Arai, S., Ahmed, A.H., & Ceuleneer, G. (2011) Origin of spinel-free dunite veins from northern Oman ophiolite: Possible involvement of a komatiitic melt. *Journal of Mineralogical and Petrological Sciences* **106**, 235-245.

Ahmed, A.H., Arai, S., & Attia, A.K. (2001): Petrological characteristics of podiform chromitites and associated peridotites of the Pan African Proterozoic ophiolite complexes of Egypt. *Mineralium Deposita* **36**, 72-84.

Ahmed, A.H. & Arai, S. (2002): Unexpectedly high-PGE chromitite from the deeper mantle section of the northern Oman ophiolite and its tectonic implications. *Contributions to Mineralogy and Petrology* **143**, 263-278.

Ahmed, A.H., Arai, S., & Kadoshima, K. (2002) Possible platinum-group element (PGE) oxides in the PGE mineralized chromitite from the Northern Oman Ophiolite. *Journal of Mineralogical and Petrological Sciences* **97**, 190-198.

Ahmed, A.H., & Arai, S. (2003): Platinum-group minerals in podiform chromitites of the Oman ophiolite. *The Canadian Mineralogist* **41**, 597-616.

Aitchison, J.C., Badengzhu, Davis A.M., Liu, J., Luo, H., Malpas, J.G., McDermid, R.C., Wu, H., Ziabrev, S.V., & Zhou, M. (2000) Remnants of Cretaceous intra-oceanic subduction system within the Yarlung– Zangbo suture (southern Tibet). *Earth and Planetary Science Letters* **183**, 231–244.

Andrews DRA, Brenan JM (2002) Phase-equilibrium constraints on the magmatic origin of laurite + Ru-Os-Ir alloy. *The Canadian Mineralogist* **40**, 1705-1716

Arai, S. (1974) "Non-calciferous" orthopyroxene and its bearing on the petrogenesis of ultramafic rocks in Sangun and Joetsu zones. Jour. *Japan. Assoc. Min. Pet. Econ. Geof.* **69**, 10, 343-353.

Arai, S. (1980): Dunite-harzburgite-chromitite complexes as refractory residue in the Sangun-Yamaguchi zone, western Japan. *Journal of Petrology* **21**, 141-165.

Arai, S. (1994): Characterization of spinel peridotites by olivine-spinel compositional relationships: Review and interpretation. *Chemical Geology* **113**, 191-204.

Arai, S. (1997): Control of wall-rock composition on the formation of podiform chromitites as a result of magma/peridotite interaction. *Resource Geology* **47**, 177-187.

Arai, S. (2010) Possible recycled origin for ultrahigh-pressure chromitites in ophiolites. *Journal of Petrological and Mineralogical Sciences* **105**, 280-285.

Arai, S. (2013) Conversion of low-pressure chromitites to ultrahigh-pressure chromitites by deep recycling: a good inference. *Earth Planetary Science Letters* **379**, 81-87.

Arai, S., & Abe, N. (1994): Podiform chromitite in the arc mantle: chromitite xenoliths from the Takashima alkali basalt, Southwest Japan arc. *Mineralium Deposita* **29**, 434-438.

Arai, S., Abe, N., Hirai, H., & Shimizu, Y. (2001): Geological, petrographical and petrological characteristics of ultramafic-mafic xenoliths in Kurose and

Takashima, northern Kyushu, southwestern Japan. *The science reports of the Kanazawa University* **46(1-2)**, 9-38.

Arai, S., Abe, N., & Ishimaru, S. (2007): Mantle peridotites from the Western Pacific. *Gondwana Research* **11**, 180-199.

Arai, S., Hirai, H., & Uto, K. (2000): Mantle peridotite zenoliths from the Southwest Japan arc: a model for the sub-arc upper mantle structure and composition of the Western Pacific rim. *Journal of Mineralogical and Petrological Sciences* **95**, 9-23.

Arai, S., & Ishimaru, S. (2008): Insights into petrological characteristics of the lithosphere of mantle wedge beneath arcs through peridotite xenoliths: a review. *Journal of Petrology* **49 (4)**, 665-695.

Arai, S., Kadoshima, K., & Morishita, T. (2006) Widespread arc-related melting in the mantle section of the northern Oman ophiolite as inferred from detrital chromian spinels. *Journal of the Geological Society, London* **163**, 869-879.

Arai, S., & Matsukage, K. (1998): Petrology of a chromitite micropod from Hess Deep, quatorial Pacific: a comparison between abyssal and alpine-type podiform chromitites. *Lithos* **43**, 1-14.

Arai, S., Okamura, H., Kadoshima, K., Tanaka, C., Suzuki, K., & Ishimaru, S. (2011): Chemical characteristics of chromian spinel in plutonic rocks: implications for deep magma processes and discrimination of tectonic setting. *Island Arc* **20**, 125-137.

Arai, S., Shimizu, Y., Morishita, T., & Ishida, Y. (2006): A new type of orthopyroxenite xenoliths from Takashima, Southwest Japan: Silica enrichment of the mantle by evolved alkali basalt. *Contributions to Mineralogy and Petrology* **152**, 387-398.

Arai, S., Uesugi, J., & Ahmed, A.H. (2004) Upper crustal podiform chromitite from the northern Oman ophiolite as the stratigraphically shallowest chromitite in ophiolite and its implication for Cr concentration. *Contributions to Mineralogy and Petrology* **147**, 145-154.

Arai, S., & Yurimoto, H. (1994): Podiform chromitites of the Tari-Misaka ultramafic complex, southwestern Japan, as mantle-melt interaction products. *Economic Geology* **89**, 1279-1288.

Arai, S., & Yurimoto, H. (1995): Possible sub-arc origin of podiform chromitites. *Island Arc* **4 (2)**, 104-111.

Aranovich, L., & Kawasaki, T. (2007) Si-in-spinel geobarometry for ultramafics. Geophysical Research Abstracts 9, 00823. SRef-ID: 1607-7962/gra/EGU2007-A-00823, Europian Geosciences Union.

Augé, T. (1987): Chromite deposits in thr northern Oman ophiolite: Mineralogical constraints. *Mineralium Deposita* **22**, 1-10.

Bai, W.J., Zhou, M.F., & Robinson, P. (1993) Possible diamond-bearing mantle peridotites and chromitites in the Luobusa and Dongiao ophiolites, Tibet. *Canadian Journal of Earth Sciences* **30**, 1650-1659.

Bai, W.J., Robinson, P.T., Fang, Q.S., Yang, J.S., Yan, B., Zhang, Z., Hu, X.-F., Zhou, M.-F., & Malpas, J., (2000) The PGE and base-metal alloys in the podiform chromitites of the Luobusa ophiolite, southern Tibet. *Canadian Mineralogist* **38**, 585-598.

Barth, M.G., Mason, P.R.D., Davies, G.R., Dijkstra, A.H., & Drury, M.R.(2003) Geochemistry of the Othris Ophiolite, Greece: Evidence for Refertilization? *Journal of Petrology* **44(10)**, 1759-1785.

Bizimis, M., Salters, V.J.M., & Bonatti, E. (2000) Trace and REE content of clinopyroxenes from supra-subduction zone peridotites. Implications for melting and enrichment processes in island arcs. *Chemical Geology* **165**, 67-85.

Borisova, A.Y., Ceuleneer, G., Kamenetsky, V.S., Arai, S., Béjina, F., Abily, B., Bindeman, I.N., Polve, M., Parseval, P.D., Aigouy, T., & Pokrovski, G.S. (2012): *Journal of Petrology* **53 (12)**, 2411-2440.

Brenan JM, Andrews DRA (2001) High-temperature stability of laurite and Ru-Os-Ir alloy and their role in PGE fractionation in mafic magmas. *The Canadian Mineralogist* **39**, 341-360

Brey, G.P., Doroshev, A.M., Girnis, A.V., & Turkin, A.I. (1999) Garnet-spinel-olivine-orthopyroxene equilibria in the FeO-MgO-Al_2O_3-SiO_2-Cr_2O_3 system: I. Composition and major volumes of minerals. *European Journal of Mineralogy* **11**, 599-617.

Cassard, D., Nicolas, A., Rabinovitch, M., Moutte, J., Leblanc, M., & Prinzhofer, A.

(1981) Structural classification of chromite pods in southern New Caledonia. *Economic Geology* **76**, 805-831.

Chen, M., Shu, J., Mao, H.K., Xie, X., & Hemley, R.J. (2003) Natural occurrence and synthesis of two new postspinel polymorphs of chromite. *Proceedings of the National Academy of Sciences* **100**, 14651-14654.

Dick, H.J.B., & Bullen, T. (1984): Chromian spinel as a petrogenetic indicator in abyssal and alpine-type peridotites and spatially associated lavas. *Contributions to Mineralogy and Petrology* **86**, 54-76.

Dick, H.J.B., & Natland, J.H. (1996) Late-stage melt evolution and transport in the shallow mantle beneath the east Pacific Rise. Proc. ODP, Science Results, 147, 103-134.

Ebel, D.S., & Naldrett, A.J. (1996): Fractional crystallization of sulfide ore liquids at high temperature. *Economic Geology* **91**, 607-621.

Ebel, D.S., & Naldrett, A.J. (1997): Crystallization of sulfide liquids and the interpretation of ore composition. *Canadian Journal of Earth Sciences* **34**, 352-365.

Economou, M.I. (1986): Platinum-group elements (PGE) in chromite and sulfide ores within the ultramafic zone of some Greek ophiolite complexes. *In*: Gallagher, M.J., Ixer, R.A., Neary, C.R., & Prichard, H.M. (eds) Metallogeny of basic and ultrabasic rocks. Inst Mining and Metallurgy Publ, London, 441-454.

Enami, M., & Mizukami, T. (2004) P-T-D Evolution of the Higashi-akaishi Ultramafic Mass in the Sanbagawa Metamorphic Belt, Central Shikoku, Japan: Subduction of Wedge Mantle Peridotite. *Journal of Geography* **113(5)**, 617-632 (in Japanese with English abstract).

Fisk, M.R. (1986) Basalt magma interaction with harzburgites and the formation of high-magnesium andesites. *Geophysical Research Letters* **13**, 5, 467-470.

Frey, F.A., & Printz, M. (1978) Ultramafic inclusions from San Carlos, Arizona: Petrologic and geochemical data bearing on their petrogenesis. *Earth Planetary Science Letters* **38**, 129-176.

Frost, D.J. (2006) The stability of Hydrous Mantle Phases. *Reviews in Mineralogy and Geochemistry* **62**, 243-271.

Garuti, G., & Zaccarini, F. (1997) In situ alteration of platinum-group minerals at low temperature: Evidence from serpentinized and weathered chromitite of the Vourinos complex, Greece. *The Canadian Mineralogist* **35**, 611-626.

Garuti G, Zaccarini F, Moloshag V, Alimov V (1999) Platinum-group minerals as indicators of sulfur fugacity in ophiolitic upper mantle: An example from chromitites of the Ray-Iz ultramafic complex, Polar Urals, Russia. *The Canadian Mineralogist* **37**, 1099-1115

González-Jiménez, J.M., Proenza, J.A., Gervilla, F., Melgarejo, J.C., Blanco-Moreno, J.A., Ruiz-Sánchez, R., & Griffin, W.L. (2011): High-Cr and high-Al chromitites from the Sagua de Tánamo district, Mayarí-Cristal ophiolitic massif (eastern Cuba): Constraints on their origin from mineralogy and geochemistry of chromian spinel and platinum-group elements. *Lithos* **12**, 101-121.

Green, D.H., & Ringwood, A.E. (1967): The stability fields of aluminous pyroxene peridotite and garnet peridotite and their relevance in upper mantle structute. *Earth and Planetary Science Letters* **3**, 151-160.

Harris, D.C., & Cabri, L.J. (1991) Nomenclature of platinum group-element alloys: review and revision. *The Canadian Mineralogist* **29**, 231-237.

Hattori, K., Wallis, S., Enami, M., & Mizukami, T. (2010) Subduction of mantle wedge peridotites: Evidence from the Higashi-akaishi ultramafic body in the Sanbagawa metamorphic belt. *Island Arc* **19**, 192-207.

Hellebrand, E., Snow, J.E., Dick, H.J.B., & Hofman, A.W. (2001) Coupled major and trace elements as indicators of the extent of melting in mid-ocean-ridge peridotites. *Nature* **410**, 677-681.

Hébert, R., Huot, F.,Wang, C.S., & Liu, Z. (2003) Yarlung zangbo ophiolites (Southern Tibet) revisited: geodynamic implications from the mineral record. In: Dilek, Y., Robinson, P.T. (Eds.), Ophiolites in Earth History. *Geological Society of London*, pp. 165–190.

Huot, F., Hebert, R., Varfalvy, V., Beaudoin, G.,Wang, C., Liu, Z., Cotten, J., & Dostal, J. (2002) The Beimarang melange (southern Tibet) brings additional constraints in assessing the origin, metamorphic evolution and obduction processes of the Yarlung Zangbo ophiolite. *Journal of Asian Earth Sciences* **21**,

307–322.

Huang, E., Chen, C.H., Huang, T., Lin, E.H., & Xu, Ji.-An. (2000) Raman spectroscopic characteristics of Mg–Fe–Ca pyroxenes. *American Mineralogist* **85**, 473–479.

Huang, M-X., Yang, J-J., Powell, R., & Mo, X.X. (2014) High-pressure metamorphism of serpentinized chromitite at Luobusa (southern Tibet). *American Journal of Science* **314**, 400-433. DoI: 10.2475/01.2014.11

Ionov, D.A., Bénard, A., Plechov, P.Y., & Shcherbakov, V.D. (2003) Along-arc variations in lithospheric mantle compositions in Kamchatka, Russia: First trace element data on mantle xenoliths from the Klyuchevskoy Group volcanos. *Journal of Volcanology and Geothermal Research* **263**, 122-131.

Ishikawa, T., Nagaishi, K., & Umino, S. (2002): Boninitic volcanism in the Oman ophiolite: Implications for thermal condition during transition from spreading ridge to arc. *Geology* **30**, 10, 899-902.

Ishikawa, T., Fujisawa, S., Nagaishi, K., & Masuda, T. (2005) Trace element characteristics of the fluid liberated from amphibolites-facies slab: Inference from the metamorphic sole beneath the Oman ophiolite and implication for boninite genesis. *Earth and Planetary Science Letters* **240**, 355-377.

Ishimaru, S., Arai, S., Ishida, Y., Shirasaka, M., & Okugin, V.M. (2007) Melting and Multi-stage Metasomatism in the Mantle Wedge beneath a Frontal Arc Inferred from Highly Depleted Peridotite Xenoliths from the Avacha Volcano, southern Kamchatka. *Journal of Petrology* **48**, 395-433.

Ishimaru, S., & Arai, S. (2008) Nickel enrichment in mantle olivine beneath a volcanic front. *Contributions to Mineralogy and Petrology* **156**, 119-131.

Ismail, S.A., Arai, S., Ahmed, A.H., & Shimizu, Y. (2009): Chromitite abd peridotite from Rayat, northeastern Iraq, as fragments of a Tethyan ophiolite. *Island Arc* **18**, 175-183.

Isozaki, Y., Maruyama, S., Nakama, T., Yamamoto, S., & Yanai, S. (2011): Growth and Shrinkage of an Active Continental Margin: Updated Geotectonic History of the Japanese Islands. *Journal of Geography* **120 (1)**, 65-99 (in Japanese with English abstract).

Ito M, Yurimoto H, Morioka M, Nagasawa H (1999) Co^{2+} and Ni^{2+} diffusion in olivine determined by secondary ion mass spectrometry. *Phys Chem Miner* **26**:425–431

Iwamori, H. (1991): Zonal structure of Cenozoic basalts related to mantle upwelling in southwest Japan. *Journal of Geophysical Research* **96**, 6157-6170.

Kanke, N., & Takazawa. (2014) A kilometer-scale highly refractory harzburgite zone in the mantle section of the northern Oman Ophiolite (Fizh Block): implications for flux melting of oceanic lithospheric mantle. In: Rollinson, H.R. et al. (eds) *Tectonic Evolution of the Oman Mountains. Geological Society, London, Special Publications* **392**, 229-246.

Kelemen, P.B. (1990) Reaction Between Ultramafic Rock and Fractionating Basaltic Magma I. Phase Relations, the Origin of Calc-alkaline Magma Series, and the Formation of Discordant Dunite. *Journal of Petrology* **31**, 51-98.

Kelemen, P.B., Shimizu, N., & Salters, V.J.M. (1995) Extraction of mid-ocean-ridge basalt from the upwelling mantle by focused flow of melt in dunite channels. *Nature* **375**, 747-753.

Klingenberg, B.M.E.T., & Kushiro, I. (1996) Melting of a chromite-bearing harzburgite and generation of boninitic melts at low pressures under controlled oxygen fugacity. *Lithos* **37**, 1-13.

Kobayashi, Y., & Arai, S. (1981): Ultramafic Nodules in Alkali Basalt from Taka-Shima, Saga Prefecture, Japan. *Geoscience Reports of Shizuoka University* **6**, 11-24.

Kusano, Y., Hayashi, M., Adachi, Y., Umino, S., & Miyashita, S. (2014) Evolution of volcanism and magmatism during initial arc stage: constraints on the tectonic setting of the Oman ophiolite. In: Rollinson, H.R. et al. (eds) *Tectonic Evolution of the Oman Mountains. Geological Society, London, Special Publications* **392**, 177-193.

Kushiro, I., & Yoder, H.S. (1966) Anorthite-Forsterite and Anorthite-Enstatite Reactions and their bearing on the Basalt-Eclogite Transformation. *Journal of Petrology* **7(3)**, 337-362.

Le Mée, L., Girardeau, J., & Monnier, C. (2004) Mantle segmentation along the

Oman ophiolite fossil mid-ocean ridge. *Nature* **432**, 167-172.

Leblanc, M. (1991): Platinum-group elements and gold in ophiolitic complexes: distribution and fractionation from mantle to oceanic floor. *In*: Peters, T. *et al*. (eds) Ophiolite genesis and evolution of the oceanic lithosphere, Oman. Kluwer, Dordrecht, 231-260.

Liou, J.G., Tsujimori, T., Yang, J., Zhang, R.Y., & Ernst, W.G. (2014) Recycling of crustal materials through study of ultrahigh-pressure minerals in collisional orogens, ophiolites, and mantle xenoliths: A review. *Journal of Asian Earth Sciences* **96**, 386-420.

Lippard, S.J., Shelton, A.W., & Gass, I.G. (1986): The Ophiolite of Northern Oman. Geological Society Memoir, No. 11, Blackwell, Oxford. pp.178.

Mashima, H. (2009): Genesis of high-magnesium andesites and associated basalts from Saga-Futagoyama, northwest Kyusyu, southwest Japan. *Journal of Volcanology and Geothermal Research* **187**, 106-116.

Matsumoto, I., Arai, S., & Yamauchi, H. (1997): High-Al podiform chromitites in dunite-harzburgite complexes of the Sangun zone, central Chugoku district, Southwest Japan. *Journal of Asian Earth Sciences* **15**, 295-302.

Matsumoto, I., & Tomurtogoo, O. (2003): Petrological characteristics of the Hantaishir ophiolite complex, Altai Region, Monglia: Coexistence of podiform chromitite and boninite. *Gondwana Research* **6(2)**, 161-169.

Miura, M., Arai, S., Ahmed, A.H., Mizukami, T., Okuno, M., & Yamamoto, S. (2012): Podiform chromitite classification revisited: A comparison of discordant and concordant chromitite pods from Wadi Hilti, northern Oman ophiolite. *Journal of Asian Earth Sciences* **59**, 52-61.

Miura, M., Arai, S., & Tamura, A. (2014): Formation of discordant chromitite at the initiation of sub-arc mantle processes: Observations from the northern Oman ophiolite. *Journal of Mineralogical and Petrological Sciences* **109**, 38-43.

Mirwald, P.W., & Massonne, H.-J. (1980) The Low-High Quartz and Quartz-Coesite Transition to 40 kbar Between 600° and 1600°C and Some Reconnaissance Data on the Effect of NaAlO2 Component on the Low Quartz-Coesite Transition. *Journal of geophysical research* **85 (No. B12)**, 6983-6990.

Mizukami, T., & Wallis, S. (2005) Structural and petrological constraints on the tectonic evolution of the garnet-lherzolite facies Higashi-akaishi peridotite body, Sambagawa belt, SW Japan. *Tecotonics* **24**, TC6012 1-17.

Morishita, T., Andal, E.S., Arai, S., & Ishida, Y. (2006): Podiform chromitites in the lherzolite-dominant mantle section of the Isabela ophiolite, the Philippines. *Island Arc* **15**, 84-101.

Morishita, T., & Arai, S. (2003) Evolution of spinel-pyroxene symplectite in spinel-lherzolites from the Horoman Complex, Japan. *Contributions to Mineralogy and Petrology* **144**, 509-522.

Naemura, K., Ikuta, D., Kagi, H., Odake, S., Ueda, T., Ohi, S., Kobayashi, T., Svojtka, M. & Hirajima, T. (2011) Diamond and other possible ultra-deep evidence discovered in the orogentic spinel-garnet peridotite from the Moldanubian Zone of the Bohemian Massif, Czech Republic. *In: Dobrzhinetskayam, L., Faryad, S.W., Wallis, S & Cuthbert, S. (Eds.), Ultrahigh-Pressure Metamorphism, 25 years after the Discovery of Coesite and Diamond. Elsevier, Amsterdam*, pp. 77-105.

Nakamura, E., McDougall, I., & Campbell, I.H. (1986): K-Ar ages of basalts from the Higashi-Matsuura distinct, northern Kyushu, Japan and regional geochronology of the Cenozoic alkaline volcanic rocks in eastern Asia. *Geochemical Journal* **20**, 91-99.

Naldrett, A.J., & Duke, J.M. (1980): Platinum metals in magmatic sulfide ores. *Science* **208**, 1417-1424.

Negishi, H., Arai, S., Yurimoto, H., Ito, S., Ishimaru, S., Tamura, A., & Akizawa, N. (2013): Sulfide-rich dunite within a thick Moho transition zone of the northern Oman ophiolite: Implications for the origin of Cyprus-type sulfide deposits. *Lithos* **164-167**, 22-35.

Nicolas, A. (1989): Structures of ophiolites and dynamics of oceanic lithosphere. Dordrecht, Netherlands, Kluwer Academic Publishers, 367 pp

Niida, K., & Green, D.H. (1999) Stability and chemical composition of pargasitic amphibole in MORB pyrolite under upper mantle conditions. *Contributions to Mineralogy and Petrology* **135**, 18-40.

Nixon, P.H. (Ed.) (1987): Mantle Xenoliths. John Wiley & Sons, New York, 384 pp

Otofuji, Y., Itaya, T., & Matsuda, T. (1991): Rapid rotation of southwest Japan: Paleomagnetism and K-Ar ages of Miocene volcanic rocks of Southwest Japan. *Geophysical Journal International* **105**, 397-405.

Ozawa, K. (1984) Olivine-spinel geospeedometry: Analysis of diffusion-controlled Mg-Fe^{2+} exchange. *Geochimica et Cosmochimica Acta* **48**, 2597-2611.

Page, N.J., Pallister, J.S., Brown, M.A., Smewing, J.D., & Haffty, J. (1982): Palladium, platinum, rhodium, iridium and ruthenium in chromite-rich rocks from the Samail ophiolite, Oman. *Canadian Mineralogist* **20**, 537-548.

Petry C, Chakraborty S, Palme H (2004) Experimental determination of Ni diffusion coefficients in olivine and their dependence on temperature, composition, oxygen fugacity, and crystallographic orientation. *Geochim Cosmochim Acta* **68(20)**, 4179–4188.

Python, M., & Ceuleneer, G. (2003) Nature and distribution of dykes and related melt migration structures in the mantle section of the Oman ophiolite. *Geochemistry Geophysics Geosystems* **4**, 8612, doi:10.1029/2002GC000354.

Robinson, P.T., Bai, W.-J., Malpas, J., Yang, J.-S., Zhou, M.F., Fang, Q.-S., Hu, X.-F., Cameron, S., Staudigel, H. (2004) Ultra-high pressure minerals in the Luobusa Ophiolite, Tibet, and their tectonic implications. In: Malpas, J., Fletcher, C.J.N., Ali, J.R., Aitchison, J.C. (Eds.), Aspects of the Tectonic Evolution of China. *J. Geol. Soc. Special Publication* **226**, 247–271.

Rollinson, H. (2005) Chromite in the mantle section of the Oman ophiolite: a new genetic model. *Island Arc* **14**, 542-550.

Rollinson, H. (2008) The geochemistry of mantle chromitites from the northern part of the Oman ophiolite: inferred parental melt compositions. *Contributions to Mineralogy and Petrology* **156**, 273-288.

Ruskov, T., Spirov, I., Georgieve, M., Yamamoto, S., Green, H.W., McCammon, C.A., & Dobrzhinetskaya, L.F. (2010) Mössbauer spectroscopy studies of the valence state of iron in chromite from the Luobusa massif of Tibet: implications for a highly reduced deep mantle. *Journal of metamorphic Geology* **28**, 551-560.

Sato, H. (1977) Nickel content of basaltic magmas: identification of primary magmas and a measure of the degree of olivine fractionation. *Lithos* **10(2)**, 113-120.

Savelieva, G.N., & Nesbitt, R.W. (1996) A synthesis of the stratigraphic and tectonic setting of the Uralian ophiolites. *Journal of the Geological Society, London* **153**, 525-537.

Senda, R., Tanaka, T., & Suzuki, K. (2007) Os, Nd, and Sr isotopic and chemical compositions of ultramafic xenoliths from Kurose, SW Japan: Implications for contribution of slab-derived material to wedge mantle. *Lithos* **95**, 229-242.

Shi, R., Alard, O., Zhi, X., O'Reilly, S.Y., Pearson, N.J., Greffin, W.L., Zhang, M., & Chen, X. (2007) Multiple events in the Neo-Tethyan oceanic upper mantle: Evidence from Ru-Os-Ir alloys in the Luobusa and Dongqiao ophiolitic podiform chromitties, Tibet. *Earth and Planetary Science Letters* **261**, 33-48.

Shmelev, V.R. (2011) Mantle ultrabasites of ophiolite complexes in the Polar Urals: petrogenesis and geodynamic environments. *Petrology* **19**, 618–640.

Shmelev, V.R., & Meng, F.C. (2013) Thenature and age of basic rocks of the Rai-Iz ophiolite massif (Polar Urals). *Doklady Earth Sciences* **451**, 758–761.

Sugaki, A., & Kitakaze, A. (1998): High form of pentlandite and its thermal stability. *American Mineralogist* **83**, 133-140.

Takahashi, E. (1978): Petrologic model of the crust and upper mantle of the Japanese island arcs. *Bull Volcanology* **41**, 529-547.

Takahashi, E., Uto, K., Schilling, J.-G., 1987. Primary magma compositions and Mg/Fe ratios of their mantle residues along Mid Atlantic Ridge 29_N to 73_N. *Technical Report of Institute for Study of the Earth's Interior Okayama University Series* **A 9**, 1–14.

Takazawa, E., Okayasu, T., & Satoh, K. (2003): Geochemistry and origin of the basal lherzolites from the northern Oman ophiolite (northern Fizh block). *Geochemistry Geophysics Geosystems* **4**, 1021. Doi:10.1029/2001GC000232

Tamura, A., & Arai, S. (2006) Harzburgite-dunite-orthopyroxenite suite as a record of supra-subduction zone setting for the Oman ophiolite mantle. *Lithos* **90**, 43-56.

Tamura, A., Arai, S., Ishimaru, S., & Andal, E.S. (2008) Petrology and geochemistry of peridotites from IODP Site U1309 at Atlantis Massif, MAR 30°N: micro- and macro-scale melt penetrations into peridotites. *Contributions to Mineralogy and Petrology* **155**, 491-509.

Tatsumi, Y., Ishikawa, N., Anno, K., Ishizaka, K., & Itaya, T. (2001): Tectonic setting of high-Mg andesite magmatism in the SW Japan arc: K-Ar chronology of the Setouchi volcanic belt. *Geophysical Journal International* **144**, 625-631.

Tatsumi, Y., & Maruyama, S. (1989): Boninites and high-Mg andesites: tectonics and petrogenesis. In: Crawford, A.J. (Ed.), Boninites. Unwin Hyman, London, pp.50-71.

Thayer, T.P. (1964): Principal features and origin of podiform chromitite deposits, and some observations on the Guleman-Soridağ district, Turkey. *Economic Geology* **59**, 1497-1524.

Thayer, T.P. (1970): Chromite segregations as petrogenetic indicators. Geological Society of South Africa Special Publication 1, 380-390

Uysal, I., Sadiklar, M.B., Tarkian, M., Karsli, O., & Aydin, F. (2005): Mineralogy and composition of the chromitites and their platinum-group minerals from Ortaca (Muğla-SW Turkey): evidence for ophiolitic chromitite genesis. *Mineralogy and Petrology* **83**, 219-242.

Ulmer, P., Stalder, R., 2001. The Mg(Fe)SiO3 orthoenstatite–clinoenstatite transitions at high pressures and temperatures determined by Raman-spectroscopy on quenched samples. *American Mineralogist* **86**, 1267–1274.

Wood, B.J., & Banno, S. (1973): Garnet-orthopyroxene and orthopyroxene clinopyroxene relationships in simple and complex systems. *Contributions to Mineralogy and Petrology* **42**, 109-124.

Xu, X., Yang, J., Songyong, C., Qingsong, F., & Wenji, B. (2009) Unusual Mantle Mineral Group from Chromitite Orebody Cr-11 in Luobusa Ophiolite of Yarlung-Zangbo Suture Zone, Tibet. *Journal of Earth Science* **20 (2)**, 284-302.

Xu, X., Yang, J., Ba, D., Guo, G., Robinson, P.T., & Li, J. (2011) Petrogenesis of the Kangjinla peridotite in the Luobusa ophiolite, Southern Tibet. *Journal of Asian Earth Sciences* **42**, 553-568.

Yamamoto, H., Yamamoto, S., Kaneko, Y., Terabayashi, M., Komiya, T., Katayama, I., & Iizuka, T. (2007) Imbricate structure of the Luobusa Ophiolite and surrounding rock units, southern Tibet. *Journal of Asian Earth Sciences* **29**, 296-304.

Yamamoto, S., Komiya, T., Hirose, K., & Maruyama, S. (2009) Coesite and clinopyroxene exsolution lamellae in chromitites: In-situ ultrahigh-pressure evidence from podiform chromitites in the Luobusa ophiolite, southern Tibet. *Lithos* **109**, 314-322.

Yamamoto, S., Komiya, T., Yamamoto, H., Kanako, Y., Terabayashi, M., Katayama, I., Iizuka, T., Maruyama, S., Yang, J., Kon, Y., & Hirata, Takafumi. (2013) Recycled crustal zircons from podiform chromitites in the Luobusa ophiolite, southern Tibet. *Island Arc* **22**, 89-103.

Yang, J., Dobzhinetskaya, L., Bai, W.-J., Fang, Q.-S., Robinson, P.T., Zhang, J., & GreenII, H.W. (2007) Diamond- and coesite-bearing chromitites from the Luobusa ophiolite, Tibet. *Geology* **35**, 875-878.

Yang, J., Meng, F., Xu, X., Robinson, P.T., Dilek, Y., Makeyev, A.B., Wirth,R., Wiedenbeck, M., Griffin, W.L., & Cliff, J. (2014) Diamonds, native elements and metal alloys from chromitites of the Ray-Iz ophiolite of the Polar Urals. Gondwana Research, doi:10.1016/j.gr.2014.07.004 (*in press*)

Zaccarini, F., Pushkarev, E., & Garuti, G. (2008): Platinum-group element mineralogy and geochemistry of chromitite of the Kluchevskoy ophiolite complex, central Urals (Russia). *Ore Geology Reviews* **33**, 20-30

Zhou, M.-F., Robinson, P., Bai, W.-J., 1994. Formation of podiform chromitites by melt/rock interaction in the upper mantle. Mineralium Deposita 29, 98–101.

Zhou, M-F., Robinson, P.T., Malpas, J., & Li, Z. (1996): Podiform chromitites in the Luobusa ophiolite (Southern Tibet): Implications for melt-rock interaction and chromite segregation in the upper mantle. *Journal of Petrology* **37(1)**, 3-21.

Zhou, M-F., Robinson, P.T., Malpas, J., Edwards, S.J., & Qi, L. (2005) REE and PGE Geochemical Constraints on the Formation of Dunites in the Luobusa Ophiolite, Southern Tibet. *Journal of Petrology* **46**, 615-639.

Zhou, M-F., Sun, M., Keays, R.R., & Kerrich, R.W. (1998): Controls on platinum-group elemental distributions of podiform chromitites: A case study of high-Cr and high-Al chromitites from Chinese orogenic belts. *Geochimica et Cosmochimica Acta* **62 (4)**, 677-688.